University of Calgary

PRISM Repository **https://prism.ucalgary.ca**

The Vault Open Theses and Dissertations

2018-05-17

Polarization Controlled Coherent Anti-Stokes Raman Scattering Microscopy for Determination of Structural Order of the Myelin Sheath

Brideau, Craig

Brideau, C. (2018). Polarization Controlled Coherent Anti-Stokes Raman Scattering Microscopy for Determination of Structural Order of the Myelin Sheath (Doctoral thesis, University of Calgary, Calgary, Canada). Retrieved from https://prism.ucalgary.ca. doi:10.11575/PRISM/31926 http://hdl.handle.net/1880/106645

Downloaded from PRISM Repository, University of Calgary

UNIVERSITY OF CALGARY

Polarization Controlled Coherent Anti-Stokes Raman Scattering Microscopy for Determination of Structural Order of the Myelin Sheath

by

Craig Brideau

A THESIS

SUBMITTED TO THE FACULTY OF GRADUATE STUDIES

IN PARTIAL FULFILMENT OF THE REQUIREMENTS FOR THE

DEGREE OF DOCTOR OF PHILOSOPHY

GRADUATE PROGRAM IN BIOMEDICAL ENGINEERING

CALGARY, ALBERTA

MAY, 2018

© Craig Brideau 2018

Abstract

Coherent Anti-Stokes Raman Scattering (CARS) is a laser-scanning microscopy technique that generates a strong label-free signal in lipid. The myelin sheath surrounding nerves is up to 80% lipid, and therefore is an ideal candidate for CARS imaging. The long lipid chains forming the myelin wraps have a directional preference when the myelin is healthy, with CH_2 bonds aligned parallel to the axis of the nerve. The optical polarization dependence of the CARS signal can be used to probe the orientation of CH_2 bonds in the sheath and determine their nanoscopic orientation. As myelin becomes unhealthy the organization of the lipids begins to loosen from their native organized packing structure. In the early stages this is not visible by conventional microscopy, however polarization-resolved CARS can measure the increasing disorder in the arrangement of the bonds before obvious morphological changes can occur. The degree of disorder is also measured to provide a metric of myelin disorganization in disease models.

Keywords: Coherent anti-Stokes Raman scattering, anisotropy, laser microscopy, nonlinear optics

Preface

The purpose of this work is to introduce a method of polarized-resolved coherent anti-Stokes Raman scattering for measuring the nanostructural order of the myelin sheath. The design and construction of a unique laser-scanning microscopy system using optical parametric amplifier light sources will be presented. The system and data processing methods will be applied to proof-of-principle biological samples to confirm its effectiveness. Comparisons against other myelin imaging methods will be discussed to frame the relevance of the proposed technique to models of demyelinating disease.

Acknowledgements

The author would like to acknowledge the assistance of Dr. Andrew Caprariello and Megan Morgan in providing assistance with the cuprizone samples used in this work. Special thanks to Dr. Sangeeta Murugkar for moral support while working to find ‘time zero’.

Dedication

This work is dedicated to my son, Malcolm, who slept through most nights, my wife, Monique, who supported me over this long road, and my parents who always put my education first.

Table of Contents

List of Tables

List of Figures and Illustrations

Epigraph

"*Music is the arithmetic of sounds as optics is the geometry of light***"**

-Claude Debussy

1. INTRODUCTION

The myelin sheath is a protective, multi-layered structure surrounding axons. It is a complex structure comprised of highly ordered lipid bilayers and proteins which aids in the efficient transmission of nerve impulses.[1] Deterioration of healthy myelin leads to dysfunction of the nervous system, and is a factor in neurological disease. [2] It is therefore a major target for study in numerous disease models to gain insight into how myelin failure occurs.

Multiple Sclerosis is a demyelinating disease of the central nervous system. [3] The mechanisms of this myelin loss are unknown and the symptoms are highly variable among patients.[4,5] Areas of localized myelin loss, called lesions, appear in the brain or spinal cord.[6] In some patients these lesions are transient, with relapsing and remitting symptoms and appearance of the lesions.[7] In others, the lesion is progressive, spreading to multiple regions in the nervous system. [8]

The variability of symptoms and the many different paths of disease progression make MS a perplexing problem to study. However, at the core of the disease demyelination is always a factor and studying demyelination will hopefully shed light on the underlying mechanisms.[9] In the laboratory, myelin samples are often imaged to observe structure and function, and the spatial and temporal relationship to other cells and the environment. [10]

Currently, the majority of myelin imaging is performed with direct lipophilic staining[11,12], such as luxol fast blue[13], or immunohistochemistry[14] or immunofluorescent[15,16] microscopy techniques, including wide field or laser-scanning methods such as confocal or multiphoton microscopy. [17,18] These techniques rely on chromophores or on specific antibody binding to (typically) protein epitopes. Other than reporting the presence, absence or relative abundance of

myelin and its distribution, limited information about myelin or myelin dysfunction is provided by these well-established methods.

This work presents a novel method of interrogating myelin nanostructure based on polarization-resolved coherent anti-Stokes Raman scattering (CARS). CARS has been used previously to allow label-free imaging of the morphology of myelin and provide chemical information in situ of its composition. In this work we extend the capability of CARS with polarization-resolved imaging to determine the nanostructural organization of myelin in two injury models in fixed and living samples of CNS and PNS myelin. Details of these animal models and their relationship to MS will be presented in Chapter 3.

1.1. What is Myelin?

The nervous system is delineated into two general categories; the central nervous system (CNS), consisting of the brain and spinal cord, and the peripheral nervous system (PNS) containing nerves and cells outside the CNS and communicate with the CNS primarily through the spinal cord. [19]

1.1.1. Purpose and Structure

Nerve cells communicate over long distances via projections called axons. The axon extends from the cell body and interacts with other cells at a remote location through synaptic junctions. Axons transmit signals down their length in the form of an electrochemical action potential. [20] When the action potential reaches a synaptic junction, chemicals known as neurotransmitters are released. The neurotransmitters interact with various receptors on the target cell to elicit a stimulus, either excitatory, inhibitory or biochemical. This can, for instance, include transmission

of sensation from sensory nerves, or induce the contraction of a muscle. In general, axons that carry information to the CNS are known as afferent fibers, while those that carry information from the CNS outward, such as to a muscle, are efferent fibers. [21] The electrical signal of the action potential is a transmembrane voltage potential propagating down the length of the nerve. In the resting state, a voltage of -80 mV exists between the extracellular space and the axon across the membrane. An active sodium-potassium pump maintains the voltage gradient by expelling three sodium ions for every two potassium ions drawn in.[22] This creates a gradient in ionic concentration, with more sodium outside the axon as a result of the sodium-potassium pump, and also a voltage gradient as the pump expels three positively charged sodium ions for every two potassium ions it draws in. Leaky ion channels also allow potassium to passively exit the axon while restricting entry of sodium, leading to a net reduction of positively charged ions inside the membrane. [23]

The action potential begins by the depolarization of the membrane voltage from the resting state. Sodium channels open, triggering an inrush of positively-charged sodium ions at the beginning of the axon near the cell body, called the axon hillock.[24] The inward current into the axon increases the membrane voltage from the resting state. In the case of myelinated axons, this inward current flows down the length of the axon, rather than leaking out the axolemma because of the insulating myelin.[25] When this current exiting at the next node of Ranvier causes a depolarization that exceeds a triggering threshold (typically -50 mV for sodium channels) more sodium channels are triggered, repeating the cycle of membrane depolarization. The influx of sodium repeats down the axon as the action potential propagates, resulting in rapid saltatory conduction. [26]

The repeated activation of sodium channels and the time required for sodium to enter the nerve is slow compared to the action of the electric field created by the concentration of positive charge at the sodium channel sites. This limits the speed of propagation in unmyelinated axons as the action potential must be constantly regenerated by sodium influx and activation of adjacent sodium channels continuously along the length. The electric field decreases rapidly with distance, so frequent sodium channels are required to maintain the propagation of the action potential.[27]

In myelinated axons, the myelin sheath accelerates the propagation of the action potential by reducing membrane capacitance and increasing membrane resistance along sections of the axon. This shields the electric field across the membrane from charge leakage to the extracellular space, increasing the distance over which the field will reach. This allows the sodium channels to be spaced further apart, reducing the amount of sodium ion exchange necessary for the action potential to propagate. [28]

Periodic breaks in the myelin, known as nodes of Ranvier,[29] expose small segments of the axon to the extracellular space. Sodium channels necessary for regenerating the action potential are concentrated at the nodes where they can access extracellular sodium. When the channels activate at one node, the electric field depolarizes the membrane at the next node. The action potential then rapidly propagates through the next myelinated section to further nodes, repeating down the length of the axon. This causes the action potential to jump rapidly from node to node, a process known as saltatory conduction. [29]

For the above reasons, the myelin sheath plays a critical role in supporting conduction within the nervous system. Myelin is comprised of multiple layers of lipid and protein in a rolled-up sheet which surrounds the axon cylinder. In the CNS, the myelin is created by a cell type known as an

oligodendrocyte. A single oligodendrocyte cell can extend numerous processes and contact many adjacent axons. At each contact point, the oligodendrocyte enwraps the axon with multiple layers of membrane. The length of an axon segment ensheathed by myelin, is known as the internode, with nodes of Ranvier forming the channel-rich, myelin-free axonal segments between flanking the internodes.[30-32]

Small channels also pass through the myelin sheath itself, called incisures. These incisures allow the transport of molecules in the internodal region between the axon and extracellular space. Incisures open and close under various conditions such as metabolic stress although the reason for this is not yet understood. [33] In the PNS, a cell type known as a Schwann cell wraps myelin around axons, conferring similar biophysical advantages to peripheral myelinated fibers. While a single oligodendrocyte in the CNS can myelinate multiple axons, in the PNS a single Schwann cell creates only a single section of myelin around a single axon. Each internode segment in a myelinated PNS axon therefore represents the wrapping supplied by a single Schwann cell. Figure 1 illustrates an example of CNS and PNS myelinated axons.

In both CNS and PNS, the myelin wraps compact tightly, forming a dense periodic structure around the axon. The periodicity of these repeating layers is approximately 12 nm with alternating layers of intra and extra-cellular space. [30,34] At the node of Ranvier the myelin layers are slightly looser and form finger-like projections curling inward at the end of the myelin cylinder to seal up the ring around the exposed section of axon at the node. This area of less-compacted myelin is known as the paranode.[35]

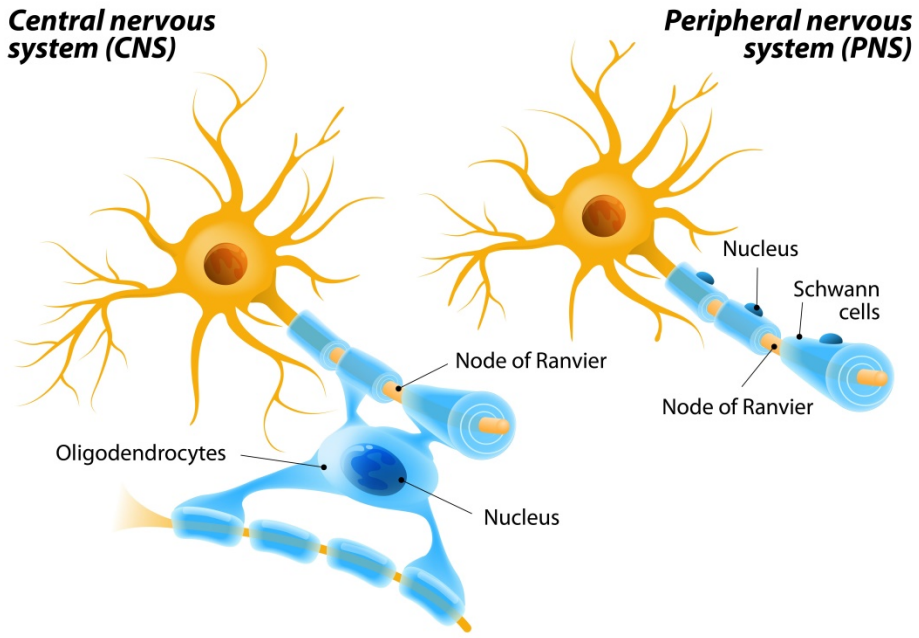

Figure 1 Central nervous system (CNS) and Perpheral nervous system (PNS) nerve cell with Myelin. Myelin is provided in the CNS by Oligodendrocytes where one cell myelinates many nerves. In the PNS each segment of myelin is a single Schwann cell.
Royalty-free licence, Shutterstock 238798720

1.1.2. Biochemical composition of Myelin

As an extension of the myelinating cell's membrane, the myelin wraps are comprised of regular lipid bilayer structures with various embedded and transmembrane proteins. Myelin contains a higher ratio of lipid to protein, comprising approximately 75% lipid to 25% protein by weight, compared to other plasma membranes. [30,36-38]

The lipid content in myelin is primarily phospholipid, which is comprised of one or multiple fatty acid chains forming a hydrophobic region. A phosphate head group at the top of the chain forms a hydrophilic region creating an amphipathic molecule. The major components present in myelin include the sterol cholesterol, galactolipid, and the phospholipids ethanolamine phosphatide, choline phosphatide, inositol phosphatide, serine phosphatide and sphingomyelin. [39]

All of these lipids possess long unsaturated fatty acid chains except for cholesterol, which contains four hydrocarbon rings and a shorter acyl chain.[40]

Like other cell membranes, myelin forms into lipid bilayers wherein the hydrophobic tails of the lipids point inwards forming two layers of lipid molecules pointing tail-first towards each other. The hydrophilic head groups form the top and bottom outer surfaces of the structure. It is important to note the exteriors of the bilayer membranes alternate between extracellular and cytoplasmic space due to the multilayer wrapping of myelin. The cytoplasm-enclosing membranes are densely packed and known as the major dense line with only a thin (≈4-5 nm) cytoplasmic spiral between the compressed membrane pairs. The extracellular space is known as the interperiod line and is comprised of closely apposed outer membranes. [30,41]

Although myelin is predominantly lipid, proteins still play a major role in determining structure.[42] Myelin basic protein (MBP) is a positively-charged molecule found within the cytoplasmic space. The positive charge shields the opposing negatively-charged hydrophilic head groups on the membranes in the cytosolic space. The two inner membrane surfaces can then pack closer together without negative electrostatic forces spreading the layers apart. Myelin protein zero (P0) also plays a similar role in the PNS, with a positively charged tail on the cytoplasmic side of the membrane. [37] In the extracellular space of CNS, proteolipid protein (PLP) is believed to regulate packing between the opposing external membranes, although the exact mechanism is not understood. A summary of major myelin proteins and lipids can be found in Table 1.

Component	% dry weight
Total protein	30.0
Some individual proteins:	
Central myelin:	
Myelin basic protein (MBP)	
Claudin-11 (oligodendrocyte-specific protein, OSP)	
Proteolipid protein (PLP)	
Peripheral myelin:	
Myelin basic protein (MBP)	
P2 protein (basic)	
P0 protein (transmembrane)	
Peripheral myelin protein, PMP-22 (a proteolipid)	
Total lipid	70.0
Types of lipid:	
Steroid	
Cholesterol	19.4
Phosphoglycerides:	
Phosphatidyl cholines (lecithin)	7.8
Phosphatidyl ethanolamines (cephalin)	10.9
Phosphatidyl serines	3.4
Ether phosphatides (plasmalogens)	8.6
Phosphatidyl inositols	0.4
Sphingomyelins	5.5
Glycosphingosides (glycolipids):	
Cerebrosides	15.9
Sulfatides	2.7

Table 1 Percentage by dry weight of major myelin constituents

1.2. Myelin Imaging

Although there exist a number of techniques to visualize myelin in ex vivo preparations, interrogating the structure and composition of myelin in vivo is challenging. In clinical medicine, myelin imaging in humans is commonly conducted with magnetic resonance imaging (MRI) as it is a relatively sensitive and non-invasive technique. MRI provides millimeter-level resolution

imaging and is capable of imaging MS lesions in patients. Moreover, repeated imaging of patients allows the tracking of the progression of lesions in time and space allowing physicians to monitor the progress of the disease, and response to therapies.

1.2.1. MRI Techniques

MRI generates contrast in tissue by causing atomic nuclei to absorb and emit radio frequency signals in the presence of a strong magnetic field. In general, a radio frequency pulse is directed into the sample while the atomic nuclei are aligned with the magnetic field. In the magnetic field the nuclei precess like a spinning top with a frequency proportional to the strength of the field. The precession rate is termed the Larmor frequency. As the nucleus wobbles it emits a radio frequency signal which is collected and analyzed. The time required for the nucleus to realign with the magnetic field is the longitudinal magnetization recovery, known as the T1 time. The transverse signal, known as the T2 time, is dependent on the phase of the precession of multiple nuclei. When the nuclei spin in lock-step the T2 signal is strong. The decay is comprised of two general components: Intrinsic inter-nuclear interactions (spin-spin dependent on proximity of the dipoles) wherein excited nuclei interact with each other, and extrinsic localized Larmor frequency variation due to local magnetic field changes caused by tissue density and equipment interference with the static field. These extrinsic factors cause the T2 signal to decay at a rate faster than predicted by the spin-spin interactions, and the resulting shortened relaxation time is called T2*. Both the spin-spin and extrinsic field variability contribute to the T2* decay rate, while only the intrinsic spin-spin interactions contribute to T2. The T2 signal is retrieved from multiple T2* echoes, where the reduction in T2* signals over many acquisitions reveals the intrinsic T2 parameter. In medical use, MRI typically interrogates hydrogen nuclei. Hydrogen is

predominantly found in water and lipid so MRI imaging maps the location and concentration of both types of molecules. [43]

Quantitative T2 examines the compartmentalization of water within tissue by the variation of signal decay due to magnetization exchange between the water protons and their immediate surroundings. The measured decay is a combination of all of the decay rates present within a region of interest, but the individual 'pools' of water can be identified by fitting a weighted multi-exponential decay function to the recorded decay curve. Each exponential component of the fit corresponds to the decay time of one of the populations of water protons. [44]

In myelinated axons the T2 relaxation times for water partition into three groups; water in the cerebral spinal fluid (CSF) supporting the brain with a very long relaxation time (approximately 2 seconds), loosely confined water in the axon and extracellular space with a long T2 relaxation time (>70 ms), and myelin water with a short relaxation time (20 ms). [45] The short T2 component provides a readout of myelination and can be used to generate myelin water maps of the brain showing spatially resolved myelin density information. [46,47]

The duration of the myelin water signal is often too brief to collect with standard MRI equipment. The signal is usually indirectly detected through a phenomenon known as magnetization transfer (MT). Bound water signal is suppressed by applying an excitation pulse frequency-selective for the bound water. After excitation, the bound water exchanges with the free water pool, leading to a partial saturation of the free water pool signal dependent on the degree of exchange between the pools. This reduction in signal after bound water suppression indirectly indicates the presence of bound water.[48]

The selective excitation of the bound pool is achieved through an off-resonance radio pulse away from the Larmor frequency of the free water pool. The absorption of constrained water is

broadened compared to free water, as the strongly coupled macromolecule distorts the local magnetic field shifting the Larmor frequency. The off-resonance excitation pulse saturates the bound water which begins to exchange with the free water. Magnetization is transferred from the bound water pool to the free water pool, causing a decrease in the free water signal dependent on the rate of transfer, and is known as the magnetization transfer ratio (MTR). A low MTR is associated with damage to myelin and axonal membranes as the bound water is less able to exchange magnetization with the free water.[49]

Another powerful MRI technique, diffusion-weighted MRI, monitors the diffusion of water. This can be used to map the motion of water within an MRI image, a technique known as diffusion tensor imaging (DTI).[50] The flow of water in the brain is strongly dependent on the tissues confining it, and directional preferences can be used to map major axonal tracts in the brain. Axons are tubular structures, so water is inclined to diffuse along the length with a strong parallel directional preference. Regions where the directional preference is weak along an otherwise ordered tract may indicate localized damage where the water movement is no longer confined. This information can also be used to compute a fractional anisotropy (FA) value for a region, generally describing the degree of organization and the diffusion tendencies of water in different directions. [51]

1.2.2. Microscopy Methods

In the laboratory, staining of myelin with a chromophore or fluorophore provides microscopic details of structure. This provides more detailed information than the millimeter-scale of MRI methods, but requires direct access to the tissue. As a result these techniques are mainly used in cases of biopsy, autopsy, or in vitro cell or animal models of disease.

Compounds such as Luxol fast blue (LFB), in conjunction with hematoxylin & eosin (H&E) [52] have traditionally been used in pathology for viewing CNS tissue. These stains provide definition of morphology of the tissue and demyelination but are not specific or sensitive enough for detection of early biochemical changes. For instance myelin contains cholesterol and cerebrosides in abundance, but LFB does not bind to them and so cannot provide information on these components of myelin. H&E staining is useful for tasks such as quantifying the number of cells within a region and stains immune cells well, but provides no biochemical information of the environment.

Nile Red, Oil red O, or Sudan black [53,54] bind to lipids in the myelin and the density of staining provides a qualitative measure of myelin in a sample, however the staining can be non-specific and dependent on fixation of the sample.[55]

Treatments with fixatives, acids, bases, and solvents are often necessary to stabilize and differentiate tissues with these stains, and the protocols are often optimized for specific lipids or cell types. The colors and shading which appear are strongly dependent on the treatment protocol which requires consistence in applying multi-step chemical treatments, often with toxic substances. [36]

Antibody tagging of specific myelin proteins is another method of labeling myelin.[56] Typically an antibody tagged with a fluorescent molecule or chromophore is applied to the tissue. The antibody seeks and binds to an epitope such as a specific protein on the surface of the myelin. Common epitopes include myelin basic protein and proteolipid protein which make up the majority of the proteins present in myelin.)[57] To increase signal, a secondary antibody targeting the primary antibody contains the tagging molecule. The primary antibody binds to the epitope,

then numerous secondary antibodies, each carrying a fluorescent molecule or chromophore, bind to the primary to generate detectable signal, thus localizing the target of interest.

This technique can be used to provide highly detailed information regarding protein components on the surface of the myelin, although the results are highly dependent on the efficiency of the antibody binding process which limits staining to near the surface of samples.

Lipophilic fluorescent molecules do not require an antibody tag, as these compounds partition directly into the lipid-rich myelin structure. Examples include BODIPY, DiOC6, Nile Red and Prodan, which anchor themselves within the long acyl chains of the myelin lipids. The fluorescent excitation dipole of these molecules aligns with a fixed angle to the myelin structure. If polarized excitation light is used the fluorescence intensity becomes a function of the direction of the membrane and the constraint of the dye molecule within the structure, thus providing potential additional information on the nanostructural organization of the sheath. [58] [59]

1.2.3. Label-free Microscopic Imaging

Chromophore and fluorescent staining methods are powerful tools that can probe for specific structures and compounds within samples. The protocols for applying these techniques can be time consuming, and in the case of antibodies, expensive. Fluorescent molecules are also vulnerable to photobleaching,[60] limiting the number of times that a sample may be imaged. Importantly, virtually all techniques that rely on exogenous labels, require chemical processing and fixation steps, that may alter the morphological and biochemical properties in unpredictable ways, distorting the true structure and nature of the specimen being studied.

Label-free imaging uses an intrinsic property of the tissue to generate signal. This eliminates the need for applying a probe, but the presence of some natural signal source is required.

Autofluorescence [61] frequently occurs within living tissue providing a natural 'label' for deriving signal. The source of the signal is often non-specific within the sample as many biological substances generate autofluorescence leading to unwanted results and high background signals. The long unsaturated fatty acids present in myelin present a unique opportunity for generation of endogenous signal. The ordered CH_2 acyl chains are tightly bound in the lipid bilayer wraps with high packing density. Raman scattering is an optical property which is sensitive to molecular bonds. Light incident on the sample scatters in a way that interacts with the molecular bonds in the sample and causes a frequency shift in the scattered photons dependent on the vibrational energy of the bond. This effect is also sensitive to the orientation of the molecular bond, with signal dependent on the polarization of the incident light relative to the orientation of the molecule. However, the Raman effect is weak, making biological imaging impractical (ref). Coherent Anti-stokes Raman Scattering (CARS) is a non-linear optical method for probing Raman vibrations in molecules using laser-scanning microscopy techniques. Similar to Raman, CARS generates signal directly from the lipid bilayers contained in the myelin sheath by interaction with vibrational bond energies. The signal produced by CARS can be analyzed for intensity and polarization information which can reveal the degree of order and localized alignment of the constituent lipid molecules. Spectral information can be used to identify changes in the lipid content by detecting specific chemical bond energies that can change depending on the environment or biochemistry. This in turn may reveal information of the composition of the myelin as well as its integrity. This molecular disorder can be observed by the CARS process providing a possible indicator of myelin dysfunction without the need for a fluorophore or chromophore probe. However, unlike Raman scattering, CARS produces signals orders of magnitude greater than spontaneous Raman scattering, making CARS a very attractive

method for label-free imaging of fixed and living biological samples. Further details of the CARS process and its applicability to biological microscopy will be provided in chapter 2.

1.3. Statement of Hypothesis

Given the highly ordered nature of myelin and its constituent molecules/oscillators, the polarization dependence of Coherent Anti-Stokes Raman Scattering (CARS) microscopy can probe the structural organization of the myelin sheath surrounding nerves, without the need for exogenous probes. The polarization-dependent information will in turn provide a measure of myelin health or disruption. The signal-strength and polarization orientation of the CARS signal will decrease and become less polarized as the myelin becomes increasingly unhealthy and the organization of the lipids becomes more random.

Proof of principle samples of live and fixed myelinated tissues will be examined to compare the ability of CARS to determine myelin order at nanostructural levels not possible by other techniques. This order information will provide an indication of myelin changes at earlier time scales than would be evident from morphological changes visible in traditional methods.

2. CARS THEORY

2.1. CARS and Raman Background

CARS is a non-linear optical process sensitive to the vibrational frequency of molecular bonds. This sensitivity allows CARS to determine the abundance and in some cases orientation of specific vibrational modes within molecules. CARS is a form of Raman microscopy, so a discussion of spontaneous Raman will establish the groundwork for the description of CARS to follow.

2.1.1 Spontaneous Raman

Raman scattering is a linear optical effect wherein an incident photon inelastically scatters during interaction with a molecule. During the scattering event, the molecule is excited from the ground state to a virtual energy state. Upon scattering, the molecule reverts to a vibrational energy level rather than returning to the ground state, thus conferring less energy to the departing photon during the transaction. This process where the emitted photon possesses lower energy than the incident photon is known as Stokes scattering. Conversely, the molecule may already exist in an excited vibrational state and revert to the ground state after scattering. This imparts additional energy to the scattering photon and is known as anti-Stokes scattering.

The frequency shift of the scattered photon relative to the incident photon is measured to determine the vibrational energy which generated the scattering event. This energy delta is typically expressed in units of wavenumbers (cm^{-1}) as it is invariant relative to the frequency of the source. Observation of the Raman scattered photons provides a readout of the presence of molecular bonds and their degrees of freedom by comparing the energy loss to profiles of

reference molecules. The probability of a Raman scattering event is extremely low with only one in 10 million scattered photons experiencing a Stokes shift. Raman spectroscopy requires large numbers of photons and long collection times to acquire sufficient Stokes-shifted photons for analysis of the vibrational composition of a sample.

2.1.1.1 Presence of Raman lines in Matter

Raman scattering is not necessarily caused by all vibrational modes present in a molecule. A vibration will be Raman-active if the associated deformation of the molecule causes a change in its polarizability. This is dependent on the symmetry of the molecule and arrangements of the bonds. A motion around a point, line or plane within a molecule identifies an axis or plane of symmetry. If the associated motion leads to a change in polarizability, the vibrational mode can cause Raman scattering. Polar molecules, such as water, are less polarizable. Conversely, hydrophobic molecules are more polarizable because they are non-polar with homogenous net charge distribution. The distribution of charge around a molecule can be expressed by a polarizability ellipsoid, which can be thought of as a description of the volume occupied by the electron cloud around the molecule. Figure 2 shows a schematic diagram of the Raman polarizability of CH_2 as the bond vibrates. The motion of the hydrogen atoms extends the electron cloud around the molecule as represented by the polarization ellipse at the bottom of the figure.

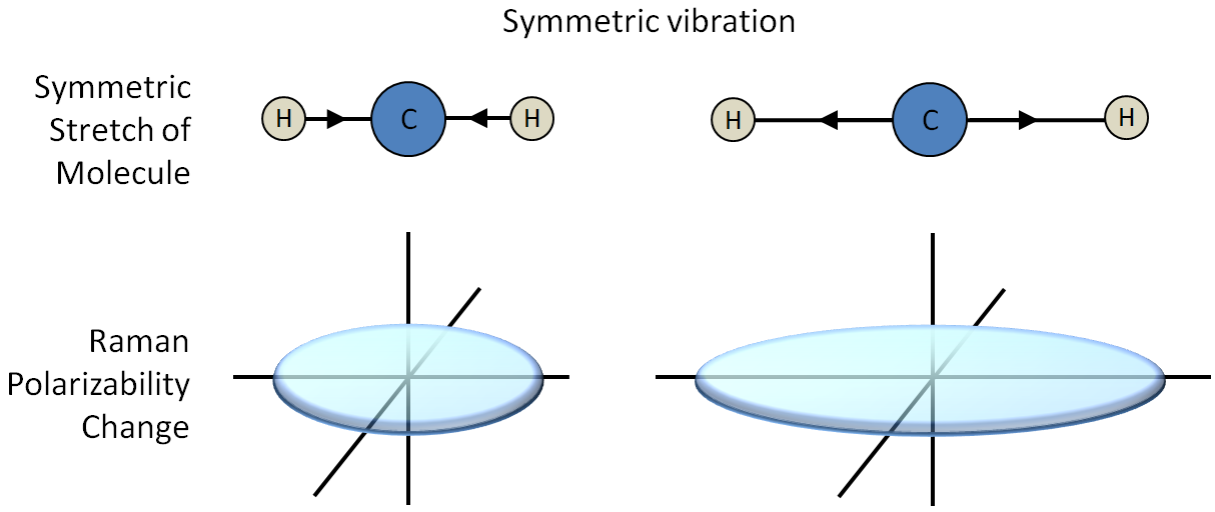

Figure 2 Change in Raman polarizability for CH_2 symmetric stretch. The displacement of the hydrogen atoms (top) stretches the electron cloud around the molecule as shown by the Raman polarizability change. If the hydrogen atoms were stationary and the carbon was to move, the polarizability would not change and the mode would not be Raman-active.

The displacement the polarizability ellipsoid is affected by the orientation of electronic bonds between atoms, as well as the mass of the nuclei, comprising the molecule. The degrees of freedom of each bond allow the molecule to vibrate in geometries specific to the bond type and mass of the atoms. This creates a vibrational energy signature specific to each possible direction of motion of the bond which influences the response of the molecule to an external driving field.

2.1.2 Coherent Raman

Rather than relying on infrequent spontaneous Raman scattering, a vibrational mode can be coherently driven by an external field to prime the polarizability of the molecule. The difference frequency between a 'pump' and 'Stokes' photon pair is selected to match the energy of a specific vibrational mode. The 'primed' mode is then interrogated by a third 'probe' photon leading to the generation of a stimulated anti-Stokes photon. [62] Figure 3 is an example of an

energy diagram comparing spontaneous Raman to CARS. The dashed arrows represent emitted signal while the solid arrows are excitation sources. In spontaneous Raman the Stokes signal results from the excitation light scattering off a molecular bond. In the figure the bond is highlighted by the horizontal orange line at the bottom labeled Ω_{vib}. The emitted Stokes photon (dashed red arrow) represents the energy-shifted photon. Note that the Stokes arrow is shorter than the leftmost excitation arrow, indicating the energy loss experienced in the scattering event. In the case of the CARS signal, the pump and Stokes (solid arrows labeled ω_p and ω_s) coherently drive the vibration Ω_{vib} and a second photon then probes the excited state, creating an anti-Stokes photon (blue dashed arrow) ω_{as}. The anti-Stokes photon is longer than the other arrows indicating it is a shorter wavelength than either excitation source. The non-resonant CARS signal is an optical process which occurs independent of the vibration creating a background signal, and will be explained in greater detail below.

The key advantage of CARS over spontaneous Raman is greater signal generation, with anti-Stokes photons generated at a rate of one in ten thousand. Compared to the one in ten million probability of spontaneous Raman scattering, CARS is stronger by five to six orders of magnitude.

The CARS process requires phase matching of the pump, Stokes and probe for generation of the anti-Stokes signal. The phase matching conditions are typically angularly tuned [63] with the three input beams delivered at various crossing angles to meet the necessary conditions. For tight focus applications, such as microscopy, all three beams can arrive at the sample through a high numerical aperture microscope objective. The short interaction length of the resulting tight focus relaxes the phase matching condition by limiting the interaction space of all three beams.

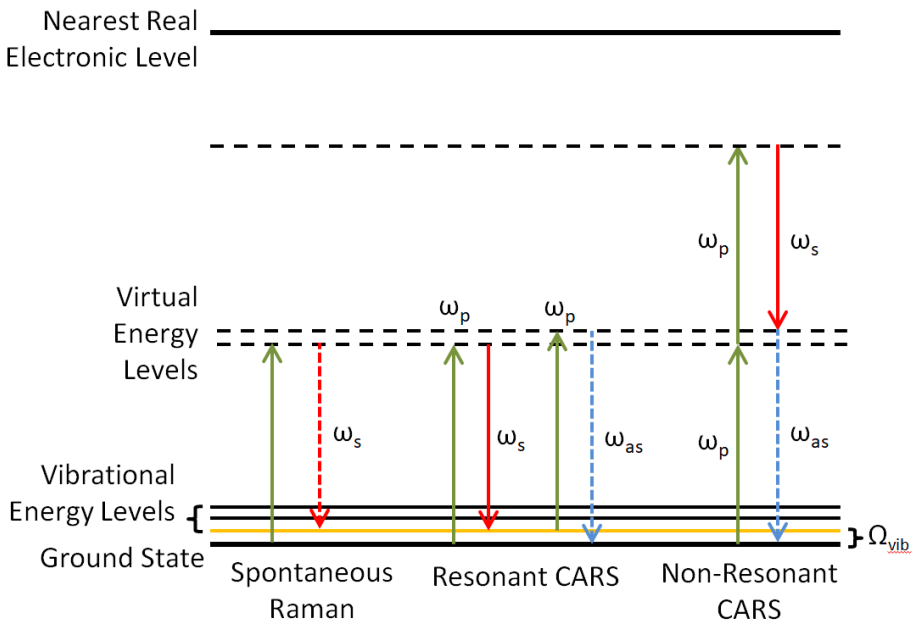

Figure 3 Energy level diagram for spontaneous Raman, and resonant and non-resonant CARS signal generation. Ω_{vib} is the energy of one of the vibrational states, highlighted in yellow. ω_p=pump frequency, ω_s=Stokes frequency, ω_{as}=anti-Stokes frequency. Dashed arrows indicate emission while solid arrows are excitation. Note that all three Raman processes require interaction with virtual energy levels, however resonant CARS couples to the real vibrational mode Ω_{vib} which has a finite lifetime unlike the virtual energy states.

The susceptibility of a sample is related to the combined polarizability of all constituent molecules. CARS signal is dependent on the third order susceptibility of the excited region which is the time-variant response of the index of refraction in response to the pump and Stokes excitation. The incident probe then interacts with the modulation and scatters to create the anti-Stokes signal.

The general expression for macroscopic polarization is expressed as a power series, with the various susceptibility terms for the interaction with an applied electric field:

$$P = e_o(\chi^{(1)}E + \chi^{(2)}E^2 + \chi^{(3)}E^3 + \ldots) \qquad [1]$$

Where e_o is the electric permittivity of free space. The first term in the series, χ^1, is the linear response related to absorption, reflection, dispersion, and other common optical phenomena. The higher order terms are dependent on the intensity of the driving field and involve a non-linear response to the electric field. The second term is typical of sum and difference frequency generation, second harmonic and optical parametric amplification while the third order term is related to CARS and related four-wave-mixing processes. Fourth and higher terms also exist, but are not shown here for brevity.

2.1.2.1 Externally Driven Oscillators

In the case of CARS, the χ^3 term is a function of the applied fields and the Raman vibrational modes of the sample. χ^3 can be expressed as a combination of resonant CARS and non-resonant four-wave-mixing processes:

$$\chi^{(3)} = \chi_r + \chi_{nr} \qquad [2]$$

The resonant contribution can be modeled as a damped harmonic oscillator in a driving field equal to the frequency difference between pump and Stokes. The solution to the damped harmonic oscillator is a Lorentz function with the phase component dependent on the difference in frequency between the resonant and driving frequencies. The solution contains and imaginary part, corresponding to the amplitude and linewidth of the resonant vibration, as well as a real part which is a result of the phase difference between the driving field (combination of pump and Stokes) and the resonance.

$$P = e_o \chi_r E_{CARS} \qquad [3]$$

$$P = e_o \frac{e}{e_o - 1} E_{CARS} = e_o (e_r - j e_i) E_{CARS} \qquad [4]$$

Where

$$e_r = A_p(\omega_r^2 - \omega_{ps}^2)/((\omega_r^2 - \omega_{ps}^2)^2 + \omega_{ps}^2 G_r^2) + 1 \qquad [5]$$

$$e_i = A_p^2 G_r \omega_{ps}/((\omega_r^2 - \omega_{ps}^2)^2 + \omega_{ps}^2 G_r^2) \qquad [6]$$

and ω_{ps} = pump-stokes difference which is the driving field, ω_r = resonance frequency, A_p = plasma frequency, and G_r is the resonant line width.

The magnitude of χ_r is therefore:

$$\chi_r = \sqrt{(e_r - 1)^2 + e_i^2} \qquad [7]$$

And the phase is:

$$\phi = atan \frac{e_i}{e_r - 1} = atan \frac{\omega_{ps} G_r}{\omega_r^2 - \omega_{ps}^2} \qquad [8]$$

The magnitude of the resonance is greatest with a phase of $\pi/2$ difference between the resonant vibration and driving field. After the resonance is primed by the pump and Stokes it can then be

interrogated by the probe wavelength scattering off the transient excitation in the electron cloud of the sample. Scattering of the probe is typically quantified with a Raman scattering cross section constant dependent on the material.

2.1.2.2 Non-resonant Background

Generation of CARS anti-Stokes signal is complicated by off-resonance transitions that can generate signal at the anti-Stokes frequency. This is independent of the targeted vibrational mode of the molecule and forms a constant background on top of the true CARS signal. As the non-resonant background is also coherent with the CARS signal, an interference term comprised of the mixing of the resonant and non-resonant signals is also present. (Equation 9) This mixing term can be derived from determining the CARS signal intensity from the polarization χ^3 term as the intensity is simply the square of the electric field:

$$I_{CARS} = |\chi^{(3)}|^2 = |\chi_r + \chi_{nr}|^2$$
$$= \chi_r^2 + \chi_{nr}^2 + 2\chi_r\chi_{nr} \qquad [9]$$

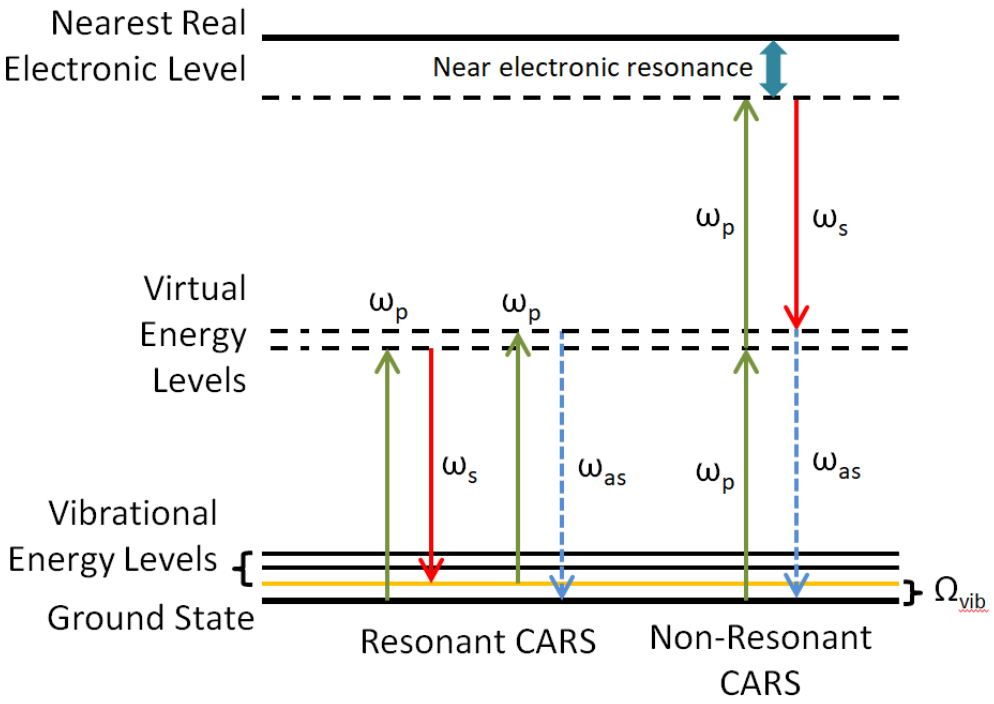

Figure 4 Resonant and non-resonant CARS energy diagrams showing enhancement of the non-resonant background by proximity to an electronic level. A virtual level that is near a real level can be enhanced by resonance increasing the probability of the transition.

The non-resonant background is enhanced when two-photon interaction of the pump is near an electronic resonance in the sample. Figure 4 shows the coupling of the highest virtual state in the non-resonant case with a nearby electronic level. A near-infrared pump frequency should be utilized to avoid proximity to two-photon electronic transitions typically corresponding to visible wavelengths. This also reduces the chance of possible autofluorescence from the electronic level.

2.1.2.3 CARS Variations

There are many configurations of CARS, each of which try to address the phase matching and non-resonant background limitations of the technique. CARS is a coherent process, which relies on constructive interference, so phase matching must be maintained over the interaction length of

the sample and the incident lasers. This is complicated by the index of refraction of the sample that will vary for different wavelengths, resulting in phase mismatches and spatial misalignments of the exciting beams.

Collinear CARS propagates pump, Stokes, and probe beams along the same spatial path through the sample. For this configuration, the 'walk-off' of the excitation beams and the anti-Stokes signal limits efficiency. If the sample is heterogeneous, local variability in the index of refraction can also unfavorably modify the phase matching distance. As such, collinear CARS is often best suited for homogeneous or thin samples where the optical path lengths are limited.

Crossed-beam phase matching (BOXCARS) propagates the excitation beams separately and crosses them within the sample. [64] While this limits the interaction distance, the crossing angles of the beams can be adjusted to compensate for walk-off within the excitation volume, improving efficiency. Additionally, the tight focusing of the beams drastically limits the interaction length of the constituent signals. Phase matching conditions must only be met over a very short distance depending on the numerical aperture, relaxing the overall phase matching conditions for efficient CARS signal production.

Both Collinear and BOXCARS can be performed with polychromatic sources. This technique uses lasers that emit multiple wavelengths along the same path. In the extreme case, a single continuum laser can emit all three excitation wavelengths, although it becomes difficult to manage the spectral content without complex coherent control techniques and spectral shaping. More simply, CARS can be performed with identical pump and probe wavelengths, allowing them to be provided from a single laser. A second laser then provides the Stokes. This reduces the phase matching complexity as pump and probe will have the same wave vectors, and is known as 'degenerate' CARS.

In addition to phase matching, CARS also requires delivery of precise pump, Stokes, and probe frequencies. It is desirable to excite a single vibrational mode at a time for molecular specificity, which requires a pump and Stokes frequency difference matched to the energy of the mode. Alternatively, broadband excitation may be used allowing multiple vibrational modes to be read out simultaneously. [65] An example of broadband excitation is shown in Figure 5. This multiplex excitation scheme requires spectrally-sensitive detection of the resulting broadband anti-Stokes signal, and the contributions of the individual vibrational components may be read out by a spectrometer. However, the broadband excitation increases the likelihood of non-resonant contributions which dilutes the resonant CARS signal. Figure 5 shows an example of broadband CARS with a spectrally narrow pump and spectrally broad Stokes. The wedged stripes replacing the arrows for the Stokes and anti-Stokes shown in Figure 4 indicate many frequencies are now present. The Stokes and anti-Stokes signals are now collections of wavelengths and therefore interact with an ensemble of vibrations ($\Sigma\Omega_{vib}$) rather than a single vibration as shown previously in Figure 4.

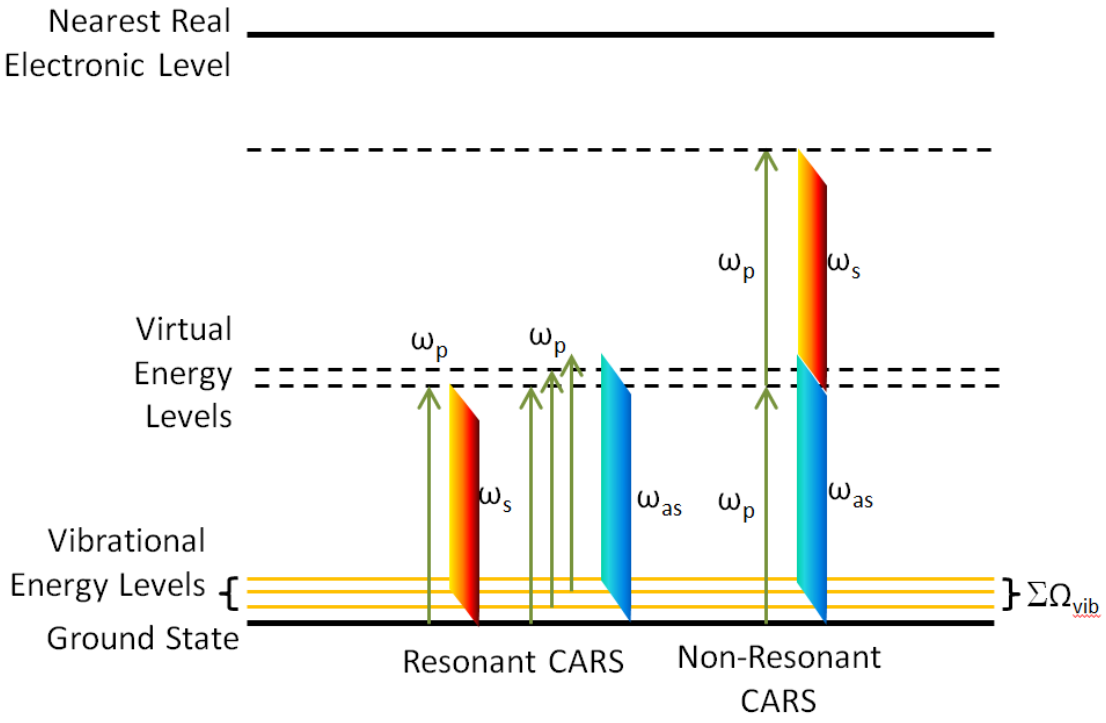

Figure 5 An example of CARS excitation with a narrowband pump and a broadband Stokes source. Instead of addressing a single molecular vibration, an ensemble of adjacent vibrational modes are excited as indicated by $\Sigma\Omega_{vib}$. Spectral detection can sort out the resulting multi-vibrational signal but non-resonant signal also increases as shown on the right.

The spectrum of the anti-Stokes signal will have a strong broadband non-resonant contribution. Non-resonant signal generation is independent of the vibrational bonds, so the entire spectral width of the Stokes is available to generate non-resonant signal. In the resonant case the energy which would excite one bond now interacts with multiple bonds, leading to a reduction in signal for any individual vibrational level.

Matching the frequency difference to one vibrational mode maximizes the resonant signal in a single vibration while decreasing the available energy combinations that could result in non-resonant background. Spectrally narrow excitation may be achieved either by using spectrally

narrow sources, or by ‘spectral focusing’ wherein broadband light sources are distributed across phase.

Spectrally narrowband CARS is straightforward to implement, as near-monochromatic laser sources are less impacted by chromatic aberrations or temporal dispersion. Picosecond lasers typically possess bandwidth on the order of only one or two nanometers or less, making them ideal for exciting a single vibrational mode at a time.

A disadvantage of picosecond lasers is that peak energy is limited by the duration of the pulses compared to femtosecond lasers. As CARS is a non-linear process, it is vitally dependent on pulse energy for efficient generation of the anti-Stokes signal. For a given signal intensity picosecond excitation will require greater average excitation power compared to a femtosecond laser. Previous examples of picosecond CARS have required pulse picking to reduce the repetition rate of the excitation to control the average power and avoid sample damage. [66]

Spectral focusing of broadband excitation provides the vibrational selectivity of narrow spectral excitation while retaining broad bandwidth. In this regime, femtosecond pulses with bandwidths on the order of tens of nanometers are spread out to picosecond durations. Careful control of the phase of the pump and Stokes pulses allows the instantaneous frequency difference to be maintained across the interaction of the two pulses. The selectivity of the excitation can be adjusted by altering the absolute chirp of the pump and Stokes excitation while maintaining a constant relative relationship between them. Increasing or decreasing the delay between the arrival of the pump and Stokes pulses tunes the instantaneous frequency difference, thus selecting a given vibrational mode within the sample for excitation. This is shown in Figure 6.

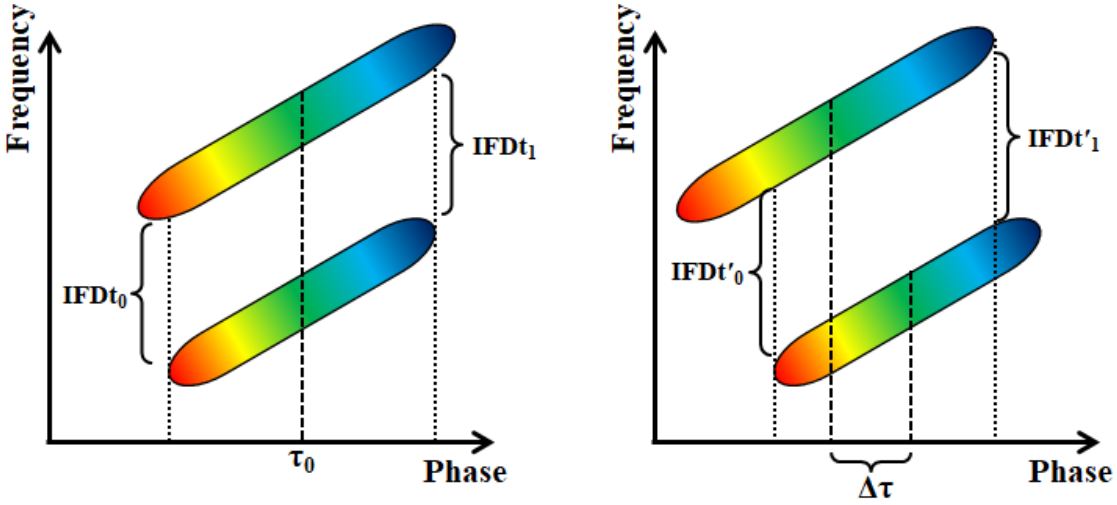

Figure 6 Matched frequency chirp of two pulsed broadband sources in frequency and phase. $IFDt_o$ = $IFDt_1$ = Instantaneous frequency difference between the two pulses. The IFD value can be increased by altering the time delay between the two pulses. This is shown at right as a time shift of Δτ. IFDt' at right is increased compared to IFD in the left example.

The disadvantages of spectral focusing include the need for careful control of pulse dispersion to maintain a controllable, matched chirp between the pump and Stokes. Additionally, as the sources are polychromatic, they are susceptible to chromatic aberration and spatial chirp, which complicates the necessary overlap of pump and Stokes frequencies in space. This can be overcome with achromatic optics, but high performance objective lenses are uncommon for the NIR wavelength range. [67,68]

The chirp rate of a single pulse is an expression of the change of instantaneous frequency with respect to time. A linear chirp is desired to maintain a consistent relationship between pump and Stokes pulses. Moreover, matching the chirp rate of both beams to the linewidth of the desired vibration optimally excites the bond: excessive chirp places too many spectral components outside the interaction time between pump and Stokes and the bond, resulting in loss of signal,

while too little chirp limits the ability to resolve the Raman line clearly from any neighboring vibrations.

Linear chirp of broadband pulses is typically achieved via grating or prism-based pulse compressors. [68] [69] Control of the dispersion is dependent on angle and distance of two or more optical elements. Misalignment of any of the optical components can lead to spatial chirp in addition to temporal chirp. In the case of spatial chirp, the frequency-phase relationship across the face of the travelling beam is not constant leading to inconsistent results. Additionally, any change of the center frequency of the beam requires angular realignment as both gratings and prisms are angularly dependent on wavelength.

Grating or angularly dispersing prism stretchers operate at a wavelength dependent angle, thus adjusting the wavelength of the source beam would require re-alignment of the stretching assembly. Conversely, a glass block at normal incidence is insensitive to wavelength. A single glass block of fixed length can only provide a fixed quantity of dispersion, although the trip may be repeated using external mirrors to internally reflect the light multiple times. The slight tilt necessary to angle the beam in the block may cause spatial chromatic distortion of the beam unless the path is perfectly reciprocal. A high index glass is desirable to give increased dispersion per unit glass length; however this aggravates any spatial chirp issues due to non-normal incidence on the glass surfaces.[70]

Long lengths of fiber optics can be used to provide large amounts of dispersion, but suffer from the same inflexibility as fixed-length blocks. Furthermore, focusing ultrafast pulses into fiber optics can lead to undesirable nonlinear optical effects as the energy density in the core of such a fiber can be quite high. This can lead to spurious signal generation, or more seriously, physical damage to the fiber. [71]

Alternatively, transmitting pulses through lengths of glass can induce positive chirp through simple material dispersion. This can be simpler to implement than grating and prism designs as the glass simply needs to be placed in the beam, but the fixed length of the glass precludes adjustability. Some designs use multiple interchangeable blocks of glass, or multiple trips through a single piece of glass, but this increases the alignment sensitivity of the system and increases the likelihood of accidental spatial chirp. [72]

A preferred approach would allow the compactness of a glass-based system with the adjustability of a grating or prism-based system. To achieve a space-efficient design the optical path must be folded within the glass in such a way to allow adjustment of the path length. Any such adjustments must be angularly insensitive to prevent accidental spatial chirp or overall misalignment of the beam. A custom dispersing prism solution with tight folding, alignment tolerance, and the ability to effectively insert over 1 m of glass into the beam in a small footprint will be presented in chapter 4.

2.2 Fingerprint vs. C-H region for biological samples

CARS and other Raman techniques seek to characterize molecules by examining the vibrational resonances of known subgroups within an unknown sample. These can include, for instance, various amides which possess a characteristic H-N-C=O moiety and are common in proteins. The orientation of the molecules is dependent on the conformation of the proteins, making amides useful for determining general structural details. [73]

While the amide groups are one example, there are many such vibrations within large molecules with many subgroups. The ‘fingerprint region’ contains vibrations with energies from approximately 500 to 1500 cm^{-1} yielding a complex signature of Raman active peaks. This

complexity is useful for identifying known specific molecules among many possibilities by comparison with a database. However, the numerous peaks create confusion for isolating the behaviors of a specific bond. Conversely, the C-H region from 2800 to 3100 cm^{-1} mainly contains contributions from the vibrational modes of CH_2 and CH_3, making it an ideal wavenumber range for examining the behavior of these bonds.[74]

2.2.1 CARS limitations in Biological Samples

The enhanced signal generation of CARS as compared to spontaneous Raman makes it viable for use in living samples. Spectroscopy of bulk gasses and liquids is straightforward as the sample is homogenous. However, live or preserved tissue is often very heterogeneous and can move during an acquisition. Different features within the sample create strong scattering effects, which disrupts delivery of the excitation beams.

2.2.1.1. Penetration Depth

Penetration into biological samples is limited by not only scattering, but index of refraction variations within heterogeneous tissue that disrupt the phase matching conditions required for CARS. This limits the depth at which CARS signal can efficiently be generated in such tissues. In addition, the anti-Stokes signal is likely to be a visible wavelength, which will scatter more than the NIR excitation. The scattering will decrease collection efficiency of the generated anti-Stokes signal at greater depths within tissue. [75]

Scattering before the focal point of the objective lens greatly disrupts CARS signal in focused imaging applications. Ranasinghesagara et al. [76] modeled the CARS signal in the presence of scattering objects between two lenses. Virtual test targets of 1 to 4 μm beads, and 2 μm diameter

myelin cylinders and myelin tubes were placed between the excitation lens and the focal volume to simulate the effect on the CARS emission. The presence of the scattering objects reduced the power reaching the sample plane, but also distorted the spatial phase of the light creating wide-angle hollow cone or wide saddle-shaped emission patterns rather than the more forward-directed signal simulated without any scatterers. This result indicates that CARS will be unlikely to penetrate more than a few layers of axons without significant signal reduction. This simulated case was for a forward-collected signal system, whereas the proposed system (to be presented in chapter 4) will use backscattered detection, so the result may differ from the simulated forward case.

Absorption can also lead to sample damage, although this can be somewhat mitigated by choosing NIR wavelengths with less absorption and using low average power delivery. Most biological samples are predominantly water, so selecting NIR wavelengths to which water is more transparent reduces absorption. Longer wavelengths reduce scattering, but the absorption of water also increases requiring a compromise between scattering and absorption. [66] This will be discussed further in chapter 3.

2.2.1.2. Acquisition Speed

The pixel dwell time limits speed and resolution for imaging Spontaneous Raman typically requires >100 ms for the acquisition of a single spectrum, requiring many minutes or even hours for even a low-resolution image. CARS typically requires ~100 μs to 1 ms for a similar acquisition, permitting high resolution images to be obtained in several minutes or less, or lower resolution images to be obtained at sub-second time scales. Depending on the technique, spatial

resolution and spectral resolution may be traded off to optimize for greater speed. Even video-rate imaging is possible if interrogating only a single resonance at a time. [77,78]

The acquisition speed of a CARS microscope is highly dependent on the repetition rate of the pulsed laser sources for pump and Stokes. The rendering of an image requires at least one pulse per pixel from each source, preferably more for a measure of average if the sources have any pulse-to-pulse instability.

The repetition of the laser sources limits the maximum imaging speed, but in reality the durability of the sample restricts the practical speed. If excessive, the average power delivered by the stream of pulses will damage the sample beyond a certain threshold. In many cases it is necessary to operate the system at a lower repetition rate than the maximum allowed by the lasers to prevent sample damage. Alternatively, higher pulse energy, lower repetition rate sources can be used to maximize CARS signal production while minimizing the average power deposited in the sample. [79]

2.2.2. C-H bonds in Lipid Bilayers

The long hydrocarbon chains in lipids consist of densely packed C-H bonds in an organized ladder structure. The acyl chains in particular contain CH_2 bonds at regular spacing and orientation, which leads to a resonant contribution of numerous oscillators within the excitation volume. [80,81] Additionally, the C-H Raman region, as discussed in Section 2.2, is also relatively sparsely populated making the specific vibrational modes of the C-H bonds easy to discern compared to competing resonances. [75]

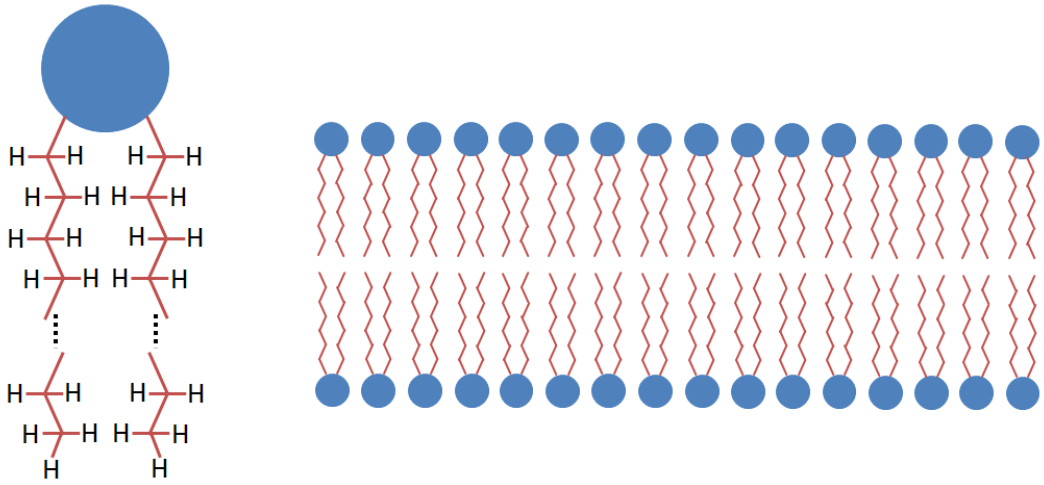

Figure 7 Schematic diagram of a lipid bilayer. The blue circles are the hydrophilic head groups while the red lines represent the hydrophobic acyl tails. The orientation of the hydrogen is shown on the enlarged molecule at left. For simplicity, the acyl tails shown here are all saturated carbon-carbon bonds.

The amphipathic nature of lipids coerces them to naturally self-assemble into bilayers and micelle structures in water. The hydrophobic tails orient inward and the molecules align into two mirrored rows with hydrophilic head groups present outward to the water. This natural packing orients the acyl chains perpendicular to the plane of the bilayer while the dipole of the CH_2 stretch is parallel to the bilayer. A schematic of this arrangement is shown in Figure 7.

As discussed in the Introduction, myelin can generally be described as a roll of multiple layers of lipid bilayer. In this configuration the CH_2 dipoles will be best aligned along the equator of the cylinder for linearly polarized excitation incident from the side of the cylinder. [75,80] Myelin will be best imaged in the longitudinal direction at the midline where the majority of CH_2 dipoles will be aligned to the plane of excitation.

2.3 Summary

In this chapter I described the basic theory of Raman scattering and extended it to non-linear CARS. The difference between narrow and broadband CARS has been described, and the combination technique of chirped broadband CARS, as applied in my project, has been presented. A model membrane was described to explain the orientation dependence of CH_2 with respect to the plane of the lipid bilayer. The next chapter will build on these concepts and consider demyelination, a cardinal feature of diseases such as multiple sclerosis, and how CARS imaging can be applied to study disorders of myelin.

3. LITERATURE REVIEW

Coherent anti-Stokes Raman scattering (CARS) spectroscopy and microscopy is a relatively new field that is rapidly changing. New techniques are constantly in development with new ideas reshaping the way CARS spectra and images are acquired. The evolution of the CARS field is tightly linked to the availability of new lasers, as new techniques are devised to take advantage of the latest available sources. This section will review the history of CARS, examining the strategies employed by researchers to create viable CARS imaging and spectroscopy systems. Some prior work in imaging of biological samples will be reviewed, and finally the relevant aspects of Multiple Sclerosis and related animal models used in this work will be summarized.

3.1 CARS Technical Development

CARS for imaging applications evolved out of its use as an analytical spectroscopic technique. The development of the laser in 1960 provided access to high-energy optical fields necessary for probing the non-linear behavior of materials. [82]

Maker and Terhune [62] used a flash lamp-driven pulsed ruby laser with pulse energy of 100mJ and 30ns pulse duration to study third-order non-linear optical effects. In addition to creating third-harmonic generation in calcite, Maker and Terhune also conducted three-wave mixing experiments in benzene generating the Stokes and anti-Stokes Raman shifts in the output light, as well as observing the nonresonant background. The authors also measured both the forward and backward-propagating signals, noting that the ratio was dependent on the Raman shift or overtone, and that in some cases it was completely forward-travelling. The theoretical

groundwork for the observations was also explained in the paper and formed the foundation for later work.

Little research would be conducted with Maker and Terhune's observations until the common availability of tunable dye lasers pumped by Nd:YAG sources. Dye lasers provided the key combination of tunability with high pulse energy necessary for stimulating Raman lines. Begley et al [83] would use such a source combined with the frequency-doubled pump laser to probe the anti-Stokes Raman spectrum of a mixture of benzene and toluene, adjusting the concentrations of each and noting the change in intensity of the peaks. The authors would also name the method "coherent anti-Stokes Raman spectroscopy" (CARS) as a nod to Maker and Terhune's earlier work that was conducted at a laboratory operated by the Ford Motor Company.

Chabay et al [84] used a pair of dye lasers pumped by a single nitrogen laser to construct a broadly tunable CARS apparatus for acquiring detailed spectra of bulk samples. A Foucault knife-edge test, where the edge of two razor blades was drawn through the combined beams of both lasers, was used as an early alignment tool to ensure coincident foci. This setup used a non-collinear geometry for the two beams, and the crossing angle limited the accessible bandwidth as the chromatic dispersion of the sample itself deflected the beams as the dye lasers were tuned.

A comprehensive review by Tolles et al in 1977 examined the implications of phase matching and the non-resonant background in CARS. [63] The review considered the coherent nature of the generation of the CARS signal and calculated a sinusoidal variance in signal strength with increasing path length. The resulting spectral line shape due to the coherent mixing of the resonant and non-resonant background was also compared to the spontaneous Raman response. The authors noted that the asymmetry was pronounced for even small amounts of non-resonant background proportional to the resonant signal.

Initial CARS experiments examined bulk samples of benzene or gas; however the ability of focused lasers to probe small volumes was quickly realized. Gustafson and Byer discussed the utility of small-volume CARS spectroscopy. They noted the ability of tight focusing to limit excitation volumes, although they mainly discussed the advantage of working with smaller quantities of expensive or hazardous samples. [85] A key point of tight focusing was the limitation of the interaction length in the CARS process, which simplified the phase matching issues brought up earlier by Tolles et al.

Duncan [86] used the concept of tight focusing and laser scanning to create a CARS microscope as early as 1982. A pair of picosecond dye lasers driven by a single mode locked argon-ion laser provided synchronized pulse pairs of moderate peak energy at 6 to 8 ps pulse duration. While Duncan managed some rudimentary imaging of deuterated phospholipid liposomes, [87] the non-resonant background greatly limited contrast. Some improvement was achieved by acquiring two images, one on-resonance (C-D bond) and one off-resonance and then performing simple image subtraction. The system was capable of imaging liposomes under 1 μm in diameter albeit with low contrast.

Zumbusch et al [87,88] improved on this with femtosecond pulse sources consisting of a Ti:Saph regenerative amplifier and optical parametric oscillator (OPO) operating at 250 kHz repetition rate. The output of the amplifier was split to act as the pump beam (855 nm) while driving the OPO to generate the Stokes wavelength (1.1-1.2 μm tunable). These sources were directed through a very high NA lens (1.4 NA) providing tight spatial confinement of the beams. The CARS spectrum was captured by adjusting the wavelength of the OPO in 2 nm steps while acquiring successive images. While acquisition was lengthy, with 20 ms required per pixel, a 512 x 512 pixel image could still be acquired. The primary speed limitation was the repetition rate of

the laser source combined with a photon counting detection scheme which further limited acquisition speed to avoid saturation.

The spectrum of a 900 nm polystyrene bead was collected from 2781-3163cm^{-1} with three major C-H Raman peaks distinguishable from each other. The higher peak energy of the femtosecond pulses (as compared to picosecond) and tight focus also generated stronger resonant signal, with the non-resonant background only being 5% of the resonant. The authors also recorded CARS images of live bacteria with this system and HeLa cells with submicron resolution, showing the potential of the technique for use in biological samples. Mitochondria were detectable within the HeLa cells due to their high C-H content, verified using fluorescence labeling with Rhodamine 123.

In 2000, Potma et al [89] used an advanced OPO system driven by a Ti:Saph laser with a pulse picker to reduce the repetition rate of the system to 800 kHz. The peak energies of the pulses were maximized with prism compressors to create minimum pulse width at the sample. Rather than tuning for C-H as performed by Zumbusch, Potma et al used the signal from water to visualize cellular dynamics. A combination of H_2O and D_2O was used to measure diffusion of water. The H_2O Raman peak was located at 3300 cm^{-1} while the deuterated water shifted the peak to 2800 cm^{-1}. The large wavenumber difference allowed the spectrally broadband CARS to distinguish between H_2O and D_2O and thus observe the exchange of the two liquids in living *D. discoideum* cells. A rapid line-scan along the equator of the cell was performed as the cells were flushed with an isotonic D_2O solution. The line scan was able to measure the efflux of H_2O from the cell and thus the membrane permeability to water. Two-dimensional imaging of entire cells was also performed, tuning to the O-H bond and capturing a micrograph of a single cell in 5 seconds.

In the search for better spectral resolution, Cheng et al in 2001 [90] constructed a CARS microscope system using two electronically synchronized picosecond lasers as pump and Stokes sources. With this approach both pump and Stokes were independently tunable giving good flexibility in the Raman shifts addressable by the system. The narrowband picosecond lasers generated 5 ps pulses capable of resolving an estimated 5.1 cm^{-1} allowing the discrimination of tightly spaced Raman peaks typical of biological samples. The authors noted the dependence of the resonant and non-resonant CARS signal strength to the pulse spectral width of the pump and Stokes. The non-resonant signal, comprised mostly of electronic contributions, had a quadratic dependence while the resonant CARS signal saturated rapidly with increasing spectral width. By choosing pulse widths of 5 ps, corresponding to 3.6cm^{-1} of spectral width, the authors maximized the ratio of resonant to non-resonant signal production.

Combined with a high NA lens, the twin 5 ps laser system produced high-resolution images of human epithelial cells imaged at 1570 cm^{-1}, which corresponds to Raman bands of proteins and nucleic acids. Image acquisition speed was primarily limited by the 400 kHz pulse-picked repetition rate of the lasers, stepped down from the natural 80 MHz repetition rate to reduce the delivered average power. The pixel dwell time was 4.88 ms per pixel limited by signal and averaging requirements as well as the low repetition rate of the pulse-picked lasers.[66] The interrogation of spectral information was limited due to the need to tune the wavelength of one or both of the lasers to change the difference between pump and Stokes beams.

Evans et al [78] vastly increased the acquisition speed of CARS images by forgoing pulse picking, and utilizing the full repetition rate of a 76 MHz Nd:vanadate laser providing pulses at 7 ps. Part of the laser output was used to drive an OPO to provide a tunable pump beam while the remainder of the 1064 nm light from the Nd:vanadate laser provided the Stokes beam. The

narrowband OPO provided narrow spectral resolution like the picosecond lasers used by Cheng et al., however changing the addressed Raman line required the retuning of the OPO wavelength. A rapidly rotating polygonal mirror provided a video-rate scan pattern, with pixel dwell times of only 0.16 μs. The rapid scan rate spread the energy of the lasers over a wide spatial area, limiting the energy any one pixel would receive and eliminating the need for pulse picking to reduce average power.

Another unique feature of the microscope was the collection of backscattered forward-propagating CARS signal. Previous designs used two lenses, one to deliver light to the sample and a second to collect the forward-propagating CARS signal transmitted through the sample. This limited CARS to imaging relatively thin mounted samples. While a weak back propagated Epi-CARS signal was imaged by some systems using a single lens, the signal was dependent on the presence of boundaries and symmetry breaks in the sample to create a backwards-traveling anti-Stokes signal. [91] By collecting back-scattered forward propagating anti-Stokes signal Evans et al took advantage of the stronger forward signal while exciting and collecting with only a single lens. This permitted the imaging of thick samples, and in fact exploited the scattering nature of many biological tissues to recover more forward-travelling signal.

3.1.1. Narrowband and Multiplex CARS

In 2006 a chapter in the third edition of the *Handbook of Biological Confocal Microscopy* by Xie, Cheng, and Potma [91] summarized much of the previous strategies for CARS microscopy. A key point of discussion was suppression of the non-resonant background, which was a consistent confounding factor for most CARS microscopy.

Narrow bandwidth picosecond pulses were the most straightforward to implement, with the limited spectral content of the excitation pulses limiting the band of excited Raman modes. The limitations of this approach are the ability to only address a single Raman resonance at a time, and the high average power to peak energy as previously discussed. [77,92] addressed the tuning limitation by using a rapidly tuning programmable picosecond laser to quickly adjust the Stokes wavelength. The system was electronically synchronized with the data acquisition system in the microscope, which was necessary as the programmable laser repetition rate varied from 12.35 to 13.98 MHz depending on the wavelength. Unfortunately the acquisition speed of the system was still limited due to the low peak power of the pulses, with multiple averaged frames necessary for sufficient signal-to-noise. The peak energy limitations of the system prevented full spectral images from being acquired although point spectra were feasible as well as image stacks acquired at a sparse number of specific resonances.

A femtosecond system with 20 fs pulses and a bandwidth of 75 nm was used by Dudovich et al for spectrally selective CARS imaging of Dibromomethane (CH_2Br_2) in a capillary plate. A spatial light modulator (SLM) was used to control the phase of the individual wavelength components of the pulses from a single laser source. Adjusting the phase of the spectral components across the 75 nm band of the laser using the SLM optimized either the resonant or non-resonant signal. While this did improve the spectral selectivity of the system, a spectral span of only 400 to 800 cm^{-1} was addressable due to the limited wavelength content of the source. The phase manipulation isolated the contributions from different spectral components within the pulse by fragmenting the main pulse into phase-shifted pulselets. This fragmentation greatly reduced the peak energy available for generating resonant signal.

Knutsen et al [93] took a simpler hybrid approach by combining a 100 fs pulse stretched out to 10 ps from an amplified Ti:Saph producing a transform-limited 100 fs pulse from an OPA driven by the same amplified Ti:Saph. A fraction of the pump light not necessary for driving the OPA was stretched by a pair of gratings to form the 10 ps pulse. Controlling the delay between the arrival of the 10 ps pump pulse and the 100 fs Stokes pulse selected the wavelength pair that would temporally overlap in the sample. Undesired wavelengths from the pump arrived before or after the much shorter Stokes.

Adjusting the arrival time via an optical delay line changed the effective spectral separation of pump and Stokes. The variable delay allowed the Stokes to arrive synchronously with different wavelength components from the stretched pump. The spectral resolution with this combination was calculated to be 3 cm^{-1} and the reported spectra of liquid methanol and iso-octane exhibited peak sensitivity of better than 5 cm^{-1} showing the separation between two CH_3 symmetric transitions at 2906 and 2901 cm^{-1}. In 2006 Knutsen et al [67] imaged plastic polystyrene bead samples dispersed on a glass coverslip with this fs-ps combination, but the speed of image acquisition was greatly hampered by the 1 kHz repetition rate of the amplified Ti:Saph and OPA source resulting in a 50 ms/pixel dwell time.

The combination of one stretched pulse and one transform limited pulse provided excellent spectral resolution, but the overlap of a very short pulse with a very broad one meant that much of the energy in the broad pulse was wasted. Hellerer et al [68] addressed this issue by chirping both pump and Stokes pulses equally. This allowed the pulses to overlap in time while the phase distribution of their spectral bandwidth restricted the interaction of the various wavelength components contained in both pulses. The laser sources were a 170 fs amplified fs laser at 798 nm for the Stokes which also drove an OPA, frequency doubled to the range of 550-800nm to

provide the pump. The repetition rate of the system was 250 kHz, and the pulses were stretched to 12.4 ps for the pump and 5 ps for the Stokes pulses. The relative arrival times of the two pulses were controlled by a delay line as per Knutsen. The system achieved a 12:1 resonant to non-resonant signal ratio and was able to clearly resolve spectral peaks in C-N spaced 15 cm^{-1} apart.

Rocha-Mendoza et al [72] further simplified this concept by using glass blocks of preset length to chirp femtosecond pulses out to picoseconds via material dispersion. Similar to Hellerer's work, the applied chirp controlled the bandwidth of the instantaneous frequency difference (IFD) between the two pulses, and the time delay between the arrival of the pulses controlled the effective center frequency difference. The pump and Stokes sources were a Ti:saph laser providing the Stokes pulses at 832.5nm while also driving an OPO to provide pump pulses from 700-650nm with a repetition rate of 76 MHz.

The advantages of the glass dispersion as compared to grating dispersion was the better transmission of the former, passing 70% even for the longest path length as compared to 50% typical of a grating-based system. The straight beam paths through the blocks were also more alignment insensitive as compared to a grating design and were thus simpler to construct and align.

A fiber optic-based stretcher by Cleff et al [71] provided large amounts of chirp by propagating the pump and Stokes beams through multi-mode, then single mode fiber. The beams were propagated down separate fibers to prevent non-linear mixing effects from occurring within the fibers and creating undesirable wavelength content by premature mixing of the pump and Stokes pulses.

The sources used by the authors consisted of an amplified fiber laser providing the Stokes beam at 1050 nm, with part of the light used to drive an OPO to generate a pump beam tunable from 765 to 940 nm. The pulse widths of the sources varied from 250 to 100 fs from the OPO dependent on center wavelength, while the residual fiber laser pulse width was 300 fs. The high energy output of the fiber laser required a two-stage fiber stretcher, with multimode fiber for the first stage stretching the pulse out prior to injection into a singlemode second stage. The larger core diameter of the multimode fiber allowed the peak energy of the pulse to be reduced before the pulse was injected into the narrower core of the singlemode fiber. This prevented undesirable nonlinear optical effects from being generated in the singlemode fiber by avoiding direct injection of a short pulse.[94]

An additional complication to the fiber chirp setup was the inability to repeatably adjust the applied dispersion. The authors selected a fixed fiber length for the pump beam at 510 cm providing a group delay dispersion (GDD) of 2.15×10^5 fs^2, while the Stokes fiber was permanently modified from 950 to 440 cm, by cleaving the fiber shorter in 20 cm increments while recording the Raman spectra of polystyrene and eugenol samples and tuning the OPO. The delay between the pump and Stokes had to be continually adjusted while the OPO was tuned, as the path length of the fiber was wavelength-dependent.

3.1.2. Polarization CARS

Historically, polarization effects in CARS spectroscopy have been used to suppress the non-resonant background, and as a probe of molecular order in samples.

Raman bands excited by polarized excitation emit with a component both perpendicular and parallel to the exciting field. The difference between these is known as the depolarization ratio.

The degree of depolarization depends on the symmetry of the molecule and the resonant mode. [95-98]

In an isotropic sample such as a liquid, the relative polarization of the pump and Stokes beams can be adjusted to create an angular separation between the resonant and non-resonant signal by exploiting the depolarization ratio. [99-101] This allows suppression of the non-resonant signal by placing an analyzer at 90-degrees to the emitted polarization. Oudar et al [102] implemented such a system in 1979 with waveplates and polarizers to control the relative polarization angle between pump and Stokes into a sample of benzene in carbon tetrachloride. The authors used the X and Y components of the nonlinear susceptibility of the medium and calculated the expression for the effect of the angle between the pump and Stokes on the resulting X-Y components of the non-resonant signal. Then with straightforward geometry they derived the signal detected through an analyzer as dependent on the pump and Stokes angular separation. The authors found the best conditions to be 71.6 degrees between pump and Stokes, with the analyzer aligned at 135 degrees relative to the pump.

While this method provides excellent contrast between the resonant and non-resonant CARS components it is not without its limitations. Cheng et al used polarization detection [90] to image lipid vesicles and gather CARS spectra of the CH_2 and CH_3 symmetric and asymmetric stretches.[65] The analyzer method was only effective for suppressing the non-resonant background for the CH_2 symmetric stretch at the cost of almost an order of magnitude loss in resonant signal strength. The CH_3 and CH_2 asymmetric stretches were incompatible with background suppression as the angle of emission of these bands was different from the optimal.

The polarization-dependent background subtraction method is dependent on maintaining the polarization state of the generated CARS and non-resonant signals. The analyzer in the detection

path is rotated orthogonally to the linear angle of the non-resonant background, rejecting it while allowing detection of the resonant CARS signal. In a scattering sample the polarization separation between the resonant and nonresonant components may not be maintained which will reduce the effectiveness of this method. [103] The required large separation angle between pump and Stokes also reduces the interaction of the excitation generating less overall signal.[104] In the event that the analyzer is unable to separate resonant and nonresonant contributions, the signal-to-noise gains of the technique will be lost to the overall lack of resonant signal.

The polarization dependence of CARS is also useful for determining the dipole orientation of Raman-active molecules. The vector components of the non-linear susceptibility of a molecule can be interrogated with controlled known polarization states of pump and Stokes. The simplest case, employed by Bélanger et al[105], circularized both pump and Stokes beams to remove the polarization dependence of the CARS response. This excitation regime eliminates any directional preference in the excitation providing a uniform emission. Images produced with this method lack directional artifacts and equally excite samples independent of orientation. This is ideal for imaging morphology but sacrifices any anisotropy or orientation information.

Cleff et al [106] used circular polarization to probe the symmetry of CARS resonance rather than normalizing angular signal intensity as per the case of Bélanger et al. The majority of polarization-resolved CARS techniques consider the Cartesian components of the nonlinear susceptibility of the Raman response. Cleff et al instead expressed the nonlinear susceptibility as a set of spherical harmonic functions, which could be probed with circularly polarized light. This provided a readout of the molecular symmetry of the sample by measuring the clockwise and counterclockwise components of the forward-propagating CARS signal simultaneously with two circular polarization-sensitive detectors. The anisotropy of the CARS signal is determined

by alternating the pump and Stokes beams between matched and counter circular polarization states to probe isotropic (matched circular) and ordered (counter circular) organizations of CARS emitters respectively. This method is convenient in that only two images are required (same and counter-rotating polarizations), however the circular polarization state of the anti-Stokes signal must be maintained for detection. For back-detected configurations or thick samples this is not possible, limiting application of the technique to thin sections.

Turcotte et al[107] applied the opposite approach, using collinearly polarized pump and Stokes to probe the population orientation of CH_2 in myelin[108] in developing zebrafish spinal cord. The excitation source consisted of a picosecond Nd:Vanadate laser and optical parametric oscillator with pulse repetition of 80 MHz. The polarization of the excitation light was rotated in 10-degree steps using a motorized waveplate rotator with an image acquired at each step. The intensity ratio of strongest and weakest CARS signal strength over the collected polarization angles was taken as a measure of anisotropy. This method did not require the polarization state of the anti-Stokes signal to be preserved, and in fact the detection method was polarization insensitive to avoid artifact due to polarization distortions from the sample or collection optics.

The authors examined embryonic spinal cord myelin at three and five days post fertilization and noted that the ratio (dubbed the 'Myelin Modulation' index) increased by a factor of three between the two time points. The increasing ratio implied a stronger orientational preference within the more mature myelin, indicating increasing organization as the myelin sheath developed.

Turcotte employed a video-rate scanning system, however acquisition speed was limited both by the need to rotate the polarization of pump and Stokes and considerable frame averaging (15-frame average at 15 frames per second) to achieve minimum acceptable signal-to-noise. The

measurement required an average power of 60 mW at the sample, which while high is non-destructive in this case due to the rapid scan rate.

Kennedy et al[80] examined not only the organization of lipids, but of water molecules. Their system employed a parallel pump and Stokes excitation regime omitting the analyzer in the detection path. The sample was a myelin figure constructed from triethyleneglycol lauryl ether ($C_{12}E_3$), a surfactant that self assembles into cylindrical layers in distilled water under capillary force. This structure formed concentric cylinders of lipid bilayers around a water core. The overall structure approximates the acyl chains and hydrophilic head groups of natural myelin. Imaging of the samples was performed at 2840 cm^{-1} for CH_2 symmetric and 3200 cm^{-1} for water. The pump and Stokes were maintained in parallel; the excitation was aligned sequentially parallel or perpendicular to the 'core' of the sample. Detection was transmission type with a second objective lens and detector to collect the forward-propagating CARS signal on the opposite side of the sample from the lens delivering the excitation light. The authors confirmed that the collected signal was a combination of resonant and non-resonant contributions and the non-resonant signal was background subtracted using empty areas adjacent to the sample as a reference.

The CH_2 symmetric signal was found to be most intense with the pump and Stokes aligned along the axis of the cylinder. Z-stack imaging was performed, and the signal was found to be most intense when the optical plane transected the middle of the cylinder when the cylinder was lying sideways to the incident excitation. At this point in the structure the radially arrayed CH_2 bonds in the acyl chains were best aligned with the incident polarization fields. Signal dropped off rapidly above and below the center of the cylinder as the acyl chains outside that depth were rotated out of the optical plane. The 3200 cm^{-1} OH water response was found to be perpendicular

in orientation to the CH_2 vibration, with water molecules trapped between the membrane layers aligning perpendicular to the membrane surface instead of parallel. This highlighted the interaction between the polar water molecules and the hydrophilic polar head groups of the lipid molecules in the membrane.

The orientation of the Raman-active CH bonds within acyl chains is typically discussed from a macroscopic manner, however Bioud et al [109] examined the resonant contributions from multiple CH and C-C bonds within lipid molecules and examined the impact of the ensemble of bonds on the CARS response. The authors considered a rotational decomposition of the CARS signal similar to the method of Cleff et al to determine the contributions of individual dipoles to determine the angular spread of resonances. The authors predicted that the distribution would form a Gaussian function, the width of which would depend on the angular distribution of the acyl chains within the ensemble of molecules within the excitation volume. The model was tested experimentally in multilamellar vesicles comprised of phosphocholine (DPPC) lipids as well as coronal acute slices of mouse spinal cord. The imaging system acquired multiple CARS images while rotating collinearly polarized pump and Stokes beams (unlike Cleff et al who utilized circularly polarized beams) over 180-degrees in 6-degree steps. The emitted CARS signal was detected in the forward direction and resolved into clockwise and counter-clockwise polarization states as per the method of Munhoz.[110] The system pixel dwell of 50 μs limited the image size to 100 x 100 pixels to acquire the entire polarization 'stack' within a reasonable time frame, as sample motion would create artifacts in the collected polarization-dependent signal. The authors concluded that the distribution of resonances, particularly in the myelin samples, followed a higher-order (super) Gaussian function with a flat top rather than the predicted first-order Gaussian distribution. The authors surmised that the broader-than-expected distribution

may be due to morphological heterogeneities, such as folded membrane layers, and the variety of different lipids and molecular packing regimes.[111]

Gasecka et al [112] would apply the circular decomposition method of Cleff and Bioud to an autoimmune demyelination model using the experimental autoimmune encephalomyelitis (EAE) protocol in mice. The goal of the work was to determine molecular alteration of the myelin following immune-mediated damage to myelin in the spinal cord. The authors also compared fresh tissue samples to paraformaldehyde-fixed and found no change in anisotropy results as a result of fixation. This indicates that the protein-based cross-linking of fixation does not interfere with the lipid distribution in the myelin samples. The authors were able to determine increasing disorder compared to increasing clinical scores of the EAE mice, where increasing EAE score indicates increasing evidence of neurological dysfunction as assessed by observation of the animals. Regional differences were also noted, with different myelin features (swelling, blebs, inclusions) exhibiting different scores of molecular order, not only compared to 'normal' myelin, but between differing features.

Disorder was measured as a Gaussian distribution with the width increasing with disorder, however the results also indicated a strong isotropic signal, approximately 25% of the ordered signal, which caused underestimation of the symmetry. The isotropic signal was attributed to a strong nonresonant CARS background signal, which would not exhibit the directional preference of the CH_2 vibrational resonance. The strong non-resonant background may have been due to the use of broadband pulses (150 cm^{-1}) in the system with no dispersion manipulation. It is also likely that both the symmetric and asymmetric CH_2 vibrational modes would have been excited with this regime. The asymmetric mode has a reduced response to polarization as compared to

the symmetric mode as will be shown later in this work. This would increase resonant polarization-insensitive background in the acquired data as well as the non-resonant background. Acquisition speed is a major limitation in the previously presented works, with the time to manipulation polarization compounded by long pixel dwell times (on the order of 20 μs or longer) for imaging. The rotation of the polarization of colinearly-polarized pump and Stokes requires rotation of one or more waveplates requiring delays on the order of seconds for typical servo rotation mounts. To address this limitation, a high-speed polarization scanning technique was developed by Piazza et al [113] that rapidly rotates the polarization state of the linearly-polarized pump using a free-spinning waveplate rotating at 10 Hz. The constantly-changing polarization is discriminated by use of a lock-in amplifier detection scheme synchronized to the rotation of the waveplate. Spectral selectivity was maintained by initially narrowband-filtering the incident femtosecond pump beam with two successive 3 nm bandpass filters (later [114] replaced with glass block spectral focusing as will be discussed in the next section). Unlike the pump, the Stokes source was circularly polarized. The authors took this approach as the attempting to use the spinning waveplate to rotate both the pump and Stokes simultaneously would cause ellipticity in the Stokes light due to the wavelength difference between the beams. Achromatic waveplates only approximate their value over a small wavelength range and so the optimum retardance value can only be selected for one of either the pump or Stokes. Two different waveplates, each wavelength-matched to each beam could be utilized, but the authors eschewed this approach, noting the difficulty in synchronizing the rotation of two separate elements with the lock-in acquisition.

Myelin samples in the form of fixed wild type mouse brain sections were examined using the rotating excitation system. The phase signal from the lock-in amplification determined the

relationship between intensity and excitation angle, and an anisotropy value consisting of the minimum and maximum intensity was calculated for each pixel. This technique rapidly determines a ratio of the directionally dependent CARS signal, but does not consider the ensemble of emitters within the focal volume, which would require analyzing the angular spread of the signal.

The dominant direction and ratio information was determined at the pixel level for images of coronal mouse brain section. This showed the parallel relationship between the CH_2 vibration and the myelin in longitudinal tracts, although the authors did not comment on the anisotropy and instead noted the overall dominant angle within each pixel. While the continuously rotating pump polarization was intended to speed acquisition times, the integration time of the lock-in amplifier was a significant limitation of the system speed. Integration times were in excess of 20 ms resulting in acquisition times of 200-500 seconds for a 100 x 100 pixel image, actually resulting in slower performance than the previously discussed rotating CARS methods. A later software method to eliminate the lock-in amplifier would attempt to improve this acquisition time but still only achieve a pixel dwell of 6.4 ms.[115]

In a later work [116] Piazza and colleagues would examine the anisotropy more closely by exposing sciatic mouse nerve to lysophosphatidylcholine (lysolecithin), which is known to induce demyelination.[117] The anisotropy ratio of brightest to dimmest angularly dependent signal was compared to the g-ratio of selected myelin tracts. The g-ratio is a comparison of the inner and outer diameters of myelinated axons and provides a method to quantify the overall myelination of a nerve. In this case, the g-ratio was calculated from both normally appearing and swollen sections of the sheath leading to a decreasing g-ratio as the lysolecithin-induced damage progressed. The authors found that the CARS-measured degree of order averaged over an axon

decreased in correlation with the g-ratio for that axon. Further work in a more recent paper by the same group [118] examined the myelin of Twitcher mice, an animal model of Krabbe disease. Both the Twitcher mouse model and Krabbe disease in humans exhibit inactivation of galactocerebrosidase, which is an enzyme necessary for the catabolism of various galactolipids. This results in the death of Schwann cells and oligodendrocytes, causing progressive demyelination. The authors compared five wild-type mice to seven Twitcher mice by excising sciatic nerves without fixation and immediately imaging with the polarization-resolved CARS system. The anisotropy ratio was collected on a pixel-wise basis for images of both groups of mice. Compared to wild type, the Twitcher mice sciatic nerves exhibited greater anisotropy as measured by polarization-resolved CARS. The authors also noticed that pixels located within normal-appearing axon walls for Twitcher samples had great variability in their anisotropy values. This implied a sub-microscopic change in the myelin that would not have been evident without an anisotropy-resolved technique.

Further comparison of the techniques presented in this review to the work presented in this paper will be included in the discussion.

3.2 CARS of Biological Samples

Biological samples present many difficulties compared to simple bulk samples for CARS imaging: The heterogeneity of biological tissue can disrupt the spatial or phase overlap of the pump and Stokes; the fragility of tissue places limits on laser powers and acquisition times, leading to weaker acquired signal; and sample motion (for live samples) can create imaging artefacts.[119]

CARS offers increased sensitivity compared to spontaneous Raman, intrinsic signal generation without requiring the addition of a tag or fluorophore to a sample, inherent 3-dimensional sectioning when used with high NA lenses, and NIR operating wavelengths which decrease tissue damage and increase penetration into scattering samples compared to visible light methods such as confocal fluorescence. The NIR excitation also benefits from avoiding electronic transitions levels, and in fact CARS operates primarily in vibrational energy levels off the ground state. This avoids multiphoton electronic transitions that might induce photo-damage in a biological sample. [120]

Fu et al [79] examined the photo-damage induced in a spinal cord preparation by repeated imaging using two 2.5 ps synchronized Ti:Saph lasers tuned to 704 and 880 nm. A pulse picker was used to reduce the repetition rate to between 3.9 to 7.8 MHz and an average power of 8.8 mW at 7.8 MHz. At a scan rate of approximately 1 frame per second no structural damage was observed in the myelin sheath.

The authors used a point scan to induce damage intentionally by dwelling the laser on a single point within the sample. The lasers were allowed to dwell directly on the wall of a myelin sheath with an average power of 13 mW for 22 seconds for one sample and 25 seconds for a second sheath. The estimated power density in the laser spot was 2×10^{11} W/cm^2. The effect on the sample was highly apparent, with the myelin sheath disrupted from concentrated exposure to the beams. The authors also recorded an intense broadband continuum emission from the sample, most likely plasma formation.

The dependence on wavelength was also examined by varying the power between the pump and Stokes beams. The average power of both beams was adjusted to maintain a constant CARS signal while the ratio of pump to Stokes power was varied from 0.37 to 2.0. The authors found

that the shorter wavelength pump increased photo-damage, with a tripling in the rate of damage between 1:2 and 2:1 ratios of pump to Stokes.

Finally, the authors tested the effect of repetition rate on photo-damage by varying the pulse picker from 0.65 to 39 MHz. The lowest photo-damage rate was found to be at 0.975 MHz, increasing slightly between 1.5 to 2 MHz, but with a sudden increase in photo-damage beyond 2 MHz.

Galli et al [121] used endogenous autofluorescence of samples as an indicator of damage during CARS and two-photon imaging of human cerebellum. The authors found that autofluorescence increased with visible structural damage to the tissue. While the exact cause of the increase in autofluorescence with exposure to the laser was not known, the authors speculated that it was a photochemical reaction. The damage to lipids appeared to be particularly correlated to the increase in fluorescence signal, and it was noted that lipid peroxidation produces highly reactive compounds that could crosslink with amines to produce fluorescent compounds.

Ex vivo imaging of cerebellum with CARS at 2850 cm^{-1} and fluorescence collected from 500-550 nm showed a decrease in lipid signal and an increase in green autofluorescence with sequential scans. The power threshold for this effect was measured at 52 mW, with images taken at this power only showing autofluorescence increase after 60-100 scans. The authors observed that adequate imaging results could be achieved with as low as 5 mW on the sample with no visible decrease in lipid signal or increase in autofluorescence (indicative of photodamage) when imaging sequentially. Even at 20 mW of power the authors did not observe any effect even after 10000 scans.

3.2.1. Myelin imaging with CARS

CNS and PNS tissue is a complex mixture of mainly water, proteins, and lipids, which is highly scattering. Imaging through such a sample is challenging enough, but attempting to propagate a pair of phase-matched laser beams of differing wavelengths is even more so. The first consideration is the transmission of pump and Stokes wavelengths through the tissue, as this will not only influence the successful juxtaposition of pump and Stokes at the focus, but also influence energy deposition into the sample, which could lead to damage.

Yaroslavsky et al [122] investigated the transmission and scattering of human brain tissue from 360 to 1100 nm, including white matter, grey matter, cerebellum, and brainstem tissue. The authors determined the absorption and scattering coefficients from experimental data. A xenon lamp with a monochromator was used as the light source, sweeping over the spectrum of the lamp with a 10 nm bandwidth. A collimated detector in the forward direction measured transmission, while an integrating sphere measured the total scatter. Yaroslavsky found a general decrease in absorption with increasing wavelength, however the trend reversed slightly between 800 and 1100 nm, with absorption slightly increasing over that range. For white matter and cerebellum, scatter decreased rapidly from 350 to 600 nm, and then remained at a relatively flat value out to 1100 nm. For grey matter scatter dropped similarly to white matter from 350 to 600nm, then very slightly increased by ~10% at 1100 nm.

As water and lipid are the most abundant substances in and around myelinated nerves, examining the absorption spectra of both provided insight to the total absorption. Given that myelin is mostly comprised of lipid and water, sample heating and photo damage can be avoided by selecting pump and Stokes wavelengths that have minimum optical absorption. Water absorption data collected by Hale and Querry [123] confirmed a local maximum at 970 nm reverting to a local

minimum by 1060 nm, and then rapidly increasing with wavelength after that. Interestingly, fat absorption data collected by van Veen et al [124] showed a sharp local maximum at 930 nm followed by a deep local minimum at 980 nm, and then increasing to a local maximum at 1040 nm. The presence of an absorption maximum in the water spectrum and a minimum in the fat spectrum between approximately 960 to 980 nm was a surprising contradiction, although little additional data on fat absorption could be found to verify these findings. The minimum in the fat spectrum in particular was very pronounced, with a factor of five between 980 and 1040 nm in the recorded absorption coefficient. The data sets from both papers are illustrated in Figure 8, below. The absorption trough at 975 nm for fat indicates a possible transparent window to minimize absorption of lipid when selecting the Stokes wavelength for CARS imaging.

While data on the scattering and absorption of myelin was found to be sparse, the Raman spectrum of key lipids found in myelin is well characterized. For CARS imaging of myelin it is important to know the Raman response of the vibrational modes characteristic of the lipids to identify the chemical bonds being addressed. Chongsoo and Bain measured the fingerprint and lipid Raman spectrum of pure samples of dimyristoyl phosphatidylcholine (DMPC) and dipalmitoyl phosphatidylcholine (DPPC), in the form of lipid films on glass, recording lipid region and fingerprint region spectra for both.[125] They found the CH_2 symmetric stretch at 2851 cm^{-1} to be the strongest for both lipid samples. In the fingerprint region the 1453 and 1441 cm^{-1} CH_2 scissoring mode was the strongest, but the symmetric 2851 cm^{-1} response was over 20x stronger in measured intensity.

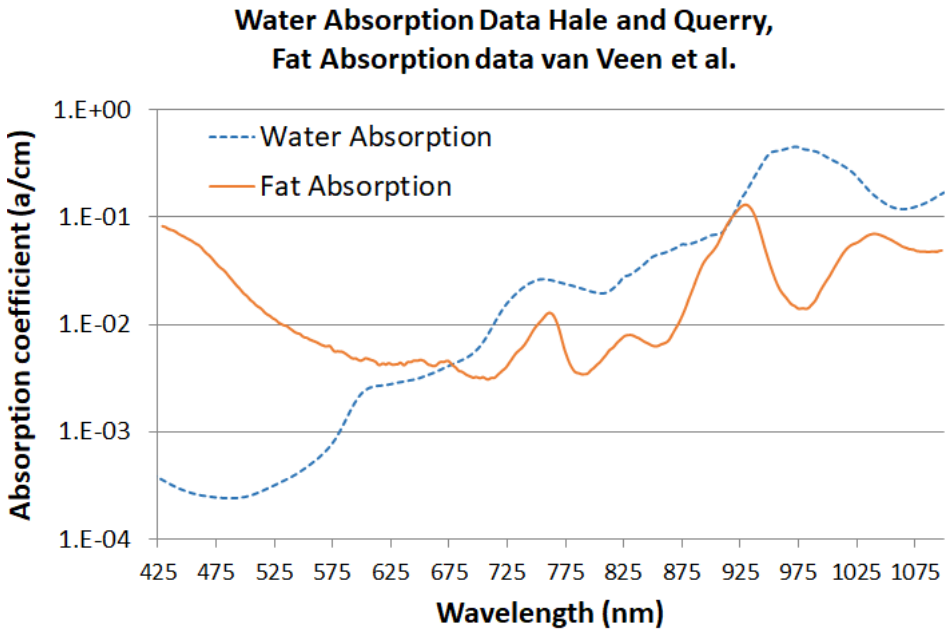

Figure 8 Plot of Relative Absorption (a cm^{-1}) coefficients from Hale and Quarry and van Veen et al showing the difference in absorption for water and fat across a broad spectral range. Note the inversion at approximately 975 nm between the two data sets.

Wang et al [75] imaged the lipid region with CARS in live spinal cord with forward and epi-collected signal. Spinal cords from guinea pigs were bisected sagittally and then a radial cut separated the white matter of the cord. The white matter strip was kept alive in oxygenated Krebs' solution in a transparent sample chamber located between an inverted excitation and upright forward collection lens in the microscope. Clear images of axons with good contrast were achieved by exciting at a wavenumber difference of 2850 cm^{-1} corresponding to the strong CH_2 symmetric stretch.

The forward and back-propagating signals both provided slightly different images of the sample. The forward propagating signal showed high signal strength of about an order of magnitude more than the back-propagating signal. The back-propagating signal showed finer detail of

internal structures within the myelin wall and a visible node of Ranvier, and appeared to have better resolution overall. It was unclear whether the improvement in detail in the back-propagating signal was due to true epi-CARS or whether the forward propagating signal was subjected to sufficient scatter to blur out any details before collection.

In addition to examining the difference between forward and backward signal, the authors also examined the polarization response of the white matter myelin. The polarization of the pump and Stokes beams was adjusted parallel and perpendicular to the myelin length, keeping pump and Stokes parallel with each other in both cases. The equatorial plane of the myelin was then brought into focus by stepping the system focus. When excitation polarization was parallel to the myelin length, the signal was several times stronger than the orthogonal case. The authors stated this was due to the symmetry axis of the CH_2 groups in the equatorial plane of the myelin. This was confirmed when imaging the top and bottom of the myelin cylinder which showed no directional preference.

The authors also measured the polarization response of the 3200 cm^{-1} H_2O symmetric stretch to probe the response from water molecules within the layers of the myelin sheath. While the effect was much less pronounced than the CH_2 2840 cm^{-1} vibration, because water is a weak Raman scatterer, a small difference was detectable. It was noted that for this water resonance the maximum signal was achieved with the excitation perpendicular to the myelin, opposite of the observed CH_2 signal. This implied that the symmetry axis of the ordered water is perpendicular to the CH_2 in the myelin. Only the water within the myelin region exhibited this polarization preference, with bulk water inside the axon or in outside solution showing an isotropic response.

3.3. Review of Multiple Sclerosis

As a quintessentially demyelinating disease, Multiple Sclerosis (MS) is an ideal candidate for investigation of myelin disorder. The exact mechanisms of the disease remain unknown; however axonal demyelination and subsequent degeneration is believed to be a primary driver of clinical symptoms. [126,127] Symptoms of MS typically follow a relapsing and remitting pattern, with cycles of degeneration and recovery of myelin. Clinical manifestations during an MS 'attack' can include weakness, sensory loss, optic neuritis (temporary visual impairment from inflammation of the optic nerve), double vision, vertigo, and impairment of coordinated movement such as gait, among others.[128] Relapsing-remitting MS patients recover to original function after an attack, while progressive forms of the disease result in continual increasing clinical impairment. Combinations are also possible, with the patient experiencing a time course of relapsing-remitting symptoms followed by a secondary progressive phase of continual deterioration.

These symptoms are accompanied by acute inflammatory demyelination in the CNS lasting at least a day. The demyelination is accompanied by immune cell infiltration, oligodendrocyte and axonal loss, and gliosis (formation of scar tissue within the lesion by glial cells). [129] The demyelinated lesions change over time and can grow, shrink or spread to other areas of the brain or spinal cord.[130]

In some lesions remyelination can occur, which is why some appear to shrink with time. In other lesions this does not occur, which may be due to a lack of mature oligodendrocytes in the lesion. Axonal damage can also inhibit remyelination, as the destruction of the axon leaves nothing to remyelinate. Demyelination often precedes axonal damage as the axon is unable to efficiently transmit action potentials without it. This taxes the metabolic processes of the axon and can lead

to excessive sodium levels as the axon struggles to maintain signal conduction. The excess sodium can lead to a rise in intra-axonal calcium levels as the mechanisms that maintain ion concentrations within the axon fail. Calcium in turn is involved in the activation of proteases and lipases which begin to disassemble the protein and lipid comprising the axon.

Externally, immune cells such as lymphocytes can also attack both the myelin and axon and are often found within lesions. These cells can generate reactive oxygen species (ROS) that chemically attack proteins and lipids. [7] Macrophages which have engulfed myelin debris are typically found in early cortical lesions. Both macrophages and T-lymphocytes emit a wide variety of cell signaling molecules collectively known as cytokines that interact with other inflammation-related processes. [131]

The interaction between inflammation and demyelination is still an open question. The leading theory posits that myelin damage is caused by immune cells and their products, such as ROS and cytokines. [132] The experimental autoimmune/allergic encephalomyelitis (EAE) animal model takes this approach by triggering an immune system attack on the nerves by injection of CNS proteins into the brain along with pertussis toxin to permeabilize the blood-brain barrier to allow the immune cells to infiltrate the brain. [133]

An alternative theory conjectures that oligodendrocyte damage and myelin damage occurs first, and the immune cell response is a subsequent response. [9] The cuprizone (CPZ) model explores this by attacking the oligodendrocytes via a copper deficiency mechanism. Mice are fed small doses of CPZ in their chow which chelates copper out of the diet. The resulting copper deficiency leads to oligodendrocyte death without appearing to impact other cell types. [134]

Recent work by Taraboletti et al confirmed uptake of CPZ into the oligodendrocyte itself. The presence of CPZ appeared to disrupt nicotinamide adenine dinucleotide (NAD+) metabolism

within the cell. [135] Myelinating oligodendrocytes perform aerobic glycolysis for energy, a process which requires NAD+ to function,[136] thus disruption of NAD+ would interfere with myelination.[137]

3.3.1. Animal Models

Two white matter injury models that recapitulate certain aspects of MS pathology, were selected to provide proof of principle samples for polarized CARS interrogation to investigate myelin disorder. The models were selected to provide a controllable level of demyelination in both fixed and live samples. The glutamate model induces damage on live nerves by activation of ionotropic receptors.[138] This leads to influx of calcium into the nerve and myelin that triggers processes causing structural failure of the myelin and axon. These details will be further explained and referenced in the next section.

The second model, for fixed samples, was cuprizone demyelination. Mice fed a diet containing cuprizone exhibit loss of oligodendrocytes, leading to demyelination of the corpus callosum region in the brain. The severity of demyelination depends on the concentration of cuprizone in the animal chow and the length of time of treatment. Explanation of this method is provided below.

3.3.1.1. Cuprizone

As discussed briefly in the MS review section, the cuprizone CPZ animal induces reproducible demyelination in mice.[139,140] The mechanism of demyelination in cuprizone was previously assumed to be due to copper deficiency [134] as it was believed that CPZ itself could not reach the brain and was confined to the gut.[141] Taraboletti et al evaluated direct cellular uptake of CPZ by

exposing populations of MO3.13 oligodendrocytes to a range of CPZ concentrations in vitro, ranging from 0.125 to 1 mM. After 24 hours of exposure only cells treated with the maximum concentration showed loss of viability, as measured with a live/dead cell assay. Further tests with concentrations of CPZ, copper, and copper-CPZ complex indicated an uptake of CPZ by the cells with diminishing concentrations observed in the cell culture medium. Conversely the concentrations of copper remained constant. In the cell, the CPZ was found to disrupt the metabolism of glycolysis by interfering with nicotinamide adenine dinucleotide (NAD+) in the cell, inhibiting a major energy pathway required for lipid synthesis. [142,143] The authors did not confirm the CPZ uptake in vivo, however, so there is still a question whether this mechanism applies for oligodendrocytes in the CNS.

A study by Hiremath et al [144] employed a low-dose CPZ treatment to demyelinate wild-type C57BL/6 mice. Hiremath observed that demyelination occurred with minimal systemic impact at CPZ doses of 0.2% or less, speaking to the specificity of the model. The authors tested various time courses for treatment, noting that glial fibrillary acidic protein (GFAP) antibody labeled cells increased above baseline after two weeks of treatment. Glial cell scar formation in lesions is prominent in MS, so the presence of these cells indicated injury response to demyelination. [145] This correlated with reduced luxol fast blue staining of myelin indicating significant demyelination in the third week of treatment. Demyelination continued steadily to week six where it reached a plateau.

Hiremath et al also experimented with increasing concentrations of CPZ treatment, ranging from 0.1 to 0.6% CPZ in the animal chow. At 0.3% and above some liver toxicity was observed, with increasing concentration causing progressively more systemic damage. The authors concluded that 0.2% was optimal for demyelinating while limiting spurious toxic effects.

Praet et al [146] conducted a review of the CPZ model examining the relevance to MS. The review also contained a detailed overview of the mechanisms of CPZ demyelination. Praet discussed the clinical repeatability of the 0.2% six week treatment regimen as put forth by Hiremath, and regarded the model's utility for studying both acute and chronic demyelination. Demyelination at different time points of 0.2% treatment was measured in the corpus callosum with T2 MRI and MBP staining to observe the myelin. Four weeks of 0.2% treatment was observed to cause extensive demyelination, although cessation of the CPZ treatment at that point allowed remyelination to begin, with increase in myelin visible in T2 MRI and MBP staining by six weeks.

Song et al [147] performed DTI [148] of specific regions of CPZ treated mice and noted a rise in relative anisotropy in the corpus callosum, indicative of demyelination. DTI measurements were correlated with luxol fast blue (LFB) staining of histological slices mapped by referencing structures in the brain. Interestingly, Song's results showed a significant increase in DTI relative anisotropy at three weeks with little change after that point.

Most studies, including the previous references, concentrated on demyelination within the brain.[149] However, Herder et al [150] compared the spinal cord to the corpus callosum in C57BL/6 mice. Transversal sections of corpus callosum and spinal cord (cervical and thoracic) were labeled with hematoxylin and eosin for the presence of immune cells and luxol fast blue staining for myelin. The authors found no observable demyelination in the spinal cord with this staining, whereas the corpus callosum exhibited clear demyelination as expected for the model. Interestingly, antibody staining for myelin basic protein mRNA in the spinal cord of CPZ animals was reduced compared to controls, implying that a subtle effect was still present in the spinal cord.

To test the ability of polarization resolved CARS to detect changes in myelin, two treatment protocols and two tissue types were selected:

A) 0.2% CPZ treatment for two weeks followed by immediate processing of the brain into coronal slices fixed with 4% paraformaldehyde (PFA).[151] The myelin in the corpus callosum is the region of interest as this is known to be demyelinated in the CPZ model.[152] This group should show reduced demyelination due to the short exposure to low dose CPZ. At this dosage and time point some oligodendrocyte cell death should have occurred but large scale demyelination is avoided. This would be confirmed by luxol fast blue staining of sections to visually confirm the presence of myelin.

B) 0.5% CPZ treatment for 25 days followed by processing into coronal slices with 4% PFA fixation. This group provided a positive control of extreme demyelination due to the high dose of CPZ and long treatment period. Spinal cord of the 0.5% treatment group would also be imaged to determine differences in myelination in what is thought to be a region relatively unaffected by CPZ. Treatment groups would be compared to control groups of naïve mice for corpus callosum and spinal cord samples. All mice were C57BL/6 type.

3.3.1.2. Glutamate

Glutamate is a natural neurotransmitter used in normal signaling between nerve cells.[153] The baseline concentration of glutamate in the synaptic cleft can be as high as 1 mM during neurotransmission, while in the CSF or extracellular fluid it is maintained in the range of 1-2 μM. [154]

Glutamate activates specific ionotropic receptors[155], which include N-methyl-D-aspartate (NMDA), α-amino-3-hydroxy-5-methyl-4-isoxazolepropionic acid (AMPA), and kainate. These

receptors are found in both CNS [156], and PNS axons. [157] and are primarily permeable to sodium and potassium ions, although NMDA and AMPA are also permeable to calcium. [156,158,159] Glutamate over-activation is believed to be a factor in lesion formation in MS white matter. [160] While the exact role that glutamate plays in MS is unknown, glutamate is released by macrophages and microglia [161] during inflammation, and it has been shown to damage oligodendrocytes and axons in the CNS.[162]

The goal of the glutamate excitotoxicity model [163] is to generate localized damage to in vivo or ex vivo samples. The presence of glutamate-sensitive NMDA receptors was identified by immunohistochemistry in the ensheathing myelin by Micu et al.[156] This was significant as it implied an independent primary response to glutamate within the myelin itself, rather than a secondary response initiated by the parent oligodendrocytes. Further evidence for the presence of NMDA receptors on the myelin was provided by immunoprecipitation of myelin fraction from whole optic nerve via sucrose gradient. Immunoblotting detected molecular subunits NR1, NR2, and NR3 of the NMDA receptor in the myelin fraction illustrating the likelihood of functional NMDA receptors on the myelin.[156]

Activation of the NMDA receptors leads to an influx of calcium into the myelin preceding axonal and myelin damage. Calcium sensitive enzymes including calpain-1 and phospholipase C could be contributing factors to the expressed damage as these are known to be present in CNS and PNS. [164-166] The influx of calcium directly into the myelin is significant because enzymes such as calpain and phospholipase C, known to be present in myelin, [167] become over-activated leading to degradation of major myelin proteins and lipids locally. [168]

Excessive intracellular calcium levels have also been linked mitochondrial dysfunction [160] leading to disruption of the energy production pathway similar to hypoxia. [169] Similar

mitochondrial damage was noted in human MS lesions by Fischer et al.[170] The authors also noted the presence of reactive oxygen species and oxidized phospholipids in cortical lesions.

Christensen et al [157] used 1 mM L-glutamate and 500μM glycine to induce damage in myelinated PNS dorsal root nerves via calcium influx. Glycine was applied in addition to glutamate as NMDA receptor activation requires both co-agonists. [171] The myelin was imaged with confocal microscopy using the lipophilic fluorescent probe Nile Red. [172,173] Christensen utilized two-dimensional Fourier analysis of the morphology of the myelin to assess structural irregularity due to the glutamate/glycine treatment. The analysis found that the morphology of the myelin moved towards a more chaotic spatial pattern as a result of the treatment. While examination of the Nile Red micrographs made the damage readily apparent, the two-dimensional Fourier analysis allowed quantification of the movement of the myelin from orderly parallel tracks to undulating or spherical damage patterns.

The directional preference of parallel myelin was examined by summing two dimensional Fourier transform of the myelin image through a line profile rotated 180 degrees. This generated a curve dependent on the anisotropy within the image. Highly ordered directional myelin would have a quick rise and fall during radial summation of the Fourier-transformed image. More damaged, disordered myelin tracts distributed signal intensity over a wider angle resulting in a broader curve. The change from ordered parallel myelin to disrupted morphologically convoluted myelin was quantified by taking the full-width half-maximum (FWHM) of the curve. A smaller value of the FWHM indicated a more ordered sample.

The Fourier transform analysis is very similar to the proposed polarization analysis for CARS. A key difference is that the Fourier imaging method requires morphological changes to create a difference in the Fourier-transformed image. Polarization-resolved CARS resolves a smaller

scale, deriving similar information for a single pixel that the Fourier method acquires for an entire image.

To test the similarity between the two models, PNS sciatic nerve will treated with glutamate, glycine to induce demyelination and axonal breakdown by activation of NMDA receptors. The activated NMDA receptors will allow calcium rise into the axon and myelin leading to destruction of the myelin via enzymatic activity.

3.4 MRI – CARS Comparison

A comparison of MRI and CARS helps to bridge the gap between clinical imaging for MS and laboratory studies of CNS injury. MRI performs on the macro scale many features that CARS provides on the micro scale, and there are functional similarities between both.

A parallel can be drawn between CARS imaging, spectroscopy, and polarization as compared to MRI imaging, T2 quantitative, and diffusion tensor imaging (DTI) methods. Spectroscopic and anisotropic methods both seek to provide additional information beyond structural imaging for each technique, and also strive to provide earlier indication of dysfunction prior to morphological changes.

MRI provides information on neurological disorders by imaging the fat and water content in the brain. MRI techniques can be used to image lipid, monitor water diffusion, and even detect the presence of water tightly bound to myelin. The sensitivity of MRI to CNS lesions makes it a highly useful diagnostic tool, particularly for monitoring the activity of lesions over time. Compared to pathological studies, which are typically performed via biopsies, or at autopsy, MRI is able to contribute to diagnosis of patients noninvasively. This positioned MRI to be the best non-invasive early indicator of MS and is considered the gold standard of diagnosis.[4]

Like MRI, CARS is also capable of imaging fat and water content of tissues. Both techniques use frequency-specific excitation (Larmor frequency in MRI, Raman vibration in CARS) to achieve chemically selective imaging. CARS addresses specific molecular bond energies through the excitation of the pump and Stokes. Different bonds and different vibrational modes of bonds are addressed by changing the frequency difference between pump and Stokes.

In comparison, MRI interacts with hydrogen proton spin with the excitation radio frequency dependent on the strength of the static magnetic field. Hydrogen is present in both fat and water, but the T1 and T2 relaxation times differ for each, with fat appearing bright in T1 images, while water appears bright on T2 weighted images. MRI selects between the two by altering the time between excitation pulses, with T1 images requiring short pulse sequences while T2 requires longer sequences.[43] CARS with sufficient bandwidth can likewise image either fat or water by exciting the appropriate Raman vibrations.

Quantitative T2 imaging is able to detect the compartmentalization of water within samples. Water more tightly associated with biomolecules, such as the myelin water, have very short T2 decay times compared to water in less constrained environments. As mentioned in chapter 1, Magnetization transfer (MT) imaging reduces this T2 time by exchanging saturated bound water protons for unsaturated free water protons, allowing for easier readout by measuring the reduction in the slower-decaying free water signal. The rate of MT provides information on the liquid environment.

The method presented in this work is also a measure of anisotropy, although for the proof-of-principle samples investigated, only lipid anisotropy is measured rather than water.

Spectroscopic CARS has been applied by others to investigate the effect of environment on the CARS spectral peaks characteristic of water. Zhu et al [174] applied a pump-probe pulse sequence

to reduce background by controlling the readout time of the Raman vibration relative to the initial arrival of the pump and Stokes.

DTI was highlighted for its sensitivity regarding the severity of tissue damage. The method worked by tracking the diffusion of water throughout brain tissue, which is inclined to travel parallel to a nerve fiber thus allowing the tracing of neuronal fiber bundles. The anisotropy of the water flow was indicative of the local organization of the tissue, and the authors noted the high correlation between DTI anisotropy indices and myelin content and axon count. [175]

Commowick et al [51] compared DTI MRI of control and MS patients, constructing a DTI atlas of control subjects. They compared this reference against individual MS patients searching for differences that might have been attributable to MS. The authors were able to detect significant differences between individual lesions and surrounding areas. The regions adjacent to lesions visible on conventional MRI exhibited significant differences in the DTI map, indicating an anisotropy change not visible conventionally.

The goal of this work is to detect anisotropy changes in the myelin by detecting the directional preference of lipids. Similarly to Commowick, the intention is to detect small anisotropy changes prior to morphology changes visible in imaging. Like DTI for MRI the metric is a directional preference within the sample.

While this section has discussed similarities between MRI and CARS, the two are not completely comparable. The scales they operate at are very different, with MRI addressing millimeter volumes and large areas, while CARS images micrometer scale images in areas under a mm (at least in microscopy applications of CARS.)

The greatest difference between CARS and MRI is the non-invasiveness of MRI. CARS is a microscopy technique with short working distance and poor penetration, so will likely never be

suitable as a routine diagnostic for humans. There may be a possible exception to this, however, as development of an endoscopic CARS probe has been put forward as a tool for surgical 'optical biopsy'.[176-178] It may be possible in the future that images and spectral, or even polarization data from a CARS probe may be used as a tool for MS.

4. CARS MICROSCOPE CONSTRUCTION

This chapter will describe the design and construction of a broadband tight-focus degenerate CARS system consisting of a dual optical parametric amplifier (OPA) excitation source and custom microscope. The OPA system was a modified ClarkMXR design driven by an Impulse (ClarkMXR, Dexter, MI) femtosecond amplified fiber laser. Beam conditioning optics modified the pulse width and polarization of the beams before being delivered to a custom-built laser scanning microscope frame. An overview image of the system is shown in Figure 9. The individual subsystems will be explained further below.

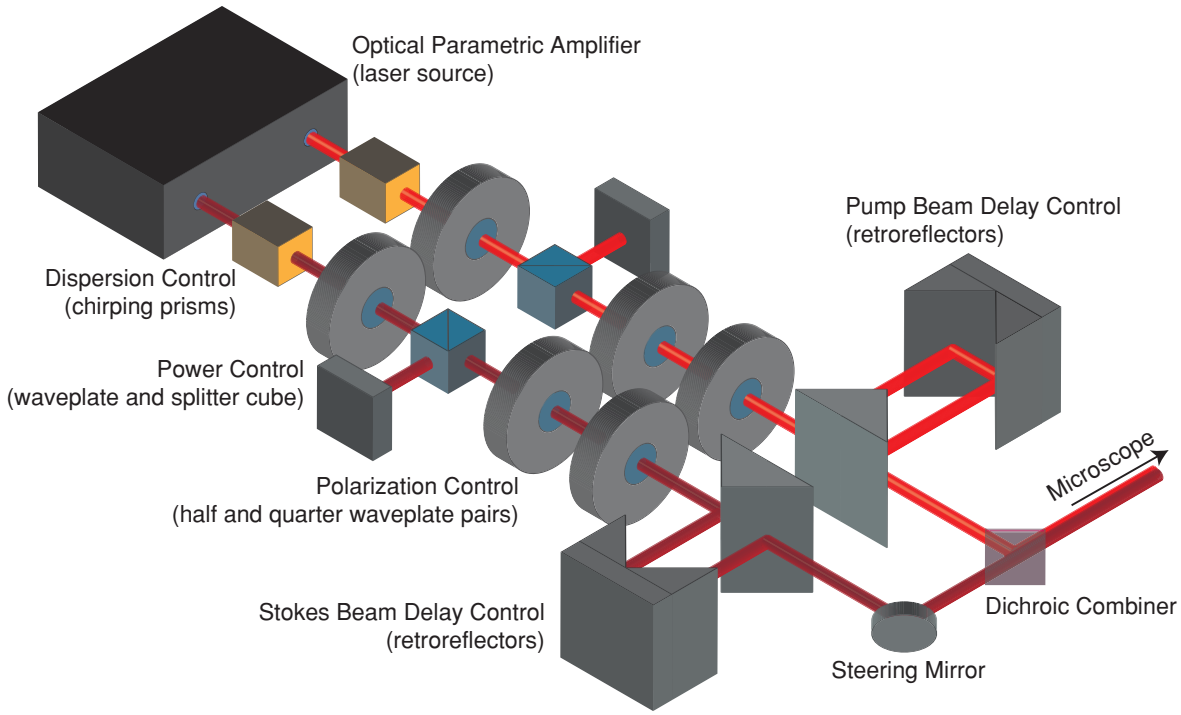

Figure 9 Beam conditioning system containing dispersion control, power and polarization control, and delay line systems for two separate beams. These subsystems will be described in detail later in the text.

4.1. Light Source

A broadband widely-tunable source was selected for maximum flexibility in CARS and multi-photon experiments. The Impulse fiber laser provided 100 fs pulses with 10 μJ of energy at a repetition rate of 1 MHz (average power of 10 W) and center wavelength of 1037 nm. This provided sufficient energy to simultaneously drive two OPAs, each of which could be tuned from 650-1300 nm. Driving both OPAs from the same laser provided perfect synchronization of the two outputs, which was ideal for providing the pump and Stokes wavelengths necessary for CARS.

4.1.1. Optical Parametric Amplification

Like CARS, optical parametric amplification is a non-linear optical process that creates an output wavelength determined by multiple inputs. OPAs utilize an intense pump beam at fixed frequency, which is combined with a seed wavelength at the desired output. Energy is transferred from the pump to the seed in a non-linear optical crystal. The ClarkMXR system was constructed as a non-colinear design, using the crossing of pump and seed to meet the necessary phase matching conditions within the crystal. The seed light was generated via a white-light continuum created in a bulk crystal plate by tightly focusing up to 1.5 W of 1037 nm light from the Impulse amplified fiber laser. Initially a titanium sapphire window was used for generating the continuum but it was frequently damaged during operation. A yttrium aluminum garnet (YAG) plate was selected as a replacement as it required less optical power to achieve a continuum and was found to be more durable in use.[179] As the YAG plate only required 0.7 W to operate an additional 0.8 W were freed up in the system for creating the pump beams. The seed light for each OPA was selected by a pair of monochromators with adjustable slits. This allowed the selection of not only

the center wavelength, but the bandwidth of the seed light provided to each OPA. The bandwidth of each OPA was adjustable from approximately 5 – 20 nm depending on center wavelength and stability.

The OPA pump beams used second harmonic generation (SHG) of the 1037 nm light from the Impulse via two barium borate (BBO) crystals. The focus of the pump light was placed beyond the crystals and the SHG process was driven at saturation to improve the stability of the pump generation.

The pump and seed for each OPA was directed via a periscope system to cross at an adjustable angle inside a BBO OPA crystal. The bandwidth of each OPA was limited either by the phase-matching requirements of the OPA crystal or the bandwidth of the seed. At shorter wavelengths the seed bandwidth dominated, while at longer wavelengths the crystal phase-matching requirements took precedence. The phase matching requirements were due to the angular cut of the crystals, which was a compromise to provide good phase matching across the 650-1300 nm range of each OPA.[180]

Each output of the OPA could operate at up to 200 mW, depending on the center frequency and bandwidth. At a repetition of 1 MHz, the pulses contained 1 nJ per mW of average power, providing approximately five times the energy to average power of a typical high repetition-rate titanium sapphire laser. Such a lower repetition rate source was deliberately selected because the peak energy allowed the OPA outputs to drive non-linear optical processes at reduced average power as compared to other higher repetition rate laser systems.[79] A photograph of the OPA system is shown in Figure 10.

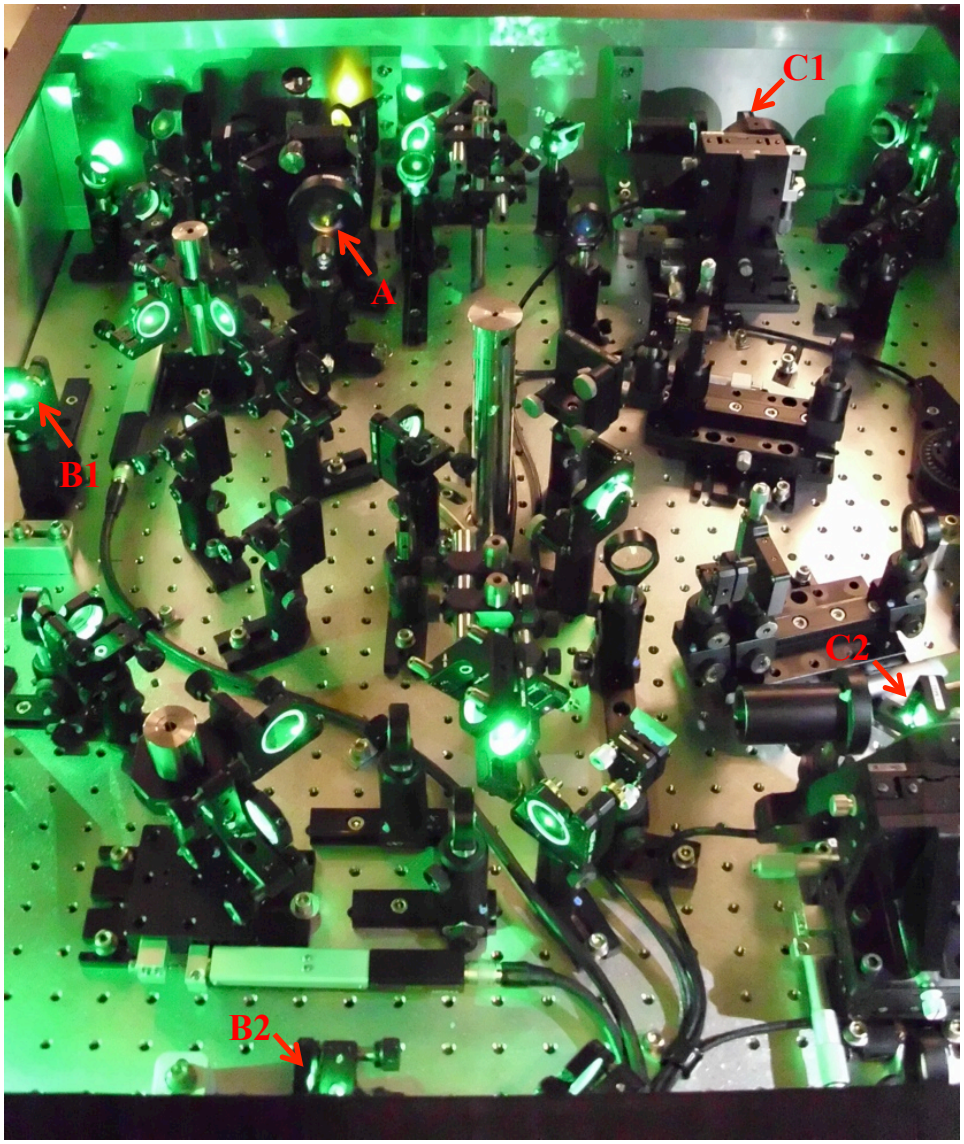

Figure 10 Twin optical parametric amplifier (OPA) system showing green pump light doubled from 1037 source. A) Yttrium aluminum garnet (YAG) continuum B1,2) Barium borate (BBO) harmonic generation crystals for OPA 1 and 2, respectively. C1,2) BBO OPA-cut crystals for each source.

4.1.2. Pulse Stretching

I designed and implemented a folded prism for adjustable positive frequency chirp with minimal angular sensitivity. The prism possessed features that address the limitations of a fixed glass dispersing optic, allowing adjustable dispersion while eliminating the angular sensitivity exhibited by other dispersing optical devices.

Preventing spatial chirp of a propagating beam requires that it enter and exit all glass surfaces at a normal angle of incidence. If all reflections are internal, where the incident and reflected rays remain inside the glass, any change in refractive index is avoided. No spatial chirp occurs, as the light does not experience any change in medium while being redirected. Total internal reflection (TIR) would seem sufficient for containing reflections, but the angle and polarization requirements, as well as its wavelength-sensitive nature make true TIR unsuitable. Instead, the placement of a metallic mirror coating on the surface of the glass provides a broadband, wavelength insensitive reflector to contain the beam within the glass while redirecting it.

Entry to the glass is maintained at a normal angle of incidence by grinding and polishing a shallow angle from one corner of the block. This entrance facet is anti-reflection (AR) coated across the NIR range for normal incidence. The exit is adjustable by means of a tilted exit ramp. The ramp allows the user to select the point at which the beam departs the block by raising or lowering the block assembly. This motion can be performed by a vertical opto-mechanical mount or laboratory jack. This adjustment requires only vertical translation of the block and does not impart any angular change to the beam, eliminating alignment issues when adjusting the number of reflections, and the therefore the amount of chirp. Rendered images and a photograph of one of the prisms is shown in Figure 11.

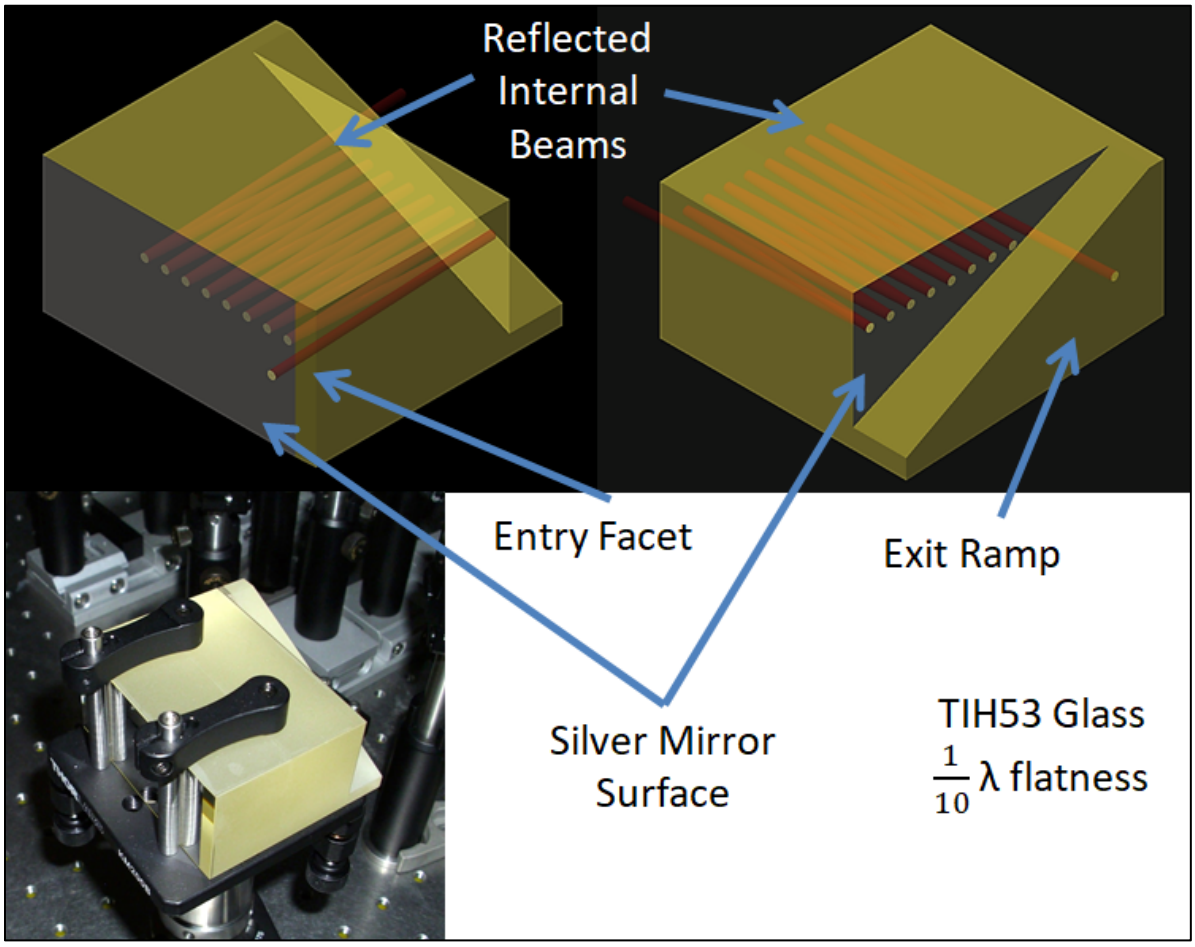

Figure 11 3-dimensional renders and photograph of custom folded prism for stretching laser pulses through positive dispersion. The folding design allows for over a meter of propagation through high index TIH53 glass. The path length is adjusted by raising or lowering the prism, which allows the exit ramp to pick off a particular reflection. Each bounce inside the block is 100 mm. Prisms were designed by the author and manufactured by BMV Optical (Ottawa, ON, Canada) TIH53 glass was purchased from Ohara Corporation (Somerville, NJ, USA)

The tilt of the exit ramp is proportional to the desired system beam diameter and the overall dimensions of the block. A steeper ramp permits a wider beam diameter but requires a taller block. The ramp divides the tilted mirrored surface from an AR coated normal exit face. Vertical adjustment selects the point within the block the circulating beam will transition from mirrored

surfaces to the AR coated exit face. The exit face is parallel to the entry facet, thus the beam enters and exits the block at normal incidence regardless of the overall path through the block. The normal entry and exit angles, as well as the achromatic internal metal coatings permit multiple passes through the block without inducing spatial chirp across the beam profile. The path length through the glass was adjusted by vertical translation of the block, which increases the number of bounces off the adjacent mirrored surfaces, and therefore the total path travelled within the block. An angled mirror coating covering half the exit surface of the block controlled whether the end of a given path through the block is permitted to exit the block or instead recirculate into the glass for additional chirp. The ramp geometry allowed the effective glass length to be varied from 150 mm to over a meter, while the block itself only occupied approximately 50 x 100 mm of space on the tabletop. The parallel angle entrance and exit faces also prevent angular deviation of the beam when adjusting the block for different path lengths.

TIH53 (Ohara Corporation, Somerville, NJ, USA) glass was selected for the prisms after consideration of a number of standard high-index glasses. When compared to glasses with similar refractive index, this material possessed good group velocity dispersion (GVD) to third order ratio for its index for the selected center wavelengths of the two OPAs, and had the highest transmittance at 963 nm of 0.999 cm^{-1}. The GVD of a glass decreases with increasing wavelength, requiring more glass to be used for a given dispersion. Longer wavelength beams will traverse more glass, making transmittance a priority to avoid excessive loss through the optic. While the NPH family of glasses has a higher ratio and index, they have a higher absorption at 963nm than TIH.

The third order dispersion (TOD) of the glass determines the majority of the non-linear chirp imparted by the glass. High values of TOD can lead to a variable dispersion rate over the

duration of the pulse, creating a variable interaction bandwidth over the duration of two pulses. It is therefore desirable to maximize GVD for maximum linear chirp while minimizing TOD to reduce non-linear phase changes. This can be quickly evaluated by calculating the GVD/TOD ratio of a given glass. The slightly lower TOD/GVD ratio of TIH53 as compared to NPH2 was deemed acceptable in return for superior transmission qualities at 963nm. Table 2 displays the various parameters for a collection of glasses for comparison. Values were calculated from glass data provided by Ohara Corporation (Branchburg, NJ, USA).

Table 2 GVD and TOD comparison for various glass types

	750nm					963nm				
Glass	Index	T*	GVD* (fs2)	TOD* (fs3)	Ratio	Index	T*	GVD* (fs2)	TOD* (fs3)	Ratio
TIH53	1.827	0.993	2429	1536	0.63	1.815	0.999	1642	1329	0.81
NPH2	1.897	0.994	3289	2231	0.68	1.88	0.996	2178	1827	0.84
SF11	1.768	0.995	2093	1290	0.62	1.757	0.998	1430	1124	0.79
SF10	1.714	0.993	1757	1064	0.61	1.705	0.995	1201	960.5	0.80
BSM25	1.651	0.996	859.2	488.6	0.57	1.645	0.996	577.2	543.8	0.94
BK7	1.512	0.998	495.8	308	0.62	1.508	0.999	303.9	403.3	1.33

*Transmittance (T), GVD, and TOD values are per cm of glass

Two blocks were manufactured, each of which was placed at the output of one of the OPA sources. The height of the block was adjusted to select the number of retro-reflections within the block to set the path length.

4.1.3. Polarization Controller

Control of the polarization state of pump and Stokes at the sample plane was required for orientation-specific excitation of CARS vibrations. The OPA outputs were already linearly polarized, however a control system was necessary to adjust the polarization angle and ellipticity to compensate for polarization distortions caused by the optics between the source and the sample.[181]

Numerous mirrors and dichroics were required to combine the pump and Stokes beams as well as collect return anti-Stokes signal from the sample. Interaction with any of these optics could alter the polarization state of the incident light prior to reaching the sample. [107,182] A system of motorized waveplates [183] was placed in the path of the pump and Stokes beams to pre-adjust the polarization state of the beams before encountering additional optics in the system. In this way, a compensatory perturbation was placed on each beam, which negated the influence of the intervening optics. A schematic of one of the two polarization controllers is shown in Figure 12. The required counter-polarization for compensation was determined by direct measurement of the polarization state of the excitation beams at the sample plane with a high-sample-rate liquid crystal polarimeter. (Meadowlark Optics LCPM-3000, Frederick, CO, USA) Combinations of manual and automated adjustments were made to a half and quarter waveplate in each controller to create the desired polarization state as recorded at the sample plane.

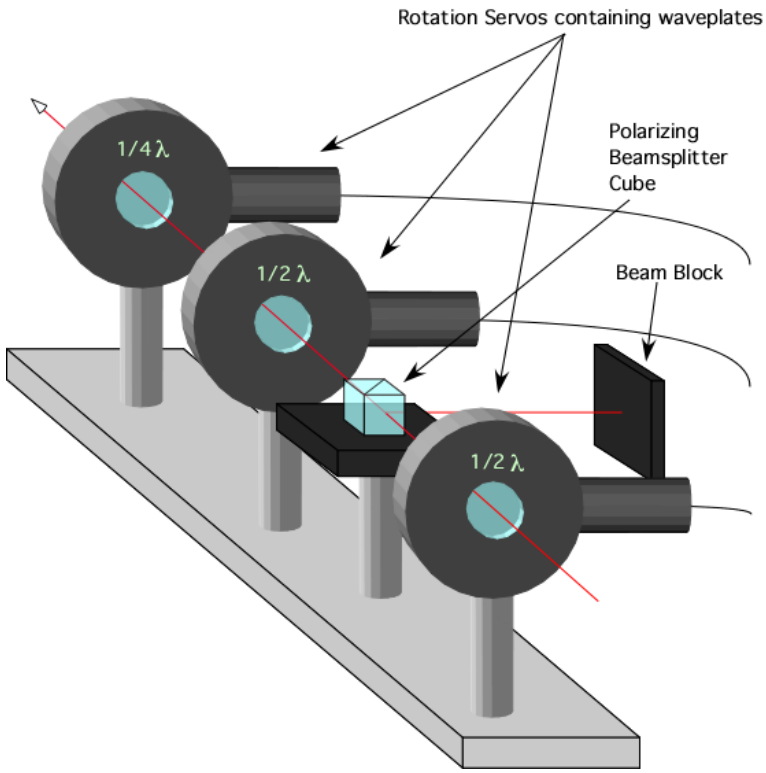

Figure 12 Laser polarization control system consisting of a 1/2 waveplate and polarizing splitter cube for power control, followed by 1/2 and 1/4 waveplate pair for polarization adjustment and precompensation.

The angles of the waveplates were recorded in a look-up table allowing any pre-calibrated state to be recalled via software. The polarization states were monitored at the start of every experiment and updated as necessary to maintain correct polarization output.

Polarization also influenced power transmission of pump and Stokes through the microscope. Angled optics created a slight transmission preference at various polarization angles. This was compensated similarly to the polarization by using a power controller to increase or decrease input power prior to the microscope. A calibration performed by a power meter (S170C, Thorlabs, Newton, NJ, USA) at each table entry ensured constant power at the sample plane for all included states.

The calibration and ongoing maintenance of the look-up table was performed by custom LabVIEW software (National Instruments Corporation, Austin, TX, USA). The software also synchronized positioning of the waveplates with image acquisition in addition to calibrating power and polarization. The software coordinated pump and Stokes polarization and power independently when acquiring multiple images, allowing the creation of 'polarization series' containing a different set of polarization states for each frame.

4.1.4. Beam Delay line and Combiner

The time delay between the arrival of the pump and Stokes pulses was controlled by an optical delay line in the path of the Stokes beam. The delay line consisted of a custom 2-dimensional hollow retro-reflector prism (BMV Optical) with a protected silver coating placed on a direct-drive linear servo motor (DDSM50, Thorlabs). The direct-drive linear motor permitted smooth motion of the retroreflector over 50 mm of travel with a minimum repeatable step size of 500 nm and absolute position accuracy of 1.5 μm. The retroreflector added up to 100 mm of path length to the Stokes pulses,. This equaled a maximum time delay of 333 ps and minimum time step of 3.34 fs with an absolute delay accuracy of 10 fs.

4.1.5. Laser Monitoring

A fiber-coupled spectrometer (Ocean Optics USB2000, Largo, FL, USA) was used for measurement of the pump and Stokes center wavelengths and bandwidths. Back-reflected light from the polarization controllers was directed to an aluminum target. An achromatic lens (ACN127-020-B, Thorlabs) focused the scattered light into the fiber optic connected to the spectrometer. Ocean Optics Spectraview software was used to display the collected spectra.

The power of the Impulse laser and OPA internal beams was measured with a 10 W thermopile sensor (S310C, Thorlabs) with an achromatic response. Measurements with this sensor were used to verify the proper functioning of the Impulse laser and OPA systems. A portable power meter console (PM100D, Thorlabs) was used to measure and record the readings from the thermopile.

The OPA outputs were measured with a 2 W thermopile (S302C, Thorlabs) to verify the average power before the scanhead. The thermopile was connected to a USB meter console (PM100USB, Thorlabs) that reported the power readings to the LabVIEW software operating the polarization controllers. Flip mirrors controlled by the software (8892, Newport/New Focus, Irvine, CA, USA) diverted the pump and Stokes beams as necessary to the thermopile for measurement. Power measurement at the objective was performed with a slide power sensor specifically designed for measurement of high NA light exiting microscope objectives. The sensor was designed in collaboration between Thorlabs Inc., Dr. Pina Colarusso (Live Cell Imaging Facility, University of Calgary), and the author. The device which is now offered commercially (S170C, Thorlabs) is water and oil-proof for use with water and oil immersion lenses. The sensor was placed underneath the objective lens with a drop of water between the sensor surface and the objective to match the normal operating conditions of the lens. The scan mirrors were parked in the central position and the power of the pump and Stokes beams exiting the objective were measured. The readings from this were used by the polarization control system to normalize the power of the pump and Stokes at the sample plane for various polarization states.

4.2.3. Stage and Sample Holder

Three high-load precision stepper motors were used for X-Y-Z motion of the stage (EAH504, EAH503, Thorlabs). Rather than moving the objective for focusing the Z stepper moved the sample relative to the focus of the lens. This alleviated the need for moving the objective lens and possibly affecting the scanning into the back aperture of the lens. The stepper motors were rated for 13 kg of load, which permitted the placement of extensive sample handling hardware on the stage without straining the motors. The minimum step size of the motor was 50 nm with 1 μm of bidirectional repeatability.

The scanning area of the microscope was a flat plane at the focus of the objective. A tilted sample would only partially intersect the plane. For large or long samples this would prevent the entire sample from being imaged in one field of view. To correct for any sample tilt the stage included a 2-axis goniometer platform (GNL20, Thorlabs) to allow tip-tilt adjustment to align with the imaging plane. A custom 3D-printed platform was attached to the top of the goniometer with anchor points for microscope slides or perfusion chambers for living samples. The perfusion chambers were also custom 3D-printed with baffles for minimizing vibration and movement of samples due to flowing fluid.[184]

4.2. Microscope Construction

The microscope was constructed from components attached to a vertical optical rail system. (XT66-500, Thorlabs) A Nikon C1 confocal scanhead (C1, Nikon) was [185] modified to bypass the confocal pinhole and directly allow the NIR beams onto the internal scanning mirrors. The scan lens integral to the scan head and an external 200 mm achromatic tube lens (AC508-200-B-ML, Thorlabs) were used to deliver the beams to the back aperture of an objective lens. (25x

1.1NA, Nikon) A custom 700 nm long pass dichroic (BMV Optical, Ottawa, ON) was placed between the objective and the tube lens to reflect the epi-collected signal towards the detection path.

The detection path consisted of a 725 nm short-pass barrier filter (Chroma Technology) to block any scatter from the excitation sources. A secondary longpass dichroic at 585 nm (Chroma Technology) split the collected light into a red channel for CARS and a blue/green channel for fluorescence, autofluorescence, second harmonic, or sum frequency generation imaging. Both channels featured a wide-band analog photomultiplier tube (PMT) (H10721-20, Hamamatsu) with extended spectral range for visible and NIR signal collection. The red channel used a 624/40 nm bandpass filter (Semrock) to collect CARS signal, while the blue/green channel was fitted with a 535/70 nm bandpass filter (Chroma Technology) for green or an optional 460/80 nm bandpass (Chroma Technology) for collection of blue light. The collection apertures of the PMTs were extended by placing 15mm 0.61 NA aspheric condenser lenses at the entrance of each tube to assist in the collection of high-angle light. (ACL1512U-A, Thorlabs)

Transimpedance amplifiers (Electrosolutions Inc., Holly Court, Flemington, NJ) converted the current output of the PMTs to a 0-2V output for the 12-bit analog-to-digital converters (ADC) in the scan controller for the Nikon C1 scanhead. The scan controller synchronized the acquisition to the movement of the scan mirrors, and rendered images in the EZC1 software suite. (EZC1, Nikon)

A spectrometer (USB2000, Ocean Optics) was placed opposite the PMT path that was accessible by rotating the primary dichroic 90-degrees. The spectrometer was used to verify the alignment of the pump and Stokes beams by measuring the spectrum of the CARS signal in a plastic sample with a parked beam.

4.3. Calibration

Consistency of CARS measurements was dependent on the pulse chirp and polarization of the pump and Stokes beams. Procedures for verifying consistent values for these parameters are described below.

4.3.1. Pulse width and Chirp Measurements

The pulse widths of pump and Stokes at the sample plane were measured using cross-correlation of both beams as per the method of Piazza et al.[186] In brief, the sum-frequency generation (SFG) and non-resonant CARS signal intensities were measured with respect to the relative time delay between the two pulses. As the delay line was swept the intensity of both signals was recorded relative to the delay position.

The sample was a 10 μm thick BBO crystal placed on the microscope stage under a protective cover glass. The thin crystal reduces the effect of the crystal itself on the resulting measurement by limiting the interaction length, and thus phase matching conditions, of the non-linear SFG and CARS processes. The crystal was cut for optimal SFG of 650-1000 nm for use with broad bandwidth laser sources.

The advantage of this method is that it utilizes the existing pump-Stokes delay line present in the system for performing the cross correlation, thus eliminating the need for external pulse-measurement equipment. The measurement is also performed at the sample plane of the microscope with the microscope objective lens in place. This takes into account all distortions of the scan optics and objective lens in the results, which would not be possible with a conventional pulse-width measurement technique such as auto-correlation. [187]

By noting that the SFG signal is dependent on the square of the combined pump and Stokes intensities, while the non-resonant CARS is dependent on twice the pump less the Stokes squared, the relationship between the pump and Stokes temporal width and the SFG and non-resonant CARS can be expressed as:

$\tau^2_{pump} = 2(W^2_{SFG} - W^2_{CARS})$

$\tau^2_{Stokes} = 2W^2_{CARS} - W^2_{SFG}$

Where $W_{SFG,CARS}$ = pulse width of the SFG and non-resonant CARS signal as measured by the delay line.[186]

The length of the pump and Stokes pulses could then be measured by comparing the interaction of two separate non-linear processes involving both. This method measured the temporal length of the pulses, but the chirp could only be estimated indirectly based on the assumption of linear dispersion. This assumption was based on the predominance of second order dispersion in the glass blocks as described in Section 4.1.2, and verified by the spacing of resonant Raman peaks as will be discussed in Section 5.

4.3.2. Polarization Calibration

Polarization calibration was performed by direct measurement of the polarization state at the sample plane using a polarimeter as described in section 4.1.3. These measurements were repeated at the start of each imaging session for the 13 linear polarization states that were used to verify that no drift occurred in the calibrated polarization profiles. The calibration for a given polarization state is updated if a deviation beyond 2 degrees in orientation or 0.05 elliptic was detected. These tolerance values were selected based on the observed repeatability of placement

of the polarimeter on the sample stage. Power normalization at each polarization state was verified as described in section 4.1.3., with the power measured at the objective for each of 13 linear polarization states. An automated power correction routine was performed prior to each imaging session. The LabVIEW software control system adjusts the power to the polarization controller at a fixed polarization state while measuring the power at the sample plane. A proportional control algorithm then adjusted the input power until a target value was reached. This control input was then saved to the overall polarization control table for use in that session. Screenshots of the stage and polarization control software are shown in Figure 13.

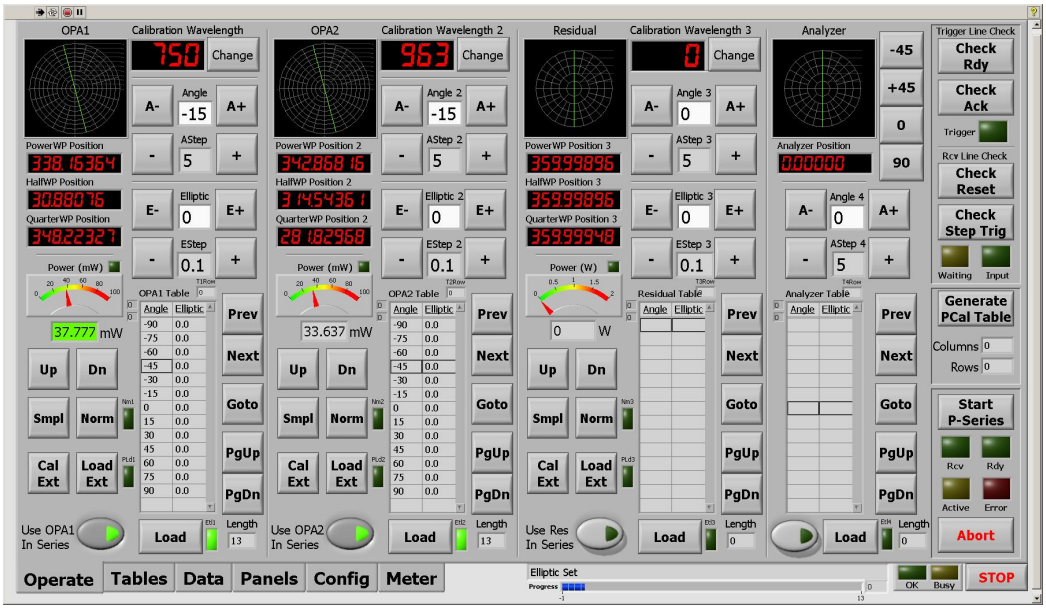

Figure 13 Polarization control software screenshot showing pump and Stokes polarization and power levels. Controls are provided for the user to select the pump and Stokes polarization and power, as well as start an automatic acquisition series synchronized with the microscope.

4.3.3. Test Samples

Verification of the span and linearity of the pump and Stokes pulse chirp was performed by examining the quality of a CARS reference spectrum acquired for a set of three types of plastic beads. The Raman spectrum for each plastic was acquired from the literature[188,189] to determine the position of the major peaks for each plastic. The three chosen plastics were polymethyl methacrylate (PMMA), polystyrene (PS) and polyethylene (PE). These Raman peaks of this combination of plastics span the 2800 to 3100 cm^{-1} vibrational range, providing convenient reference points for comparison with CARS spectra of the lipid region. The Raman spectra of the three plastics are shown in Figure 14.

All three plastics exhibit peaks at the CH_2 symmetric stretch around 2850 cm^{-1} while PE also provides a strong asymmetric stretch at 2880 cm^{-1}. PMMA contains a symmetric CH_3 stretch at 2930 cm^{-1} while PS provides additional peaks at 2900 and 3050 cm^{-1} related to CH_2 in chains (aliphatic) and rings (aromatic).

The overall span and peak structure of the three plastics provides a way to calibrate the span of the delay line in wavenumbers, establishing a delay line position for a given Raman peak. The width of the peaks also provided a confirmation that the spectral sensitivity of the system was equal or better than required to clearly resolve single peaks. The spacing of the peak confirmed the linear chirp of the pump and Stokes pulses. If the spacing between the peaks matched the Raman spectrum then the instantaneous frequency difference between the pulses were linear over the range of the spectral readout.

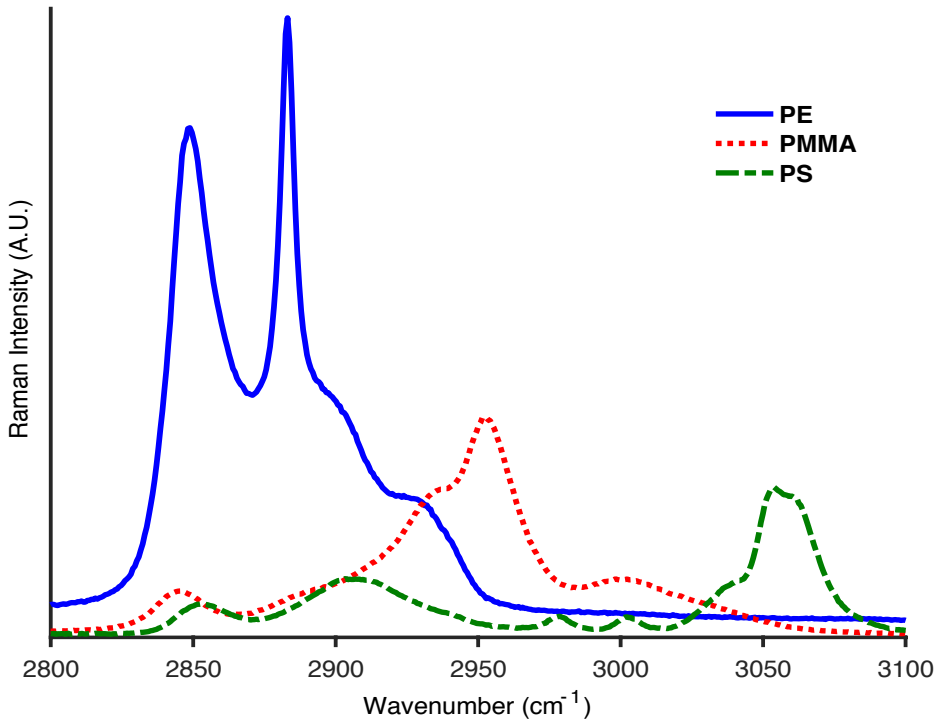

Figure 14. Spontaneous Raman spectra of polymethyl methacrylate (PMMA), polystyrene (PS) and polyethylene (PE) plastics.[188]

The polarization response of the detection path was measured with and without a rotating analyzer using samples of liquid oils. Olive, grapeseed, and coconut oil samples were imaged to provide a homogeneous CARS signal at any excitation angle. The analyzer was rotated with the pump and Stokes polarization over 180 degrees, then the experiment was repeated without the analyzer. The CARS signal at every 15 degrees was measured over the 180 degree span to determine any variability in the signal reaching the detector.

4.4. Construction Summary

This chapter detailed the design and construction of the elements of the polarized-CARS microscope. The choice of optical parametric amplifiers as the pump and Stokes sources was

explained, and the modification of the continuum source in the OPA was described. The engineering of custom the folded dispersion prisms was explained, detailing glass selection and geometry. Optomechanics for the polarization controller, delay line, and microscope stage were described, with special note taken of the time step and repeatability of the delay line motion.

It is worth noting that the complexity of the system was so great that new devices, such as the folding dispersion prisms, automated polarization controllers, and water-proof microscope objective power meter had to be designed from scratch for its construction and operation.

The next section will discuss the results of the testing, calibration, and proof-of-principle myelin samples that were imaged by this microscope.

5. RESULTS

Samples were imaged for calibrating the basic parameters of the system, including pulse width, polarization response, and Raman spectral resolution. Proof-of-principle samples followed, first to confirm the imaging performance of the system, then to explore the polarization response of myelin. First I describe the calibration samples, which were required for maintaining consistent bandwidth and determining the position of the delay line relative to the CH_2 symmetric vibration.

5.1. Calibration Samples

Test samples including a non-linear crystal, liquid oil samples, and plastic beads were imaged to verify the basic functionality of the CARS microscope system. The non-linear crystal measured the pulse width of the pump and Stokes, the oil samples characterized the polarization response of the detection path, and the plastic beads confirmed the spectral resolution of the system and the linearity of the pulse chirp.

5.1.1. BBO Crystal Pulse Width Measurement

The time-delay dependent pulse width of the sum-frequency generation (SFG) and CARS signals generated by the pump and Stokes was measured in thin BBO crystal. The data was fit to a Gaussian curve using a least-squares fit, and the FWHM was determined for both signals. The data and curve fits are shown in Figure 15.

The power of the Stokes beam was reduced to 1.6 mW and the pump set to 10 mW to prevent depletion of the pump beam by the Stokes. The bandwidth of the pump was 16.9 nm and the Stokes was 11.5 nm, set by adjusting the OPA seed bandwidth for each. The FWHM of the

CARS signal was 5.58 ps and the SFG was 7.42 ps. The resulting pump and Stokes pulse widths were calculated to be 6.91 and 2.70 ps, respectively, using the method described in section 4.3.1. In brief, the SFG signal depends on the square of the combined pump and Stokes fields while the CARS signal is dependent on twice the pump less the Stokes squared. The SFG and CARS signals have different delay-dependent intensities, and this difference can be used to back-calculate the pump and Stokes pulse widths from the SFG and CARS interaction lengths as measured by the delay line.

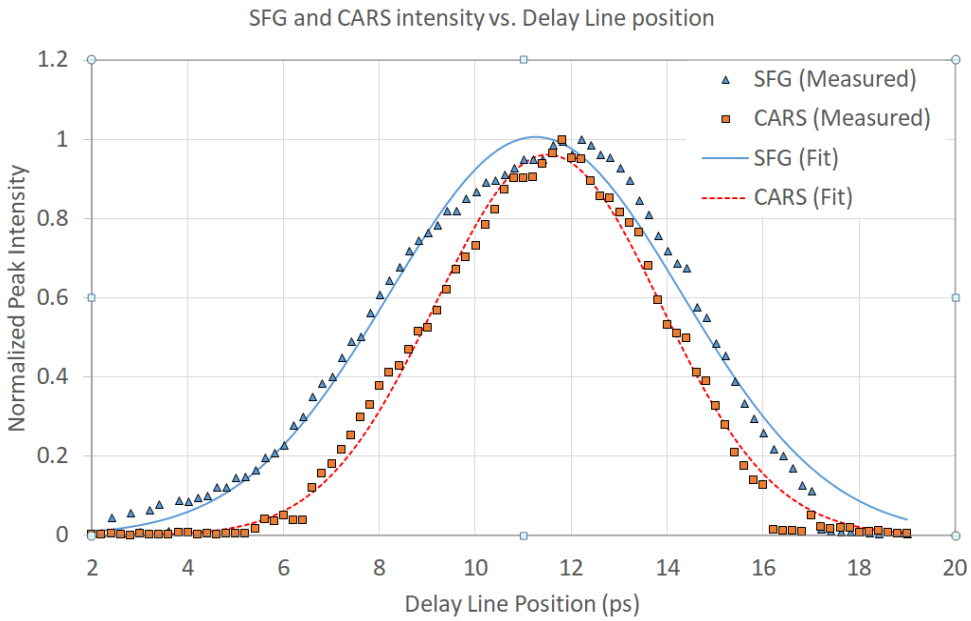

Figure 15 The measured intensity of SFG and CARS signals generated in a thin BBO crystal relative to the delay line position between the pump and Stokes beams. These values can be used to back-calculate the pulse width of the pump and Stokes pulses as explained in the text.

Calculation of the group delay dispersion (GDD) of the glass chirping blocks described in section 4.1.2. estimated pulse widths of 6.06 ps for the pump and 2.43 ps for the Stokes after transiting the blocks. The longer pulse width measured with the BBO crystal was likely due to the dispersion introduced by the other optical elements in the microscope, such as the objective, scan and tube lenses, which all contain substantial amounts of glass. GDD values for typical microscope objectives range from 1000 – 4000 fs^2 [190] which is approximately one sixth of the dispersion induced by one trip of the pump and Stokes inside the chirping blocks. (10 cm of glass per trip gives ~24300 fs^2 for the pump) This also does not account for the large scan which contained more glass than the objective, as well as all the other optics used to deliver the beam to the microscope. Measuring the pulse width directly after the glass blocks was impossible as the measurement method required tight focus, necessitating an objective lens, as well as the delay line system located much further down the optical path. It is impossible to perform the measurement without these additional optical elements which would add to the GDD and increase the measured pulse width. [72]

5.1.2. Oil Spectra and Polarization Responses

Coconut, grapeseed, and olive oil samples were selected for testing as these oils contain CH_2 and CH_3 symmetric and asymmetric vibrations [191] also present in myelin. The liquid oils provide a completely disordered sample with a similar vibrational profile to lipid within the 2850 to 2930 cm^{-1} wavenumber range. CH_2 is constrained within the acyl chains of the long fatty acids while CH_3 is likely to be found at the end of the chains or in ring structures where any directional

preference relative to the molecule should be diminished. All three oil samples were spectrally imaged to determine the 2850 and 2930 cm^{-1} responses of each.

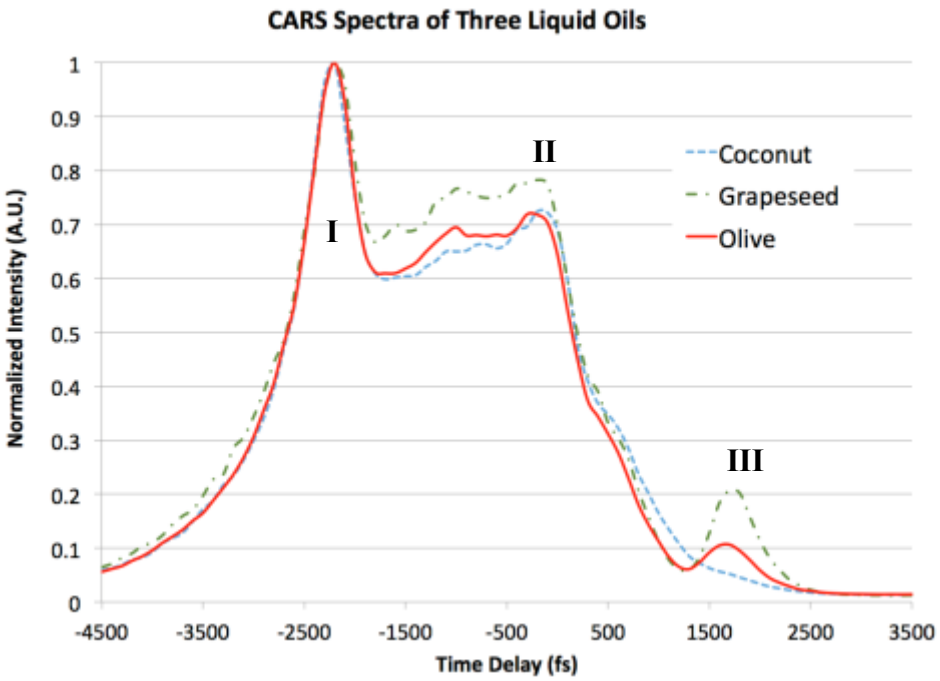

Figure 16 CARS spectrum of three oil samples. The peak at -2400 fs corresponds to the 2850 cm^{-1} CH_2 stretch, while the peak at -200 fs corresponds to 2930 cm^{-1} CH_3 stretch as calibrated in section 5.1.3.

The CARS spectra of the three oils are shown in Figure 16. The peak corresponding to 2850 cm^{-1} is indicated by 'I' and 2930 cm^{-1} peak by 'II'. A double bond =C-H stretch at 3015 cm^{-1} is indicated by 'III' and corresponds with published spectra showing the absince of this vibration in coconut oil. Grapeseed was found to have the closest intensity match between the CH_2 and CH_3 resonances and was selected to act as a polarization standard.The CARS signal intensity of grapeseed oil was measured for 2850 and 2930 cm^{-1} as the polarization of the pump and Stokes

were rotated. This measurement was performed twice, once with an analyzer in front of the detector and a second time with no analyzer. Two sets of measurements were taken: one with the analyzer in the detection path, rotated in synchronization with the pump and Stokes angles, the second with pump and Stokes angles rotated together but with no analyzer present. The results are shown in Figure 17.

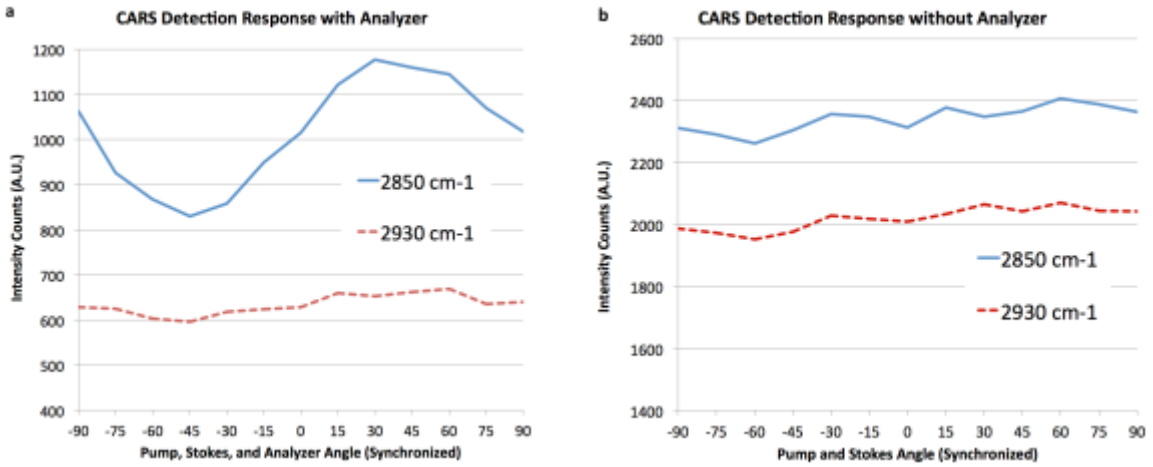

Figure 17 Polarization response of the detection path for two specific Raman vibrations in grapeseed oil. a) Polarization response with a rotating analyzer aligned with pump and Stokes polarization rotation angle. The CH_2 vibration at 2850 cm^{-1} shows a response to the analyzer rotation while the 2930 cm^{-1} CH_3 polarization sensitivity is almost completely muted b) Measurement repeated with the analyzer removed from the detection path.

The CARS signal for the 2850 cm^{-1} vibration shows a minimum and maximum at positive and negative 45 degrees relative to the polarization axis. Conversely, the values at 0 and 90 are very similar and are midway between the minimum and maximum values. This result implies that the CARS signal from the 2850 cm^{-1} vibration was polarized, and that the primary dichroic in the microscope was inducing an elliptical polarization onto the signal when it reflected the light towards the detector. [192] The effect of the dichroic on the pump and Stokes polarization was compensated by the polarization control system to maintain a linear state. The detection path did

not benefit from this system so the detected light contained polarization distortions. The elliptic nature of the light can be inferred from the minimum and maximum points in Figure 17a. If the light were still linearly polarized and aligned perfectly with the analyzer then the signal would be constant across angle. If the light was perfectly circularized it would be similarly constant.[182] The signal at the 2930 cm^{-1} vibration showed very minor polarization preference (10% signal intensity change) compared to the 2850 cm^{-1} vibration (30% change). Following the same logic for the 2850 cm^{-1} signal, the 2930 cm^{-1} must be mostly circular in nature to maintain a constant signal through the rotating analyzer. The alternative case of perfectly tracking linear signal seems unlikely given the polarization change shown by the 2850 cm^{-1}. The CARS signal only shifts by a few nanometers when it is tuned, so a chromatic dependent difference seems unlikely. The only alternative is circular polarization, although there is a very small minimum and maximum corresponding to the same angles in the 2850 cm^{-1} response. This indicates that the 2930 cm^{-1} was nearly circular rather than mostly, so some residual linear polarization could still be present. Removal of the analyzer equalized the signal for both vibrations across all pump and Stokes angles to a difference of 2.5%. The consistent angular response of both signals indicated that the detection path was polarization-insensitive without the analyzer. The detector, a photomultiplier tube (PMT), did not show a polarization dependent signal. PMTs are known to be insensitive to polarization if the incident light arrives at the detector at normal incidence. If the PMT is tilted significant dependence is observable. [193] The light in the detection path of this system was collimated and aligned directly down the detection path ensuring that the signal did arrive at the PMT at normal incidence.

5.1.3. Plastic Reference Beads

Polymethyl methacrylate (PMMA), polystyrene (PS) and polyethylene (PE) beads were mounted in Sylgard 184 (Dow Corning, Midland, MI, USA) to prevent movement. The delay between pump and Stokes was manually adjusted while imaging the beads to determine the position of the leftmost PE peak and the rightmost PS peak relative to the delay line position. Images were sequentially acquired, as the delay line was automatically stepped over 7 ps of path length in steps of 70 or 140 fs while triggering automated acquisition of the images depending on the desired spectral resolution.

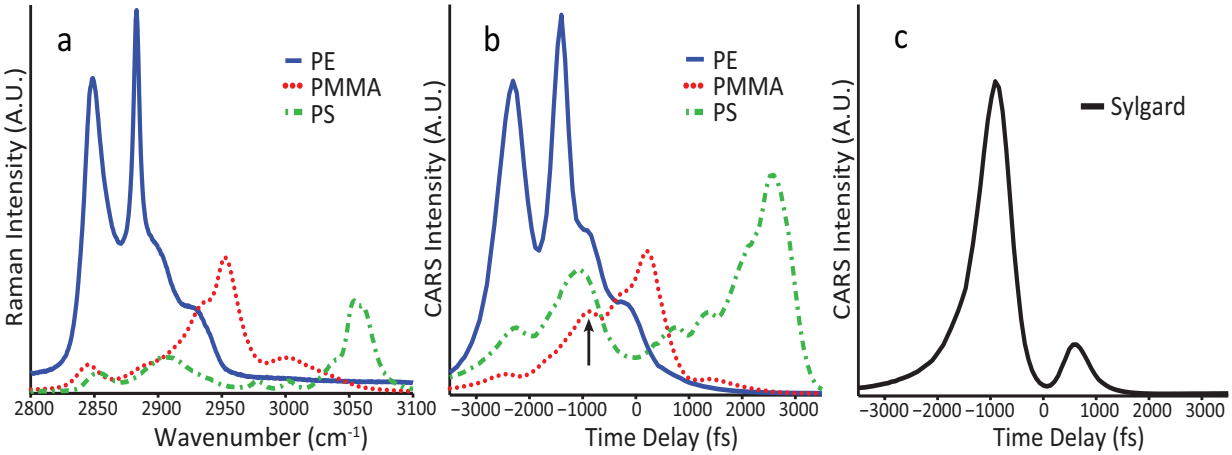

Figure 18 (a) Spontaneous Raman spectra of PE, PMMA, and PS plastics. (b) CARS spectrum obtained for the same three plastics using our CARS microscope. The arrow at -900 fs indicates the extraneous peak introduced by the Sylgard mounting medium. (c) CARS spectrum of the Sylgard mounting medium for comparison. The CARS spectrum in 'b' shows good agreement with the published spontaneous Raman spectrum shown in 'a'.

The acquired CARS spectra of each plastic was compared to published spontaneous Raman spectra. (Figure 18a) The acquired CARS spectrum (Figure 18b) shows the results of a 70 fs resolution scan of the three plastics, with 450 mm of glass introduced in the pump path and 650 mm of glass in the Stokes paths, via the dispersion prisms described in chapter 4. The pump was

centered at 750 nm with a full-width half-maximum (FWHM) bandwidth of 14 nm, while the Stokes was centered at 963 nm with a bandwidth of 10 nm. This corresponded to a spectral range of 2770 to 3130 cm-1 for the chirp and bandwidth parameters of the pump and Stokes. Based on the physical step size of the stage and comparing to the full span between the peaks the 70 fs step size equated to a vibrational step of approximately 3 cm-1. A small peak not corresponding to any of the plastics was visible at -900 fs (approximately 2930 cm-1) corresponding to the Sylgard mounting media. The acquired CARS spectrum of Sylgard is shown in Figure 18c, with one major peak at 2930 cm^{-1} and one minor peak near 2950 cm^{-1}. The minor Sylgard peak is the cause of the slight extension of the PMMA 2950 cm^{-1} peak visible in Figure 18b.

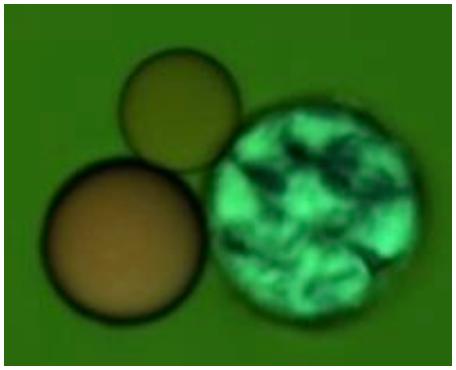

Figure 19 False-color CARS image of three plastic beads captured from 2800 to 3100 cm^{-1} with the resulting CARS spectrum converted into a pseudocolor image. The largest bead, PE is 20 µm in diameter. The medium-sized bead is PS with a diameter of 16 µm, while the smallest bead, PMMA, is 11 µm in diameter. The background is Sylgard 184.

The results of the CARS spectra were in close agreement with the published spontaneous Raman spectra for all three plastics. The spacing of the CARS peaks with respect to the delay line position also confirms the linear chirp on the pump and Stokes beam. A non-linear chirp profile

would distort the relationship between wavenumber and delay line position and the peaks would appear closer together or further apart compared to the spontaneous Raman spectrum.

For visual interpretation, the CARS spectra for each plastic were mapped into a visible-equivalent spectral image, treating the Raman spectrum as if it were a visible light spectrum. This displayed the Raman vibrational content of each plastic in a combination of hues. An image of the three plastics is shown in Figure 19. The small PMMA bead with content mainly in the middle of the scan range maps predominantly to green, while the large PE bead, with smaller wavenumber content maps to blue green and appears brighter. The medium PS bead contains information at both longer and shorter wavenumbers over the scan range and thus appears orange, as a mixture of red and green mapped components.

5.1.4. Imaging Tests

Paraformaldehyde-fixed spinal column of C57BL/6 mouse in 150 μm section was slide mounted and imaged to verify the imaging performance of the microscope on myelinated tissue. A dorsal-root entry zone (DREZ) was located in the sample and 13 images were acquired at 15 degree increments from -90 to +90 degrees generating a polarization image series. The DREZ is the intersection of peripheral nerves with the CNS of the spinal cord. The peripheral nerves often intersect the cord at a steep angle, providing two straight sections of myelin at different orientations. The polarization series of this intersection will show different intensities for each section as the excitation aligns with them in turn during the polarization image series.

Four images from that series are displayed in Figure 20, showing myelin, in green. Note that this is an intensity signal rather than a spectral pseudo-color image like the beads displayed in Figure 19. The signal is obtained from the 2850 cm^{-1} symmetric stretch. The CNS myelin is arranged

vertically while the PNS myelin is oriented approximately 45 degrees from the CNS. The double arrows indicate the direction of the excitation in each image. The triangles indicate small features in the myelin that were pronounced when the polarization angle was off the main axis of myelin. The triangles in the top left image show an inclusion of folded myelin and two nodes in the PNS. The myelin in the nodes curves inwards and the sections of myelin in the node aligned with the vertical excitation are brightest.

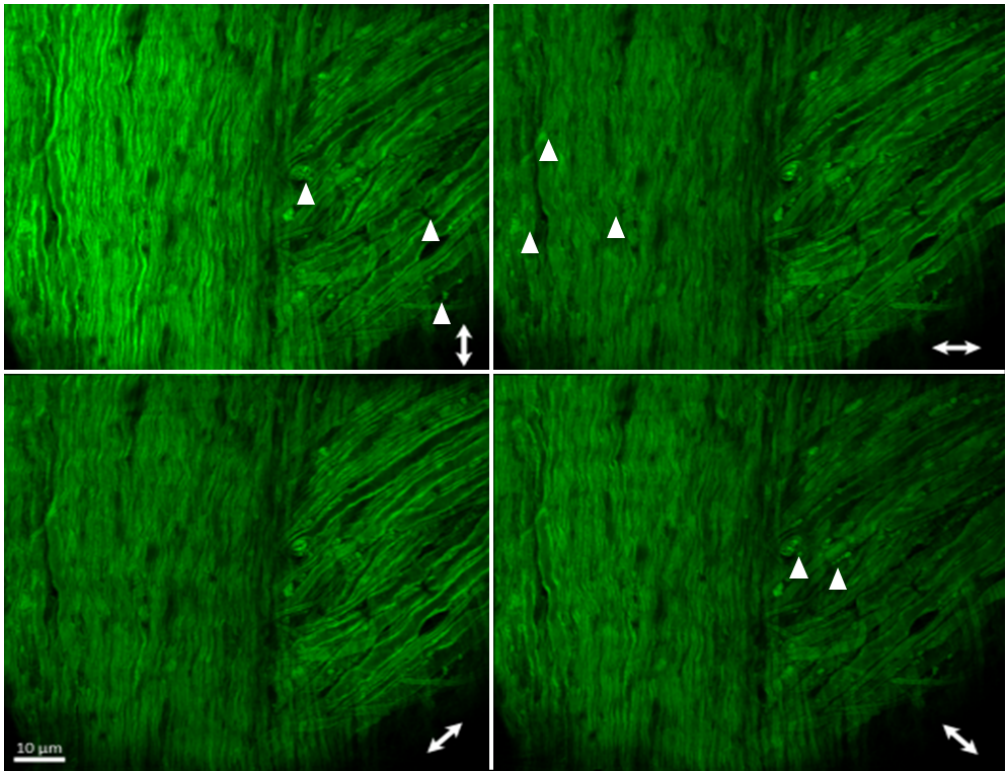

Figure 20 CARS image of a spinal cord section from an 8-week-old C57BL/6 mouse at four polarization states for the 2850 cm^{-1} vibrational line. Both pump and Stokes beam polarization angles were aligned in the direction of the double arrows. The myelin running north-south in the image is CNS tissue and has the highest CARS signal intensity with vertical polarization, as shown in the top left image. The PNS myelin is oriented at 45 degrees to the CNS, and is brightest in the lower left image. The small triangles point to lipid debris and nodes that are highlighted when the polarization is not aligned with the lengths of myelin.

In the top right image the triangles point to small bright deposits in the CNS axons that appear to be myelin debris. Similar debris deposits are indicated in the bottom right image in the PNS. The myelin tracts are brightest when the polarization of the excitation is in parallel with the tract. For the CNS section this occurs in the top left image with vertical polarization, while for the PNS this occurs in the bottom left image with the excitation at 45 degrees. This result shows the polarization dependence of the 2850 cm^{-1} vibration and verifies that the Raman dipole for this vibration aligns parallel to the myelin as expected. The debris in the image are visible at all polarization states illustrating the reduced directional preference of the 2850 cm^{-1} vibration when not ordered in the myelin.

5.2 Data Analysis

The 13 polarization images acquired from -90 to +90 degrees created a polarization-resolved 'stack' of images. Each pixel contained 13 intensity readings corresponding to the 15 degree steps from image to image. The images were intensity-threshold filtered to eliminate pixels with signal below 25% of the maximum to eliminate background signal from out-of-plane myelin. The minimum value of the 13 polarization readings was applied against the exclusion threshold to determine if a pixel would be retained or discarded.

5.2.1. Anisotropy Plots

A plot of the intensity recorded from a single pixel from the CNS in a spinal cord sample in Figure 20 is shown in Figure 21. The pixel was located in a portion of myelin running due north-south through the image. It is shown here as an example of the type of data acquired for each pixel in the image. In the plot, 0 degrees references 'North' in the corresponding image,+90 is

'West' and -90 degrees is 'East'. The plot therefore shows the CARS signal response to the excitation polarization being rotated counter-clockwise through 180 degrees.

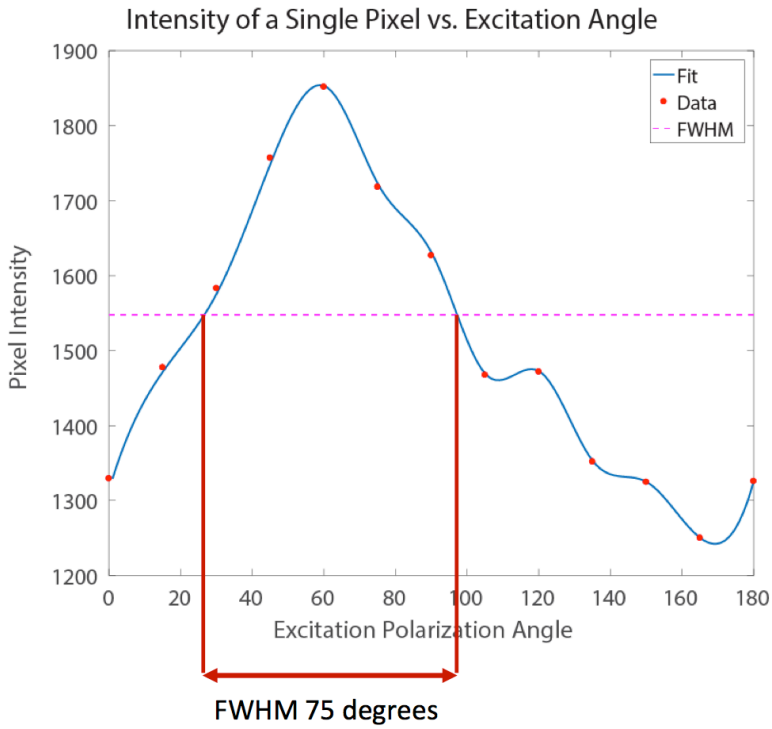

Figure 21 Intensity recorded from a single pixel with respect to polarization angle taken from the spinal cord sample used in the previous figure. The spread of intensity by angle is indicative of the population of angles of CARS vibrations present in the pixel. A wider FWHM indicates a broader distribution of dipole angles while a narrower one indicates that the dipoles are more tightly aligned with each other.

The spread of angles within the pixel can be measured by calculating the FWHM of the curve. The signal is an ensemble of all the CARS emitters within the pixel, which may all be oriented differently. A broader FWHM implies a higher level of disorder in the pixel by indicating a greater spread of angles within the population of emitters. The FWHM value assigns a single number to represent the degree of disorder of all oscillators within the pixel volume. This value can be color-coded and plotted, generating an anisotropy image of the sample. Two examples of

this in control spinal cord are shown in Figure 22. Violet-shifted pixels are disordered, while red is ordered. Blue-green is intermediate. The numbers indicated on the color bar are the FWHM values in degrees corresponding to each color. The right image, further caudal in the cord, shows more color variety than the higher, or more rostral sample.

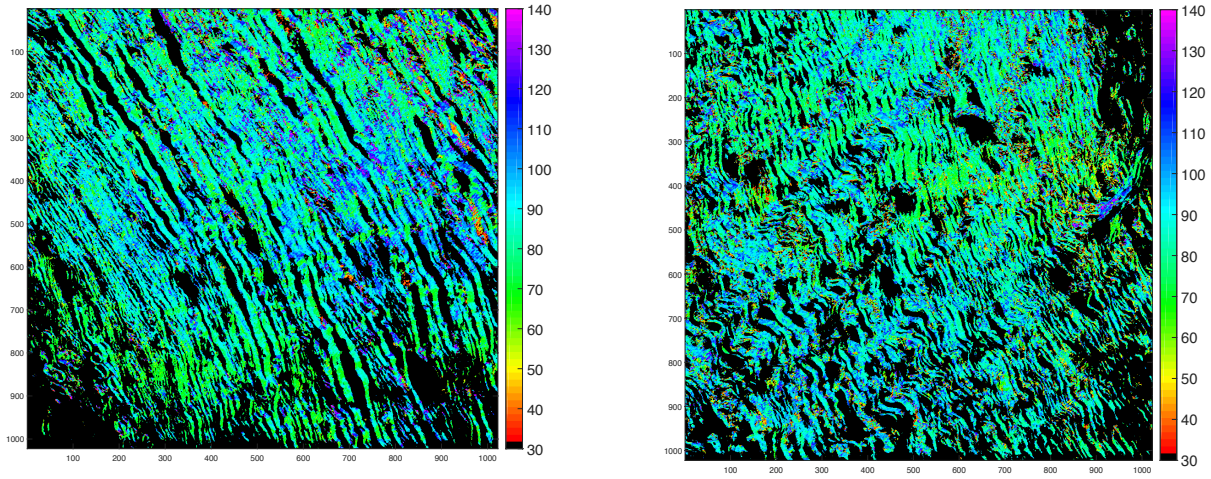

Figure 22 Color-coded plot of anisotropy for two fields of view within cervical region of a control spine. Images were 1mm apart down the length of the cord, with the left image more rostral.

5.2.2. Histogram and Cumulative Histogram Analysis

Imaging is useful for providing regional information, but it is useful to be able to perform statistics on an entire image. One method of quantifying a picture is through a histogram, which is a plot of the population in the image, binning pixels of similar values together. The histograms corresponding to the images in Figure 22 are shown below in Figure 23.

The histogram is composed of all the FWHM values (a single pixel of which was shown in Figure 21) of the anisotropy plots of all the pixels within the image. An image-wide increase in order or disorder results in a shift in the histogram as the average value changes. Regional

differences within an entire image can also invoke a broadening of the histogram rather than a shifting, by increasing the population of pixels with higher and lower values compared to the mean. Inspection of numerous histograms from imaged myelin samples identified a small population of highly ordered pixels appearing concurrently with a shifting of the bulk of the histogram towards the more disordered state. This caused little change in the mean value of the histogram as the addition of the few highly ordered pixels negated the slight shift of the bulk of the distribution towards disorder.

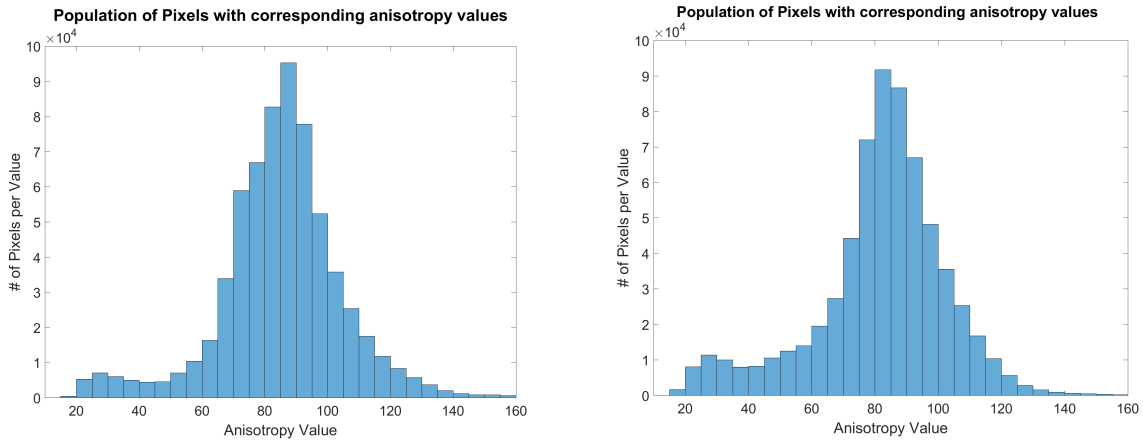

Figure 23 Histograms corresponding to pixel populations (FWHM for every pixel) shown in Figure 22. Note the right histogram, corresponding to the right image in Figure 22 located more caudally in the spine, has increased values between 40 and 60 degrees while the main large peaks are very similar.

A cumulative histogram method was devised to increase sensitivity to the small populations of ordered pixels in the image. The cumulative histogram sums the standard histogram bins from most ordered to most disordered and plots the cumulative value as the bins are progressively added to the sum. A rapid rise indicated the presence of many ordered pixels, which would quickly increase the cumulative sum causing a sharp rise in the line. Conversely the rise would

be slower across the cumulative histogram if the population of highly ordered pixels were lower. Cumulative histograms can be used to segment a population by determining the percentage of the population of pixels that have anisotropy values less than a certain value. This can be inverted, to determine the anisotropy value at which a fixed percentage of the population has equal or less anisotropy values.

A 5% population threshold was determined experimentally by generating many cumulative histograms from samples and applying different threshold levels. 5% was empirically found to provide the most sensitivity without inducing erratic changes in values across similar samples, such as groups of control or treatment samples. The resulting single number was the anisotropy value in which 5% of the pixels in the image had that anisotropy value or less. Image processing scripts were written in MATLAB (Mathworks, Natick, MA, USA) to extract these values from the images and display the color-coded anisotropy plots as well as the histograms and cumulative histograms.

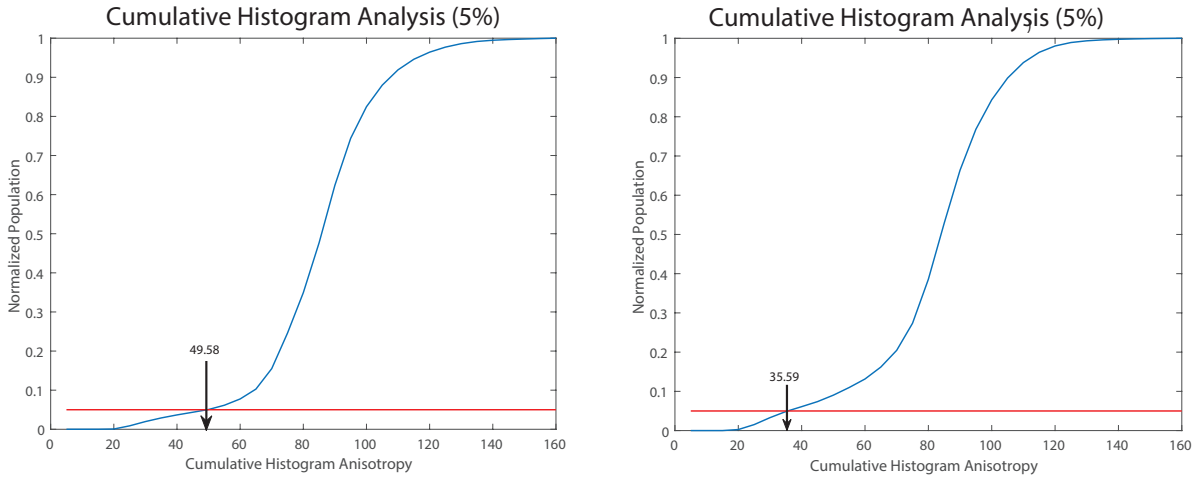

Figure 24 Cumulative histograms compiled from histograms shown in Figure 23. The red line demarcates the 5% threshold for evaluating the cumulative histogram population. The black arrows show the 5% crossing point and note the value on the horizontal scale. This value is taken as representative of the entire image for statistical purposes.

5.3. Live Sciatic Nerve

A live sample allows the monitoring of evolving disorder in myelin over short time scales. Sciatic nerve was selected for this test as it provides large diameter PNS axons with thick myelin. Sciatic nerve can also be pharmacologically treated to initiate myelin breakdown allowing control of the demyelination process during an experiment.

Sciatic nerve was harvested from C57BL/6 mice and placed in room-temperature oxygenated artificial cerebral spinal fluid (aCSF). The nerve was transferred to a live imaging perfusion chamber with circulating oxygenated aCSF. The chamber was positioned on the microscope stage and allowed to equilibrate for five minutes. During this time, live CARS imaging was performed to find a suitable site for imaging free of membrane debris or adipocytes (fat cells). The selected region was imaged every 10 minutes for up to 100 minutes.

5.3.1. Control Sciatic Nerve

The sciatic nerve was left in the imaging chamber at room temperature without administering any treatment. Oxygenated aCSF continued to be delivered to the nerve, which begin to deteriorate from being removed from the animal. This slow breakdown allowed the polarization CARS image series to be acquired with reduced sample movement compared to the glutamate treatment case. The processed anisotropy values are shown in Figure 25 indicating a relatively stable period followed by a consistent rise after 60 minutes.

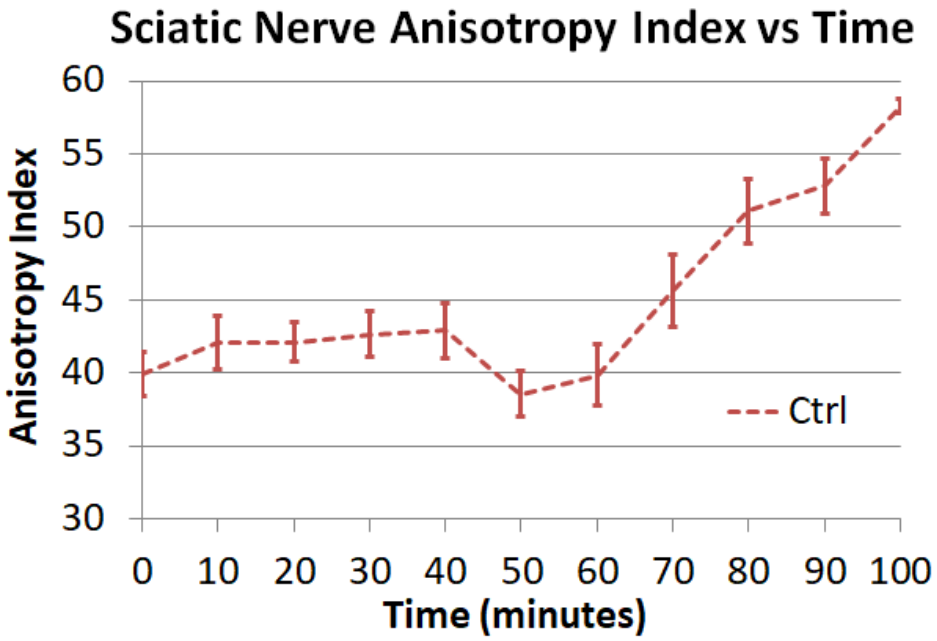

Figure 25 Cumulative histograms compiled from histograms shown in Figure 24. The red line demarcates the 5% threshold for evaluating the cumulative histogram population. The black arrows show the 5% crossing point and note the value on the horizontal scale. This value is taken as representative of the entire image for statistical purposes.

A sampling of images from one of the corresponding control series is shown in Figure 26. It is interesting to note that the image from the 70 minute mark shows an increase in both ordered and disordered pixels. This regional concurrent increase and decrease in disorder may explain the slight dip in the anisotropy index plot in Figure 25 prior to the sudden rapid increase in anisotropy index.

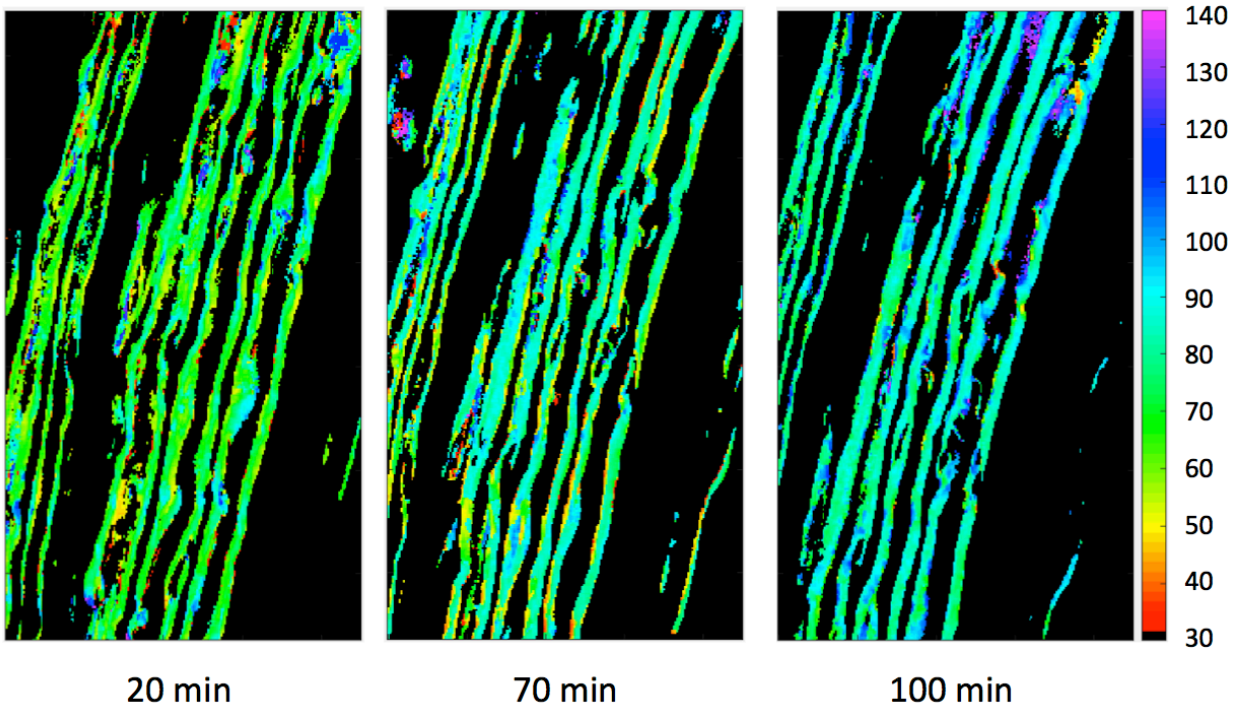

Figure 26 Selected frames from a sciatic nerve control time series. Blue colors indicate increasing disorder while red indicates increasing order. The 70 min time point shows an increase in both more ordered and more disordered pixels but the main bulk of myelin begins to show a shift towards the disordered state.

5.3.2. Glutamate NMDA Receptor Activation

Treatment tissue followed the same procedure as control samples with the following exception: A solution of 100 mM glutamate and 150 μM glycine was administered at the 10 minute time point to induce injury to the sciatic nerve. This produced rapid morphological changes that interfered with the acquisition of the CARS spectral data. The system required approximately 2 minutes to acquire the 13 images for each time point, and the sample shifted greatly during this time. Sequential images in each polarization series did not register properly and the recovered spectral data contained considerable artifact. The results are shown with the control sciatic in Figure 27.

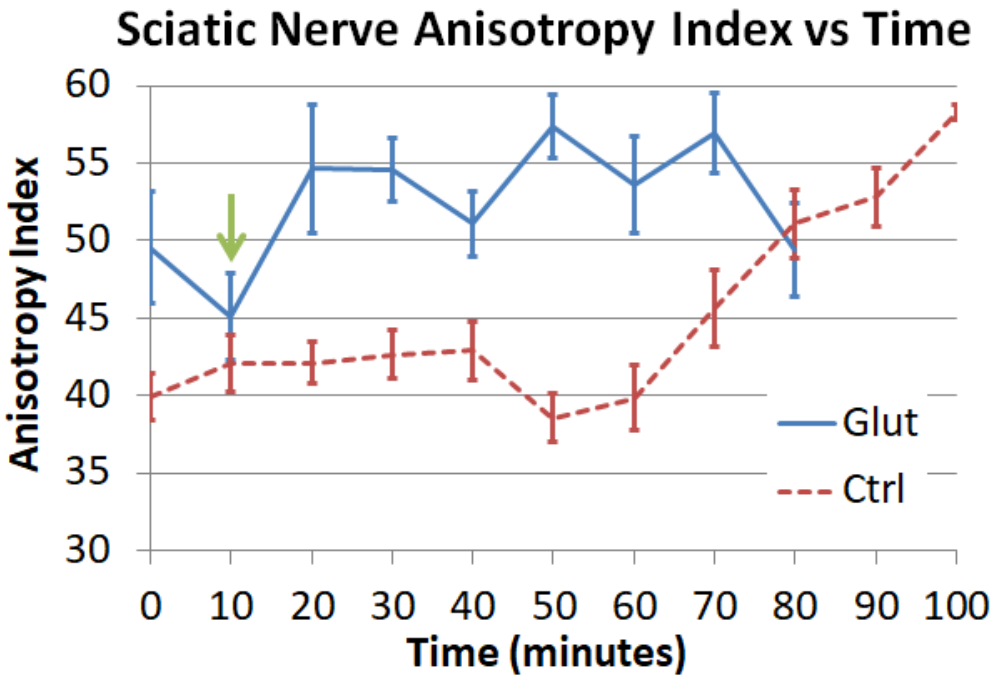

Figure 27 Cumulative Histogram Anisotropy Index for live C57BL/6 sciatic nerve. Glutamate treatment (Glut - solid line n=4) was applied at 10 minutes (green arrow). Control (Ctrl - dashed line n=10) received no treatment.

The different time zero anisotropy values for the glutamate treatment group compared to the control may have been artifact as the tissue recovered from the initial surgical trauma, but by 10 minutes the two groups approach each other. The images of the glutamate samples taken at t=10 minutes were acquired as the glutamate/glycine treatment was switched into the perfusion mixture, so there would be some delay between the effect of treatment and the image. The 20-minute time point shows considerable increase in anisotropy, implying that most of the disordering effect occurred between 10 and 20 minutes. The very small index increase from time 20 to 70 minutes for the treatment group implies that most of the change happened by time 20. The sharp drop at time 80 may be due to artifact, as the tissue tended contract more at this point in the experiment and the region would be lost.

5.4. Cuprizone Mouse Brain

C57BL/6 mice starting at age seven weeks were fed 0.2% cuprizone (CPZ) in the chow for two weeks. After this period, when the animals were 9 weeks old in total they were sacrificed and coronal brain sections were collected. The samples were slide-mounted and treated with 4% PFA. A positive control group was fed 0.5% CPZ starting at age seven weeks for 21 days total, and then sacrificed. The high dosage and long duration assured severe demyelination would occur. The samples were processed and fixed with the same method as the 0.2% treatment group. Finally a group of naïve mice received no CPZ, and were sacrificed at age 9 weeks to provide a reference against the 0.2% case. Brain sections were collected and fixed as per the 0.2% group. CARS images were acquired of the corpus callosum (CC) from the coronal sections taken from all three groups. The images were acquired lateral to medial along the corpus callosum. The sampling pattern is shown in a luxol fast blue (LFB) stained reference image in Figure 28.

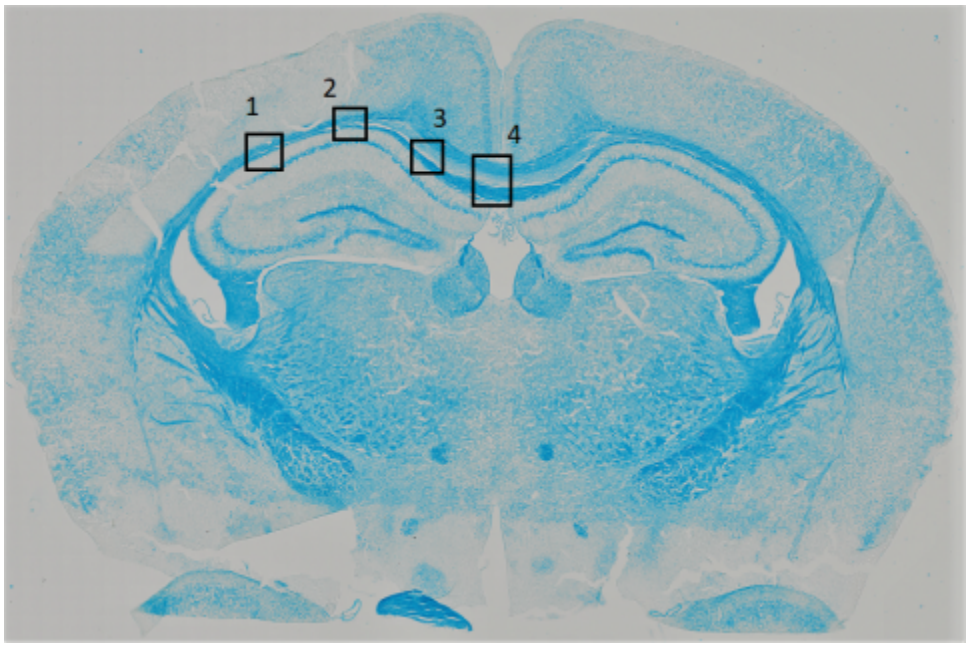

Figure 28 Luxol fast blue staining of C57BL/6 mouse brain slice showing myelin detail. Rectangles illustrate lateral to medial sampling pattern for acquiring polarization CARS images. The thick blue line followed by the rectangles is the corpus callosum.

The cumulative histogram anisotropy method was applied to the images acquired from three sample groups: Control mice which received no CZ treatment, 0.2% CZ for two weeks, and 0.5% CZ for three weeks. The two treatment groups were compared against the control using the Mann-Whitney Wilcoxon Rank Test. The regional statistics are shown in Figure 29.

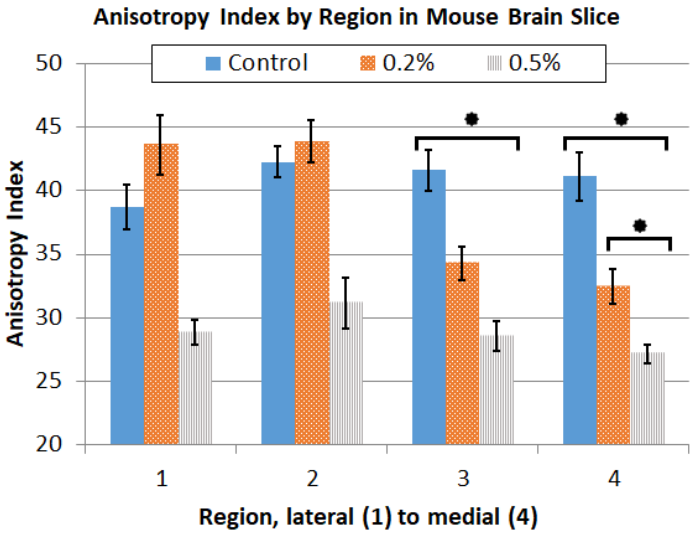

Figure 29 Anisotropy index for four regions within the corpus callosum of three sample groups. CZ treatments were 0.2% and 0.5% for two weeks. Error bars are standard error and the Mann-Whitney Wilcoxon rank test was used to test significance of the groups. Significance was found between control (n=13) and 0.5% treatment (n=5) for region 3, with p=0.019. The medial region of the corpus callosum showed significance for both the 0.2% (n=11) (p =0.026) and the 0.5% (p=0.010) groups.

The anisotropy index for the medial CC in the 0.5% treatment group was lower than 0.2%, which was lower than the control. This was the opposite of the expected result as lower numbers actually indicate a more ordered sample. Cholesterol may play a role in this, which will be discussed further in chapter 6. Representative CARS images of the medial CC (region 4) and the adjacent zone (region 3) are shown in Figure 30. The imaging data visualizes the FWHM plots of each pixel (compare to curve shown previously in Figure 21) The red coloration shown in the 0.5% experimental group (rightmost column) all show reddish values, indicating a lower index and higher order.

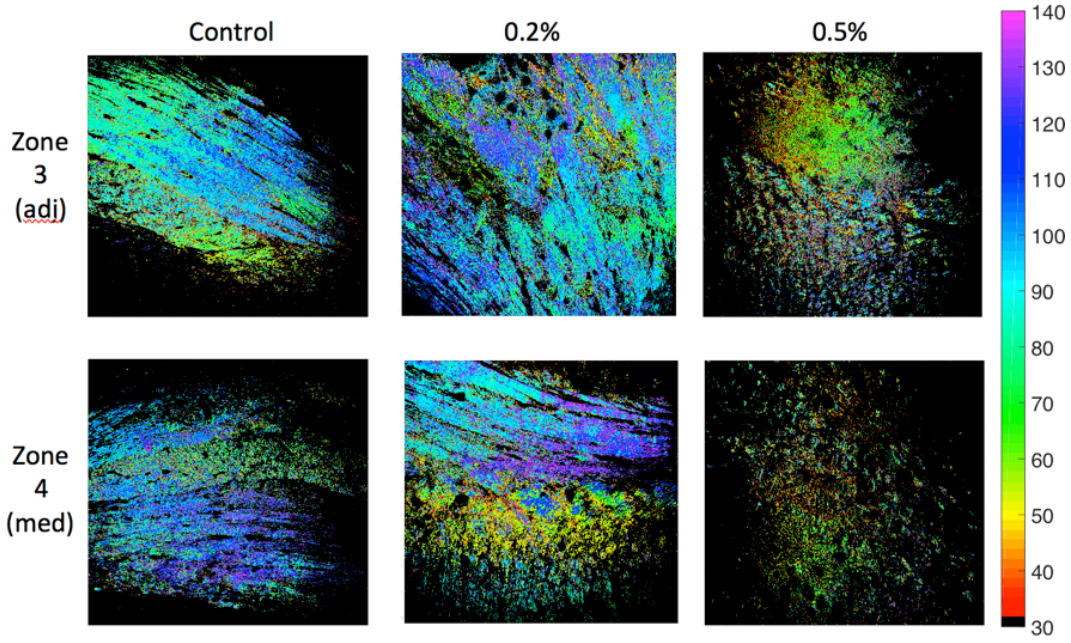

Figure 30 CARS FWHM anisotropy plots of region 3 (top row) and 4 (bottom row) in the corpus callosum (map shown in Figure 28 previously) for all experimental CPZ brain groups. Red (lower numbers) indicates a more ordered polarization response with a narrower FWHM.

5.5. Cuprizone Spinal Cord

Longitudinal spinal cord sections fixed in 4% PFA were imaged to determine any anisotropy difference between 0.5% CZ and control C57BL/6 mice in the cord. Images were acquired rostral to caudal at 0.5 mm spacing for a length of 4 mm in the cervical region of the cord. The mean of all eight regions was taken as a point for each animal in each group. The Mann-Whitney Wilcoxon Rank Test was applied to the data to verify significance between the CZ and control groups and the value was found to be $p = 0.017$. The results are shown in Figure 31.

These samples exhibited increased disorder for the positive control, similar to the ranges shown by the live sciatic nerve tests of 40 to 60 anisotropy index units. It is also notable that the literature indicated minimal change in the spinal cord in the CPZ model, yet there is a statistical difference measured by the polarized CARS anisotropy index method.

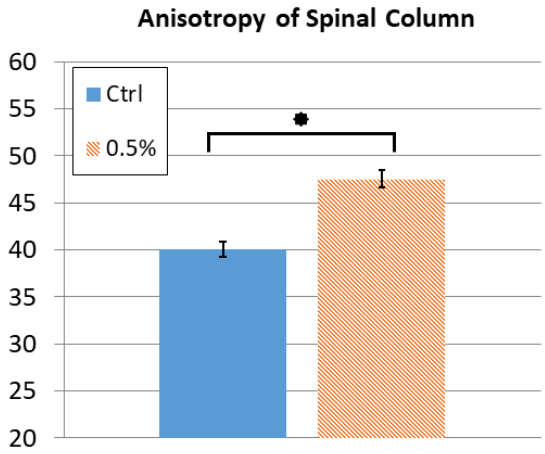

Figure 31 Cumulative histogram anisotropy results for cervical region of spinal cord for control (n=7 Ctrl, left) and 0.5% cuprizone treated (n=5 0.5%, right) C57BL/6 mice. Significance was verified by Mann-Whitney Wilcoxon with p = 0.017

5.6. Results Summary

These results have shown the ability to image myelin in a polarization-selective manner and display the results in a FWHM anisotropy plot. Images of control spinal cord were presented to illustrate the concept and show the differences observable between two locations on a spinal cord. The variation in anisotropy of medial CC in treatment and control was also presented as FWHM anisotropy plots, visually showing the difference between control, and low and high dose CPZ. This result was then also presented statistically using the cumulative histogram method, demonstrating the ability to extract single values representative of an entire image. The cumulative histogram method was then used to show the difference between spinal cord in CPZ treated animal vs. controls, which again showed a statistical difference. These results have proven the techniques ability to discern changes in myelin, and these results will be discussed further in the next chapter.

6. DISCUSSION

Successful polarization CARS imaging hinges on selective excitation of individual Raman resonances, and repeatable polarization excitation with adaptive power control. This combination targets the most polarization-sensitive Raman vibrations, while ensuring the instrument delivers consistent results.

6.1. Spectral Resolution

The CH_2 symmetric Raman vibration is highly prolific in lipid acyl chains and has a repeating, orderly distribution which exhibit a strong polarization response according to the literature. Other CH-related vibrations are less constrained, such as the CH_3 at the end of a chain, or in a ring structure such as the CH bonds in cholesterol. These vibrations will be less polarization-sensitive and will reduce the selectivity of polarization excitation if they are excited at the same time as the CH_2 symmetric. Imaging of the plastic reference beads provided a spectral reference to compare against spontaneous Raman. The structure of the peaks visible with CARS was very similar to the published Raman spectrum, showing peaks at the same location with similar intensity ratios. While the exact resolution is difficult to determine due to the asymmetric CARS lineshape, comparing the CARS result to the spontaneous Raman result for the C-H region for several plastics indicates that our resolution is comparable to the line width of the CH_2 symmetric vibration, approximately 18 cm^{-1} based on the published Raman spectrum.

6.2. Polarization Response

Polarization at the sample plane was tightly controlled by measurement with a polarimeter. The impact of intermediate optics such as filters is often overlooked in polarization studies, and controlling polarization distortions while maintaining constant power at the sample plane requires significant hardware. As part of a collaboration with Micu et al.,[59] I measured the polarization of confocal laser lines of several commercial systems, and noted differences between brands, lasers, and objective lenses, indicating that polarization can vary significantly from instrument to instrument, or even within an instrument if an optic changes. The CARS microscope was constructed from parts rather than using a commercial frame, but care was still required to maintain consistent excitation polarization.

The control and calibration system required considerable upkeep but heavy software automation kept the procedure within practical time scales. This allowed polarization and power calibrations to be completed at the start of every imaging session, ensuring reliability of the sample excitation from day-to-day. A manual approach would not have allowed this to be performed as frequently. Homogeneous oil samples revealed the polarization effects of the excited CARS signal, indicating a linear polarization return from the sample. This polarization was ellipticized when reflecting off the primary dichroic mirror to separate excitation wavelengths from emission. Without the analyzer in the detection path, the power varied less than 2.5%, for both the CH_2 and CH_3 vibrations. The change in polarization of the detected signal was only readily apparent by rotating an analyzer in the detection path. This measured a power variation of 30% for CH_2 and 10% for CH_3 between +45 and -45 degrees.

The detecting photomultiplier tube showed no polarization preference in the absence of the analyzer, ensuring consistent signal across excitation polarization states when imaging samples

that generate a polarized anti-Stokes response. This was important as it allows decoupling of the polarization of the generated anti-Stokes signal from the polarized pump and Stokes excitation. If the detection path showed a polarization preference the experimental results would be a combination of both effects. While it will be interesting in the future to revisit the polarization of the detected light, for now this work concentrates on the effects of the polarized excitation.

Polarization can also be altered in the focus of high numerical aperture (NA) microscope objectives. Even assuming the lens transmits the polarization properly, the effects of strong focusing cause distortion. [194] Kang et al. investigated the polarization output of a simulated 1.1 NA lens for linear and radial polarization cases. Kang profiled the change in polarization throughout the focus of the lens, showing small angular changes near the focus. A key point of their findings were that the polarization distortions were symmetric, so a clockwise tilt slightly to one side of the focus would be compensated by a counter-clockwise tilt on the other side. If the beam were static, this would cause a spatial profile in the response of a sample to the excitation. In the case of a laser-scanning system, however, the focus is swept over the region while the signal is integrated. With a symmetric distortion swept through the sample, the ensemble of multiple oscillators transiting the focus may average this out.

Ranasinghesagara et al. [76] considered the impact of scatters in the light field of a CARS microscope near the focus. As part of that work the effect of polarization was calculated in addition to overall efficiency of CARS signal production. The polarization result was interesting in that it showed a degree of symmetry when the virtual scattering object was offset from the optical axis. As per the work of Kang it can be envisaged that a scanning beam pattern may average out effects for scatters smaller than the focus.

6.3. Myelin Experiments

A limitation to any CARS imaging with myelin is the dependence on high concentration of lipids for generating a signal. As myelin deteriorates the lipid concentration decreases as the sheath comes apart. This limits the ability of CARS to image end-stage demyelination as signal decreases below the ability to clearly detect it. For polarization-resolved CARS this impacts the ability to measure the most disordered myelin, as near complete disorder implies a severe loss of packing density.

This concentration dependence is not limiting for the purposes of this experiment, as this work is attempting to characterize early phase myelin pathology. Existing histopathology and fluorescence methods are more effective, and well established, for identifying end-case demyelination. This work does not propose to replace these tried-and-true methods but instead seeks to offer a supplementary measure of more subtle myelin changes.

6.3.1. Sciatic Nerve

As discussed in the literature review, glutamate triggers influx of calcium in nerves by activation of NMDA, AMPA, and kainate receptors through either attacking the energy pathways of the cell (mitochondrial damage) or activation of enzymes such as phospholipase or calpain. The intent of the glutamate treatment was to induce a combination of chemical ischemia and enzymatic damage to induce myelin breakdown. While the cuprizome treatment animals could take weeks to demyelinate, and then be examined at fixed time points, live imaging required a faster myelin breakdown process.

The original experiment for this model used Fourier image analysis to determine myelin damage by quantifying structural changes by measuring spatial frequency. [157] This is a way of measuring

anisotropy in tissues, but at large scales as it relies on morphological changes on the order of the pixel size to be detectible. The treatment used here matched the treatment protocol for this level of damage and in retrospect may have been too aggressive for the smaller scales and more subtle results the polarized CARS method seems to operate on.

The glutamate treated sciatic nerve experienced rapid morphological changes on the time scale of the acquisition of the 13 polarization images. This caused spatially noisy acquisition as the polarization data was corrupted by adjacent pixels or even background as the sample moved. While a lower dose of glutamate may have triggered a slower response,[156] the untreated control samples actually worked well for the purpose of providing a measured rate of myelin disruption. The slight dip in index at approximately 50-60 minutes may be indicative of a subtle change in the lipids prior to the more progressive disordering observed at 70 minutes and onward.

An additional positive aspect of the results is that polarization imaging was able to detect differences in the order of the myelin under what appeared to be slow morphological changes. The structure of the myelin did not exhibit gross disruption yet an increase in the disorder was detected after the samples were at rest after approximately one hour. This was observed both in the anisotropy index analysis, and seen visually in sample images ,which showed only slight morphological change while the index increased rapidly.

6.3.2. Spinal cord

The cuprizone demyelination model is well known for damage to the corpus callosum; however observation of the spinal cord shows no firm indications of damage using histopathological methods, although some myelin basic protein expression levels seemed abnormal. No myelin debris was visible in the spinal cord, whereas in the brain puncta were detected. [150] The lack of

obvious results using conventional methods made the spinal cord samples a good test case for detection of changes in the myelin with polarization sensitive CARS.

Acs et al.[195] examined the presence of Cu/Zn superoxide dismutase (SOD) in the corpus callosum and spinal cord of mice. Biochemical assay was used to measure Cu/ZnSOD in the corpus callosum and the cord. The CC samples showed greatly reduced levels of Cu/ZnSOD while the spinal cord only exhibited a slight decrease. This enzyme has antioxidant effects and aids in partitioning free radical oxygen into O_2. Is it suspected that free radical production by mitochondria is partly why oligodendrocyte death occurs, so Cu/ZnSOD decreasing drastically in the brain may indicated free radical activity, whereas in the spine the slight decrease in Cu/ZnSOD could indicate a reduced level of free radical production. This result may be linked to the effect of cholesterol, as oxidized cholesterol becomes a variety of oxysterols with many implications for cell signaling and enzymatic activity. [196]

While a full discussion of the biochemical ramifications would be beyond the scope of this work, the subtle secondary effects seen in many biochemical pathways in the CPZ spine that are greatly muted in the cord, suggests a reduced pathology that involves cholesterol in some form.

6.3.3. Order Enhancement in CPZ Brain

Myelin damage in the corpus callosum (CC) of CPZ treated mice is well documented and is considered a reliable model of demyelination. [197] The 0.5% treatment protocol is known to cause severe demyelination while the 0.2% treatment protocol causes intermediate effects. The scalability of the result provides a positive control with aggressive treatment and a ‘challenge’ sample with reduced treatment.

The most pronounced demyelination of the CC occurs in the medial region at the center of the band, and samples were imaged from the lateral to medial region to determine if there was a regional gradient in the myelin order. The previous sciatic and spinal cord samples indicated an increase in the anisotropy index value with increasing damage, but unexpectedly the CPZ samples in the corpus callosum exhibited a decrease. The decrease also appeared proportional to the degree of CPZ treatment, with the 0.5% showing lower indices (ie more order) than the 0.2%, which in turn were lower than the control samples.

The differences detected in the medial CC of the 0.2% CPZ treatment brains were noteworthy as standard staining protocols do not show much difference at this treatment level. An example of luxol fast blue (LFB) staining of control and 0.2% CC for two weeks is shown in Figure 32, for comparison.

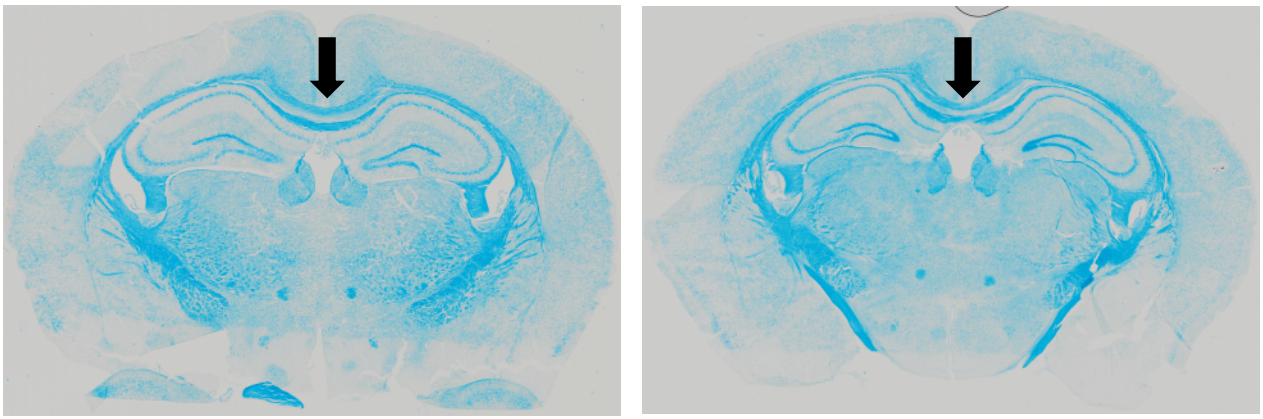

Figure 32 Luxol fast blue staining of control (left) and 0.2% treatment (right) CPZ brain slice. The black arrow in both images indicates the medial CC which is the region most sensitive to demyelination. Note the visual similarity between control and treatment.

While unexpected, there is some evidence that the decrease in the disorder index may be highlighting the interaction between CPZ and cholesterol in myelin. The LFB staining of the control and 0.2% treatment showed very little difference in visible stained myelin. It is known

that LFB does not stain cholesterol, so it would fail to show any changes in cholesterol in the tissue. [198]

Many previous works [146,197,199-201] have observed decreased serum levels of cholesterol and increased levels of oxidized cholesterol in the CSF. Berghoff et al. imaged the corpus callosum (CC) of control and CPZ mice using bodipy-cholesterol to fluorescently label cholesterol. The CC sections of the CPZ mice showed granular deposits of bodipy cholesterol in the medial CC, whereas control samples did not show this.

The process of CPZ demyelination appears to involve some form of cholesterol removal from the myelin relatively early in the process. Praet speculated that early oligodendrocyte cell death left the myelin initially intact, but metabolically unsupported. Cholesterol may be one of the earlier components to oxidize or break down in the myelin, and without oligodendrocytes to maintain a supply this would lead to a net decrease. Berghoff's observation of cholesterol granules shows that immune cells may be collecting cholesterol at early points in the CPZ process as well.

This is significant as cholesterol is a major mediator of myelin fluidity. The presence of cholesterol maintains the spacing of other lipid components within the membrane to hold the myelin layers in a gel state. Removing the cholesterol removes this spacing effect, and the myelin moves towards a more solid state. [202] [203] This would increase the packing density of the acyl tails of the lipids and constrain their movement. Given that the reduction in anisotropy index compared to control is proportional to the CPZ treatment dose, the effect seems dependent on the amount of CPZ used. This result has presented potential insight to the impact of CPZ on the packing structure of myelin through a possible link with cholesterol mediation.

6.4. Comparison to Previous Polarization CARS Methods

Numerous other groups have successfully pursued polarization-resolved imaging of lipids in myelin and myelin-like constructs such as vesicles or myelin figures. These methods have been discussed in the literature review, and a comparison of the key points of those methods to the work presented in this manuscript is considered below.

6.4.1. Acquisition Speed

A common limitation in these works is the acquisition speed of the necessary polarization-resolved images for analysis of anisotropy and orientation. Consecutive images of the same region must be acquired for multiple angles of collinearly polarized pump and Stokes to obtain the angle dependency of the anti-Stokes signal. The use of motorized waveplates is a common limiting factor both in the previously discussed works and the work presented in this manuscript. The delay required to rotate the excitation polarization limits the rate at which a polarization 'stack' of images can be acquired. The work of Piazza and de Vito attempted to address this issue with a freely rotating waveplate for rapid sweeping of the linearly polarized pump and Stokes. While this allowed rapid changes in polarization, the need for lock-in detection to synchronize image scanning with polarization angle eliminated the speed gains of this method. Polarization-resolved information was actually acquired on time scales comparable to the ubiquitous slow waveplate rotation method used in this work and others.

Pixel dwell times of the works presented in the literature review were on the order of tens of microseconds in the best case. This is likely due to the high-repetition rate, low pulse energy sources employed which all tended to require significant averaging or long pixel dwell to achieve useful signal to noise levels. The method herein is unique in the application of high-energy

pulses generated by optical parametric amplification, eliminating the need for any averaging in the acquisition of the CARS signal. The pixel dwell time of 2 μs from this approach is an order of magnitude faster than that presented in the reviewed works.

To compensate for limited acquisition speeds the presented works imaged relatively small fields of view with a limited number of pixels. 50-100 μm fields were typical with pixel sizes of 0.5 μm, with 100x100 pixel images being common. In comparison, the rapid pixel dwell used in this work permitted fields of 512 x 512 pixels with pixel sizes ranging from 0.5 to 0.25 μm. Given that the anisotropy information is acquired on a pixel-level for all methods, collecting a larger number of pixels for a given region provides greater detail within a region or allows collection of information from a larger region. This improves the ability of polarization-resolved CARS to gather statistical information for larger sample regions in a single image series, or gather more finely resolved pixel-wise information.

Fast sequential acquisition of images also limits motion artifact, and allows the imaging of short-term activity. The live sciatic control and glutamate model presented in this work was imaged in 10 minute intervals over periods in excess of an hour. Similar dynamic samples were not presented in any of the reviewed works.

Finally, rapid image acquisition without averaging allows continuous display of the imaged region to the user. This allows smooth navigation throughout a sample to rapidly identify regions of interest and adjust focus. This was particularly important for the previously-mentioned live sciatic nerve samples, as the live samples inevitably drifted in focus over the duration of the experiment. The rapid imaging capability allowed the focal plane to be rapidly reacquired prior to each polarization series ensuring the same region was imaged over the duration of the experiment.

6.4.2. Transmitted vs. Epi-Detection

Minimally destructive imaging of live samples would ideally avoid the need for thin sectioning. In vivo or whole tissue ex vivo imaging allows the structure of the sample to be maintained. Epi-detection, where a single lens both delivers excitation and collects signal, is preferred for this form of imaging. Transmitted techniques require access to opposite sides of the tissue, typically requiring thin sections or inherently thin samples. This limits sample selection and the preservation of structure of tissues. The circular polarization excitation technique employed by Cleff and Bioud, allow acquisition of polarization data in a much simpler manner than rotation of linear states. While the technique was still limited in speed by the need to compensate for the non-resonant background and low signal, (50 μs pixel dwell times typical) the need to only acquire two images for complete polarization-resolved images reduced the time required for data acquisition. The method as implemented required the manual rotation of a quarter waveplate to select between clockwise and counter-clockwise excitation although this could be straightforwardly automated for very rapid imaging. An unfortunate limitation of the technique was the need to collect circularly polarized anti-Stokes signal from the sample to determine the symmetry and orientation information. This was collected in the forward direction from thin-sectioned samples to preserve the polarization state of the emitted light. Epi-detection would not be feasible for this method as the back-scattered forward-propagating signal would experience polarization distortions, which would occlude the necessary polarization information in the detected signals. In contrast, the method used in this work collects back-scattered signal without requiring polarization information, and in fact the detection path was proven to be polarization-agnostic in section 5.1. Additionally, CARS is inherently forward-propagating, so typical

methods invoking low-energy pulses are often limited by the losses inherent to collecting the back-scatter of a forward-propagating signal requiring transmitted detection schemes.

6.4.3. Spectral Selectivity and Background Signal

Different vibrational modes exhibit varying degrees of sensitivity to polarization. To maximize the polarization-dependent result of the sample it is essential to excite only the most polarization-sensitive vibrations. If multiple vibrational modes are excited with various degrees of polarization sensitivity the overall dependence will be diluted. The majority of published reports utilized narrowband picosecond lasers to ensure Raman selectivity, however the lower energy pulses emitted by these lasers were a factor in the longer acquisition times for these systems. Piazza et al used femtosecond sources, initially using a narrowband filter to limit spectral content, but eventually switching to a glass block spectral focusing method similar to this work. In the case of Piazza and co-workers, the blocks were of fixed length, precluding any adjustability. While the femtosecond titanium sapphire and optical parametric oscillator sources are more energetic than picosecond lasers, they emit less energetic pulses compared to an OPA. This limits the degree to which the emitted pulses can be stretched while maintaining high peak energy, which in turn limits the spectral selectivity of the system. Piazza was still able to selectively target the CH_2 symmetric vibration, which provides the greatest polarization contrast within the lipid region.

The importance of spectral selectivity is also evident in the work of Gasecka[112], who used femtosecond pulses with no dispersion control or bandwidth limiting. This maintained high peak energy, allowing relatively short 20 μs pixel dwell times, but the estimated excited vibrational span of the system was 150 cm^{-1}. This would excite both CH_2 symmetric and asymmetric modes,

and also approaches the CH_3 antisymmetric mode that is polarization insensitive. Indeed Gasecka noted the presence of a large background signal that did not appear to vary with excitation polarization. While it was not noted whether this was due to excessive nonresonant background (also a difficulty with broadband CARS as discussed in the Theory section) or simultaneous excitation of less polarization-sensitive vibrations, the signal was on the order of 25% of the polarization-sensitive signal. If contributions from CH_2 asymmetric or CH_3 antisymmetric modes were present in this data then Gasecka could have underestimated the overall anisotropy response.

6.5. Conclusions and Future Directions

The interpretation of the polarized CARS data required testing and observation of actual samples. The full-width half-maximum polarization plots with respect to intensity provided pixel-level information on organization, but applying this information across an entire image proved ineffective. Deterioration of the myelin was not always global across an entire image, as shown in the presented sciatic images. The 70 minute time point image displayed an increase of both ordered and disordered pixels compared to the mean. These small regional variations were still detected by the cumulative histogram method, which proved capable of enhancing detection of regional variability in a global interpretation of an image.

The histogram method provided insight to the population of ordered regions within the image, but a single number was still required as a metric for the overall order in an image. Observation of the histograms of many samples indicated a tendency for more variability in the higher-order portions of the histogram, (points with an index less than 40-50) so a cumulative histogram approach was applied. Smaller changes in order were more pronounced by observing the rise of

the cumulative histogram rather than trying to interpret mean values. The 5% threshold for readout was determined experimentally by generating many cumulative histograms from samples and applying different threshold levels. 5% was empirically found to provide the most sensitivity without inducing erratic changes in values across similar samples, such as groups of control or treatment samples.

The end goal of this work was to prove the efficacy of polarization-resolved CARS for detecting changes in myelin. A polarization and spectrally-controlled CARS microscope system was designed and constructed for delivering polarized excitation to the sample in a repeatable manner. Protocols and control samples for maintenance and monitoring of the excitation, and collection of the emission light were developed and regularly employed.

An anisotropy indexing method was developed for interpreting the results from polarized CARS imaging. This method was applied to control and treatment brain and spinal cord using the cuprizone demyelination animal model and sciatic nerve using a glutamate and control ex vivo model. The results of these experiments indicated myelin order change in subtle samples, such as the CPZ spinal cord which does not typically show differences in myelin using standard methods. While the acquisition rate of the system limited the ability to resolve fast myelin changes in the glutamate live sciatic nerve model, slower changes in order were apparent in control sciatic nerve. These results show that polarization-resolved CARS is capable of imaging and determining the order of the myelin sheath.

For future work, and exploration of cholesterol may help to explain the observations in the CPZ brain samples. Repeating this experiment for the Raman vibration 2930 cm^{-1}, associated with cholesterol [74] may explain the difference in CPZ brain compared to CPZ spinal cord. The next

steps will be to repeat the CPZ imaging while also measuring the 2930cm^{-1} Raman vibration to see if there is a difference in the strength of this band between treatment and controls.

References

1. Squire LR. *Encyclopedia of Neuroscience*. Elsevier Academic Press; 2009.

2. Podbielska M, Hogan EL. Molecular and immunogenic features of myelin lipids: incitants or modulators of multiple sclerosis? *Mult Scler*. 2009;15(9):1011-1029. doi:10.1177/1352458509106708.

3. Compston A, Coles A. Multiple sclerosis. *The Lancet*. 2008;372(9648):1502-1517. doi:10.1016/S0140-6736(08)61620-7.

4. MD PAJT, MD PBLB, MD PFB, et al. Diagnosis of multiple sclerosis: 2017 revisions of the McDonald criteria. *The Lancet Neurology*. 2018;17(2):162-173. doi:10.1016/S1474-4422(17)30470-2.

5. Thompson AJ, Montalban X, Barkhof F, et al. Diagnostic criteria for primary progressive multiple sclerosis: a position paper. *Ann Neurol*. 2000;47(6):831-835.

6. Matute C, Pérez-Cerdá F. Multiple sclerosis: novel perspectives on newly forming lesions. *Trends in Neurosciences*. 2005;28(4):173-175. doi:10.1016/j.tins.2005.01.006.

7. MD DO, MD PAJT, MD PRJF, MD DPJAC. Multiple sclerosis 3 Progressive multiple sclerosis: prospects for disease therapy, repair, and restoration of function. *The Lancet*. 2017;389(10076):1357-1366. doi:10.1016/S0140-6736(16)31320-4.

8. Kuhlmann T, Ludwin S, Prat A, Antel J, Brück W, Lassmann H. An updated histological classification system for multiple sclerosis lesions. *Acta Neuropathol*. 2016;133(1):13-24. doi:10.1007/s00401-016-1653-y.

9. Stadelmann C, Wegner C, Brück W. Inflammation, demyelination, and degeneration — Recent insights from MS pathology. *BBA - Molecular Basis of Disease*. 2011;1812(2):275-282. doi:10.1016/j.bbadis.2010.07.007.

10. Hauser SL, Oksenberg JR. The Neurobiology of Multiple Sclerosis: Genes, Inflammation, and Neurodegeneration. *Neuron*. 2006;52(1):61-76. doi:10.1016/j.neuron.2006.09.011.

11. Schmued L, Slikker W. Black-gold: a simple, high-resolution histochemical label for normal and pathological myelin in brain tissue sections. *Brain Research*. 1999;837(1-2):289-297. doi:10.1016/S0006-8993(99)01624-8.

12. Gallyas F. Silver staining of myelin by means of physical development. *Neurological Research*. 1979;1(2):203-209. doi:10.1080/01616412.1979.11739553.

13. Goto N. Discriminative staining methods for the nervous system: Luxol fast blue-periodic acid-schiff- hematoxylin triple stain and subsidiary staining methods. *Biotechnic & Histochemistry*. 1987;62(5):305-315. doi:10.3109/10520298709108015.

14. Hamano K, Iwasaki N, Takeya T, Takita H. A quantitative analysis of rat central nervous system myelination using the immunohistochemical method for MBP. *Brain Res Dev Brain Res*. 1996;93(1-2):18-22. doi:10.1016/0165-3806(96)00025-9.

15. Aarli JA, Aparicio SR, Lumsden CE, Tonder O. Binding of normal human IgG to myelin sheaths, glia and neurons. *Immunology*. 1975;28(1):171-185.

16. Lisak RP, Zwiman B, Norman M. Antimyelin Antibodies in Neurologic Diseases: Immunofluorescent Demonstration. *Arch Neurol*. 1975;32(3):163-167. doi:10.1001/archneur.1975.00490450043005.

17. Wang C, Wu C, Zhu J, Miller RH, Wang Y. Design, Synthesis, and Evaluation of Coumarin-Based Molecular Probes for Imaging of Myelination. *J Med Chem*. 2011;54(7):2331-2340. doi:10.1021/jm101489w.

18. Wang Y, Wu C, Caprariello AV, et al. In Vivo Quantification of Myelin Changes in the Vertebrate Nervous System. *Journal of Neuroscience*. 2009;29(46):14663-14669. doi:10.1523/JNEUROSCI.4082-08.2009.

19. Noback CR, Strominger NL, Demarest RJ, Ruggiero DA. *The Human Nervous System: Structure and Function: Sixth Edition*. Totowa, NJ: Humana Press; 2005:1-477. doi:10.1007/978-1-59259-730-7.

20. Brodal P. *The Central Nervous System*. Oxford University Press; 2016.

21. Debanne D, Campanac E, Bialowas A, Carlier E, Alcaraz G. Axon physiology. *Physiol Rev*. 2011;91(2):555-602. doi:10.1152/physrev.00048.2009.

22. Thomas RC. Electrogenic sodium pump in nerve and muscle cells. *Physiol Rev*. 1972;52(3):563-594. doi:10.1152/physrev.1972.52.3.563.

23. Strominger NL, Demarest RJ, Laemle LB. *Noback's Human Nervous System, Seventh Edition: Structure and Function*. Vol 9781617797798. Totowa, NJ: Humana Press; 2012:1-469. doi:10.1007/978-1-61779-779-8.

24. Wollner DA, Catterall WA. Localization of sodium channels in axon hillocks and initial segments of retinal ganglion cells. *Proc Natl Acad Sci USA*. 1986;83(21):8424-8428.

25. Fields RD. Myelin - More than insulation. *Science*. 2014;344(6181):264-266. doi:10.1126/science.1253851.

26. Carroll SL. The Molecular and Morphologic Structures That Make Saltatory Conduction Possible in Peripheral Nerve. *J Neuropathol Exp Neurol*. 2017;76(4):255-257. doi:10.1093/jnen/nlx013.

27. Richardson AG, McIntyre CC, Grill WM. Modelling the effects of electric fields on nerve fibres: influence of the myelin sheath. *Med Biol Eng Comput*. 2000;38(4):438-446.

28. Hille B. *Ion Channels of Excitable Membranes*. Sunderland, Mass. : Sinauer; 2001.

29. Arancibia-Carcamo IL, Attwell D. The node of Ranvier in CNS pathology. *Acta Neuropathol*. 2014;128(2):161-175. doi:10.1007/s00401-014-1305-z.

30. Aggarwal S, Yurlova L, Simons M. Central nervous system myelin: structure, synthesis and assembly. *Trends in Cell Biology*. 2011;21(10):585-593. doi:10.1016/j.tcb.2011.06.004.

31. Williams KA, Deber CM, Klrschner OA. The Structure and Function of Central Nervous System Myelin. *Critical Reviews in Clinical Laboratory Sciences*. 2008;30(1):29-64. doi:10.3109/10408369309084665.

32. Hartline DK. What is myelin? *Neuron Glia Biol*. 2008;4(2):153-163. doi:10.1017/S1740925X09990263.

33. Berger BL, Gupta R. Demyelination secondary to chronic nerve compression injury alters Schmidt-Lanterman incisures. *J Anat*. 2006;209(1):111-118. doi:10.1111/j.1469-7580.2006.00561.x.

34. Deber CM, Reynolds SJ. Central nervous system myelin: structure, function, and pathology. *Clin Biochem*. 1991;24(2):113-134. doi:10.1016/0009-9120(91)90421-A.

35. Salzer JL. Clustering sodium channels at the node of Ranvier: Close encounters of the axon-glia kind. *Neuron*. 1997;18(6):843-846. doi:10.1016/S0896-6273(00)80323-2.

36. Kiernan JA. Histochemistry of Staining Methods for Normal and Degenerating Myelin in the Central and Peripheral Nervous Systems. *Journal of Histotechnology*. 2013;30(2):87-106. doi:10.1179/his.2007.30.2.87.

37. Han H, Myllykoski M, Ruskamo S, Wang C, Kursula P. Myelin-specific proteins: A structurally diverse group of membrane-interacting molecules. *BioFactors*. 2013;39(3):233-241. doi:10.1002/biof.1076.

38. Suter U. Myelin: keeping nerves well wrapped up. *Curr Biol*. 1997;7(1):R21-R23. doi:10.1016/S0960-9822(06)00011-X.

39. Smith ME, Eng LF. The turnover of the lipid components of myelin. *J Am Oil Chem Soc*. 1965;42(12):1013-1018. doi:10.1007/BF02636894.

40. Yurlova L, Kahya N, Aggarwal S, et al. Self-segregation of myelin membrane lipids in model membranes. *Biophys J*. 2011;101(11):2713-2720. doi:10.1016/j.bpj.2011.10.026.

41. Weil M-T, Möbius W, Winkler A, et al. Loss of Myelin Basic Protein Function Triggers Myelin Breakdown in Models of Demyelinating Diseases. *CellReports*. 2016;16(2):314-322. doi:10.1016/j.celrep.2016.06.008.

42. Hu Y, Doudevski I, Wood D, et al. Synergistic interactions of lipids and myelin basic protein. *Proc Natl Acad Sci USA*. 2004;101(37):13466-13471. doi:10.1073/pnas.0405665101.

43. Chrysikopoulos HS. *Clinical MR Imaging and Physics: a Tutorial*. Berlin, Heidelberg: Springer Berlin Heidelberg; 2009:1-176. doi:10.1007/978-3-540-78023-6.

44. Ali TS, Bjarnason TA, Senger DL, Dunn JF, Joseph JT, Mitchell JR. QuantitativeT2: interactive quantitative T2 MRI witnessed in mouse glioblastoma. *J Med Imag*. 2015;2(3):036002-036013. doi:10.1117/1.JMI.2.3.036002.

45. Ding X, Wang R, Zhang H, et al. Generation of 3.5W high efficiency blue-violet laser by intracavity frequency-doubling of an all-solid-state tunable Ti:sapphire laser. *Opt Express, OE*. 2008;16(7):4582-4587. doi:10.1364/OE.16.004582.

46. Mackay A, Whittall K, Adler J, Li D, Paty D, Graeb D. In vivo visualization of myelin water in brain by magnetic resonance. *Magn Reson Med*. 1994;31(6):673-677. doi:10.1002/mrm.1910310614.

47. Laule C, Leung E, Li DK, et al. Myelin water imaging in multiple sclerosis: quantitative correlations with histopathology. *Mult Scler*. 2016;12(6):747-753. doi:10.1177/1352458506070928.

48. Henkelman RM, Stanisz GJ, Graham SJ. Magnetization transfer in MRI: a review. *NMR Biomed*. 2001;14(2):57-64. doi:10.1002/nbm.683.

49. Filippi M, Agosta F. Magnetization Transfer MRI in Multiple Sclerosis. *J Neuroimaging*. 2007;17(suppl 1):22S–26S. doi:10.1111/j.1552-6569.2007.00132.x.

50. Kozlowski P, Raj D, Liu J, Lam C, Yung AC, Tetzlaff W. Characterizing white matter damage in rat spinal cord with quantitative MRI and histology. *J Neurotrauma*. 2008;25(6):653-676. doi:10.1089/neu.2007.0462.

51. Olivier Commowick PFOCASKW. LNCS 5241 - Detection of DTI White Matter Abnormalities in Multiple Sclerosis Patients. July 2008:1-8.

52. Rafee MA, Amarpal, Sharma GT. Comparison of Hematoxylin and Eosin staining with and without pre treatment with Marchi's solution on nerve samples for nerve degeneration and regeneration studies. *Explor Anim Med Res*. 2018;7(2):206-209.

53. Gerrits PO, Brekelmans-Bartels M, Mast L, Gravenmade EJ, Horobin RW, Holstege G. Staining myelin and myelin-like degradation products in the spinal cords of chronic experimental allergic encephalomyelitis (Cr-EAE) rats using Sudan black B staining of glycol methacrylate-embedded material. *Journal of Neuroscience Methods*. 1992;45(1-2):99-105. doi:10.1016/0165-0270(92)90047-H.

54. Ineichen BV, Weinmann O, Good N, et al. Sudan black: a fast, easy and non-toxic

method to assess myelin repair in demyelinating diseases. *Neuropathology and Applied Neurobiology*. 2017;43(3):242-251. doi:10.1111/nan.12373.

55. Yen K, Le TT, Bansal A, Narasimhan SD, Cheng J-X, Tissenbaum HA. A Comparative Study of Fat Storage Quantitation in Nematode Caenorhabditis elegans Using Label and Label-Free Methods. Melov S, ed. *PLoS ONE*. 2010;5(9):e12810-e12810. doi:10.1371/journal.pone.0012810.

56. Ivanova MV, Zakharova MN. Antibodies against Myelin Lipids in Multiple Sclerosis. *Hum Physiol*. 2018;43(8):875-880. doi:10.1134/S0362119717080023.

57. Quarles RH, Macklin WB, Morell P. Myelin Formation, Structure and Biochemistry. In: Siegel GJ, Agranoff BW, Albers RW, eds. *Basic Neurochemistry Molecular, Cellular and Medical Aspects*. 6 ed. Philadelphia: Lippincott-Raven; 1999:1-21.

58. Timr Š, Brabec J, Bondar A, et al. Nonlinear Optical Properties of Fluorescent Dyes Allow for Accurate Determination of Their Molecular Orientations in Phospholipid Membranes. *J Phys Chem B*. 2015;119(30):9706-9716. doi:10.1021/acs.jpcb.5b05123.

59. Micu I, Brideau C, Lu L, Stys PK. Effects of laser polarization on responses of the fluorescent Ca 2+indicator X-Rhod-1 in neurons and myelin. *Neurophoton*. 2017;4(2):025002-025010. doi:10.1117/1.NPh.4.2.025002.

60. Gavrilyuk S, Polyutov S, Jha PC, Rinkevicius Z, Ågren H, Gel'mukhanov F. Many-Photon Dynamics of Photobleaching. *J Phys Chem A*. 2007;111(47):11961-11975. doi:10.1021/jp074756x.

61. Monici M. Cell and tissue autofluorescence research and diagnostic applications. In: Vol 11. Biotechnology Annual Review. Elsevier; 2005:227-256. doi:10.1016/S1387-2656(05)11007-2.

62. Maker PD, Terhune RW. Study of optical effects due to an induced polarization third order in the electric field strength. *Physical Review*. 1965;137(3A):A801-A818. doi:10.1103/PhysRev.137.A801.

63. Tolles WM, Nibler JW, McDonald JR, Harvey AB. A Review of the Theory and Application of Coherent Anti-Stokes Raman Spectroscopy (CARS). *Appl Spectrosc*. 2016;31(4):253-271. doi:10.1366/000370277774463625.

64. Shirley JA, Hall RJ, Eckbreth AC. Folded BOXCARS for rotational Raman studies. *Opt Lett, OL*. 1980;5(9):380-382. doi:10.1364/OL.5.000380.

65. Cheng J-X, Volkmer A, Book LD, Xie XS. Multiplex Coherent Anti-Stokes Raman Scattering Microspectroscopy and Study of Lipid Vesicles. *J Phys Chem B*. 2002;106(34):8493-8498. doi:10.1021/jp025771z.

66. Volkmer A, Cheng J-X, Sunney Xie X. Vibrational Imaging with High Sensitivity via

Epidetected Coherent Anti-Stokes Raman Scattering Microscopy. *Phys Rev Lett*. 2001;87(2):4142-4144. doi:10.1103/PhysRevLett.87.023901.

67. Knutsen KP, Messer BM, Onorato RM, Saykally RJ. Chirped Coherent Anti-Stokes Raman Scattering for High Spectral Resolution Spectroscopy and Chemically Selective Imaging. *J Phys Chem B*. 2006;110(12):5854-5864. doi:10.1021/jp052416a.

68. Hellerer T, Enejder AMK, Zumbusch A. Spectral focusing: High spectral resolution spectroscopy with broad-bandwidth laser pulses. *Appl Phys Lett*. 2004;85(1):25-27. doi:10.1063/1.1768312.

69. Pegoraro AF, Ridsdale A, Moffatt DJ, Jia Y, Pezacki JP, Stolow A. Optimally chirped multimodal CARS microscopy based on a single Ti:sapphire oscillator. *Opt Express, OE*. 2009;17(4):2984-2996. doi:10.1021/jp035693v.

70. Gu X, Akturk S, Trebino R. Spatial chirp in ultrafast optics. *Optics Communications*. 2004;242(4-6):599-604. doi:10.1016/j.optcom.2004.09.004.

71. Cleff C, Groß P, Kleinschmidt L, Epping J. Optimally chirped CARS using fiber stretchers. *Appl Phys B*. 2011. doi:10.1007/s00340-011-4751-5.

72. Rocha-Mendoza I, Langbein W, Borri P. Coherent anti-Stokes Raman microspectroscopy using spectral focusing with glass dispersion. *Appl Phys Lett*. 2008;93(20):201103-201103. doi:10.1063/1.3028346.

73. Hashimoto M, Araki T, Kawata S. Molecular vibration imaging in the fingerprint region by use of coherent anti-Stokes Raman scattering microscopy with a collinear configuration. *Opt Lett, OL*. 2000;25(24):1768-1770. doi:10.1364/OL.25.001768.

74. Czamara K, Majzner K, Pacia MZ, Kochan K, Kaczor A, Baranska M. Raman spectroscopy of lipids: a review. *J Raman Spectrosc*. 2014;46(1):4-20. doi:10.1002/jrs.4607.

75. Wang H, Fu Y, Zickmund P, Shi R, Cheng J-X. Coherent Anti-Stokes Raman Scattering Imaging of Axonal Myelin in Live Spinal Tissues. *Biophys J*. 2005;89(1):581-591. doi:10.1529/biophysj.105.061911.

76. Ranasinghesagara JC, de Vito G, Piazza V, Potma EO, Venugopalan V. Effect of scattering on coherent anti-Stokes Raman scattering (CARS) signals. *Opt Express, OE*. 2017;25(8):8638–15. doi:10.1364/OE.25.008638.

77. Bégin S, Burgoyne B, Mercier V, Villeneuve A, Vallée R, Côté D. Coherent anti-Stokes Raman scattering hyperspectral tissue imaging with a wavelength-swept system. *Biomed Opt Express*. 2011;2(5):1296-1306. doi:10.1364/BOE.2.001296.

78. Evans CL, Potma EO, Puoris'haag M, Côté D, Lin CP, Xie XS. Chemical imaging of tissue in vivo with video-rate coherent anti-Stokes Raman scattering microscopy. *Proc*

Natl Acad Sci USA. 2005;102(46):16807-16812. doi:10.1073/pnas.0508282102.

79. Fu Y, Wang H, Shi R, Cheng J-X. Characterization of photodamage in coherent anti-Stokes Raman scattering microscopy. *Opt Express*. 2006;14(9):3942-3951.

80. Kennedy AP, Sutcliffe J, Cheng J-X. Molecular Composition and Orientation in Myelin Figures Characterized by Coherent Anti-Stokes Raman Scattering Microscopy. *Langmuir*. 2005;21(14):6478-6486. doi:10.1021/la046820x.

81. Breunig HG, Weinigel M, Bückle R, et al. Clinical coherent anti-Stokes Raman scattering and multiphoton tomography of human skin with a femtosecond laser and photonic crystal fiber. *Laser Phys Lett*. 2013;10(2):025604-025606. doi:10.1088/1612-2011/10/2/025604.

82. Maiman TH. Stimulated optical radiation in Ruby. *Nature*. 1960;187(4736):493-494. doi:10.1038/187493a0.

83. Begley RF, Harvey AB, Byer RL. Coherent anti-Stokes Raman spectroscopy. *Appl Phys Lett*. 1974;25(7):387-390. doi:10.1063/1.1655519.

84. Chabay I, Klauminzer GK, Hudson BS. Coherent anti-Stokes Raman spectroscopy (CARS): Improved experimental design and observation of new higher-order processes. *Appl Phys Lett*. 1976;28(1):27-29. doi:10.1063/1.88553.

85. Gustafson EK, Byer RL. Coherent anti-Stokes Raman scattering from small volumes. *Opt Lett, OL*. 1984;9(6):220-222. doi:10.1364/OL.9.000220.

86. Duncan MD, Reintjes J, Manuccia TJ. Scanning coherent anti-Stokes Raman microscope. *Opt Lett, OL*. 1982;7(8):350-352. doi:10.1364/OL.7.000350.

87. Duncan MD. Molecular discrimination and contrast enhancement using a scanning coherent anti-stokes Raman microscope. *Optics Communications*. 1984;50(5):307-312. doi:10.1016/0030-4018(84)90173-1.

88. Zumbusch A, Holtom GR, Xie XS. Three-dimensional vibrational imaging by coherent anti-stokes raman scattering. *Phys Rev Lett*. 1999;82(20):4142-4145. doi:10.1103/PhysRevLett.82.4142.

89. Potma E, de Boeij WP, van Haastert PJ, Wiersma DA. Real-time visualization of intracellular hydrodynamics in single living cells. *Proc Natl Acad Sci USA*. 2001;98(4):1577-1582. doi:10.1073/pnas.031575698.

90. Cheng J-X, Volkmer A, Book LD, Xie XS. An Epi-Detected Coherent Anti-Stokes Raman Scattering (E-CARS) Microscope with High Spectral Resolution and High Sensitivity. *J Phys Chem B*. 2001;105(7):1277-1280. doi:10.1021/jp003774a.

91. Pawley JB. *Handbook of Biological Confocal Microscopy: Third Edition*. (Pawley JB, ed.). Boston, MA: Springer US; 2006:1-985. doi:10.1007/978-0-387-45524-2.

92. Potma EO, Jones DJ, Cheng JX, Xie XS, Ye J. High-sensitivity coherent anti-Stokes Raman scattering microscopy with two tightly synchronized picosecond lasers. *Opt Lett, OL*. 2002;27(13):1168-1170.

93. Knutsen KP, Johnson JC, Miller AE, Petersen PB, Saykally RJ. High spectral resolution multiplex CARS spectroscopy using chirped pulses. *Chemical Physics Letters*. 2004;387(4-6):436-441. doi:10.1016/j.cplett.2004.02.049.

94. Zhao W, Bourkoff E. FEMTOSECOND PULSE PROPAGATION IN OPTICAL FIBERS: HIGHER ORDER EFFECTS. *IEEE Journal of Quantum Electronics*. 1988;24(2):365-372. doi:10.1109/3.133.

95. Munhoz F, Brustlein S, Gachet D, Billard F, Brasselet S, Rigneault H. Raman depolarization ratio of liquids probed by linear polarization coherent anti-Stokes Raman spectroscopy. Volkmer A, Radi PP, Zheltikov AM, Zumbusch A, eds. *J Raman Spectrosc*. 2009;40(7):775-780. doi:10.1002/jrs.2289.

96. Koster J, Popp J, Schlücker S. Quantitative polarization-sensitive resonance CARS and resonance Raman spectroscopy on octaethylporphine. *J Raman Spectrosc*. 2006;37(1-3):384-391. doi:10.1002/jrs.1439.

97. Chikishev AY, Lucassen GW, Koroteev NI, Otto C, Greve J. Polarization sensitive coherent anti-Stokes Raman scattering spectroscopy of the amide I band of proteins in solutions. *Biophys J*. 1992;63(4):976-985. doi:10.1016/S0006-3495(92)81691-0.

98. Song JJ, Eesley GL, Levenson MD. Background suppression in coherent Raman spectroscopy. *Appl Phys Lett*. 1976;29(9):567-569. doi:10.1063/1.89189.

99. Eckbreth AC, Hall RJ. CARS concentration sensitivity with and without nonresonant background suppression. *Combustion Science and Technology*. 1981;25(5-6):175-192. doi:10.1080/00102208108547501.

100. Dick B. Response function theory of time-resolved CARS and CSRS of rotating molecules in liquids under general polarization conditions. *Chemical Physics*. 1987;113(1):131-147. doi:10.1016/0301-0104(87)80226-4.

101. Kohles N, Laubereau A. Polarization effects of picosecond CARS in liquids. *Applied Physics B Photophysics and Laser Chemistry*. 1986;39(3):141-147. doi:10.1007/BF00697411.

102. Oudar JL, Smith RW, Shen YR. Polarization-sensitive coherent anti-Stokes Raman spectroscopy. *Appl Phys Lett*. 1979;34(11):758-760. doi:10.1063/1.90663.

103. de Aguiar HB, Gasecka P, Brasselet S. Quantitative analysis of light scattering in polarization-resolved nonlinear microscopy. *Opt Express*. 2015;23(7):8960-8973. doi:10.1364/OE.23.008960.

104. Lu F, Zheng W, Huang Z. Elliptically polarized coherent anti-Stokes Raman scattering microscopy. *Opt Lett, OL*. 2008;33(23):2842-2844.

105. Bélanger E, Bégin S, Laffray S, De Koninck Y, Vallée R, Côté D. Quantitative myelin imaging with coherent anti-Stokes Raman scattering microscopy: alleviating the excitation polarization dependence with circularly polarized laser beams. *Opt Express, OE*. 2009;17(21):18419-18432.

106. Cleff C, Gasecka A, Ferrand P, Rigneault H, Brasselet S, Duboisset J. Direct imaging of molecular symmetry by coherent anti-stokes Raman scattering. *Nature Communications*. 2016;7:11562. doi:10.1038/ncomms11562.

107. Turcotte R, Rutledge DJ, Bélanger E, Dill D, Macklin WB, Côté DC. Intravital assessment of myelin molecular order with polarimetric multiphoton microscopy. *Nature Publishing Group*. August 2016:1-8. doi:10.1038/srep31685.

108. Bégin S, Bélanger E, Laffray S, Vallée R, Côté D. In vivo optical monitoring of tissue pathologies and diseases with vibrational contrast. *J Biophoton*. 2009;2(11):632-642. doi:10.1002/jbio.200910071.

109. Bioud F-Z, Gasecka P, Ferrand P, Rigneault H, Duboisset J, Brasselet S. Structure of molecular packing probed by polarization-resolved nonlinear four-wave mixing and coherent anti-Stokes Raman-scattering microscopy. *Physical Review A - Atomic, Molecular, and Optical Physics*. 2014;89(1). doi:10.1103/PhysRevA.89.013836.

110. Munhoz F, Rigneault H, Brasselet S. High order symmetry structural properties of vibrational resonances using multiple-field polarization coherent anti-Stokes Raman spectroscopy microscopy. *Phys Rev Lett*. 2010;105(12):123903. doi:10.1103/PhysRevLett.105.123903.

111. Duboisset J, Berto P, Gasecka P, et al. Molecular orientational order probed by coherent anti-Stokes Raman scattering (CARS) and stimulated Raman scattering (SRS) microscopy: a spectral comparative study. *J Phys Chem B*. 2015;119(7):3242-3249. doi:10.1021/jp5113813.

112. Gasecka P, Jaouen A, Bioud F-Z, et al. Lipid Order Degradation in Autoimmune Demyelination Probed by Polarized Coherent Raman Microscopy. *Biophys J*. 2017;113(7):1520-1530. doi:10.1016/j.bpj.2017.07.033.

113. de Vito G, Bifone A, Piazza V. Rotating-polarization CARS microscopy: combining chemical and molecular orientation sensitivity. *Opt Express*. 2012;20(28):29369-29377. doi:10.1364/OE.20.029369.

114. de Vito G, Canta A, Marmiroli P, Piazza V. A large-field polarisation-resolved laser scanning microscope: Applications to CARS imaging. *Journal of Microscopy*. 2015;260(2):194-199. doi:10.1111/jmi.12282.

115. de Vito G, Piazza V. Fast signal analysis in Rotating-Polarization CARS microscopy. *Optical Data Processing and Storage*. 2014;1(1):1-5. doi:10.2478/odps-2014-0001.

116. de Vito G, Tonazzini I, Cecchini M, Piazza V. RP-CARS: label-free optical readout of the myelin intrinsic healthiness. *Opt Express, OE*. 2014;22(11):13733–11. doi:10.1364/OE.22.013733.

117. Plemel JR, Michaels NJ, Weishaupt N, et al. Mechanisms of lysophosphatidylcholine-induced demyelination: A primary lipid disrupting myelinopathy. *Glia*. 2018;66(2):327-347. doi:10.1002/glia.23245.

118. de Vito G, Cappello V, Tonazzini I, Cecchini M, Piazza V. RP-CARS reveals molecular spatial order anomalies in myelin of an animal model of Krabbe disease. *J Biophoton*. 2017;10(3):385-393. doi:10.1002/jbio.201500305.

119. Cheng JX, Xie XS. Vibrational spectroscopic imaging of living systems: An emerging platform for biology and medicine. *Science*. 2015;350(6264):aaa8870-aaa8870. doi:10.1126/science.aaa8870.

120. Evans CL, Xie XS. Coherent Anti-Stokes Raman Scattering Microscopy: Chemical Imaging for Biology and Medicine. *Annual Rev Anal Chem*. 2008;1(1):883-909. doi:10.1146/annurev.anchem.1.031207.112754.

121. Galli R, Uckermann O, Andresen EF, et al. Intrinsic Indicator of Photodamage during Label-Free Multiphoton Microscopy of Cells and Tissues. Aegerter CM, ed. *PLoS ONE*. 2014;9(10):e110295–10. doi:10.1371/journal.pone.0110295.

122. Yaroslavsky AN, Schulze PC, Yaroslavsky IV, Schober R, Ulrich F, Schwarzmaier HJ. Optical properties of selected native and coagulated human brain tissues in vitro in the visible and near infrared spectral range. *Phys Med Biol*. 2002;47(12):2059-2073.

123. Hale GM, Querry MR. Optical Constants of Water in the 200-nm to 200-Mm Wavelength Region. *Appl Opt*. 1973:555-563.

124. van Veen RLP, Sterenborg HJCM, Pifferi A, Torricelli A, Chikoidze E, Cubeddu R. Determination of visible near-IR absorption coefficients of mammalian fat using time- and spatially resolved diffuse reflectance and transmission spectroscopy. *J Biomed Opt*. 2005;10(5):054004-054006. doi:10.1117/1.2085149.

125. Lee C, Bain CD. Raman spectra of planar supported lipid bilayers. *Biochim Biophys Acta*. 2005;1711(1):59-71. doi:10.1016/j.bbamem.2005.02.006.

126. Nave K-A, Werner HB. Myelination of the Nervous System: Mechanisms and

Functions. *Annu Rev Cell Dev Biol*. 2014;30(1):503-533. doi:10.1146/annurev-cellbio-100913-013101.

127. MD PMF, MD MAR, MD PFB, et al. Association between pathological and MRI findings in multiple sclerosis. *The Lancet Neurology*. 2012;11(4):349-360. doi:10.1016/S1474-4422(12)70003-0.

128. Love S. Demyelinating diseases. *Journal of Clinical Pathology*. 2006;59(11):1151-1159. doi:10.1136/jcp.2005.031195.

129. Wu GF, Alvarez E. The Immunopathophysiology of Multiple Sclerosis. *Neurologic Clinics*. 2011;29(2):257-278. doi:10.1016/j.ncl.2010.12.009.

130. Wilkins A. *Progressive Multiple Sclerosis*. (Wilkins A, ed.). Cham: Springer; 2017. doi:10.1007/978-3-319-65921-3.

131. Khaibullin T, Ivanova V, Martynova E, et al. Elevated Levels of Proinflammatory Cytokines in Cerebrospinal Fluid of Multiple Sclerosis Patients. *Front Immunol*. 2017;8:647–10. doi:10.3389/fimmu.2017.00531.

132. Bongarzone ER, Pasquini JM, Soto EF. Oxidative damage to proteins and lipids of CNS myelin produced by in vitro generated reactive oxygen species. *J Neurosci Res*. 1995;41(2):213-221. doi:10.1002/jnr.490410209.

133. Terry RL, Ifergan I, Miller SD. Experimental Autoimmune Encephalomyelitis in Mice. In: *Autoimmunity*. Vol 1304. Methods in Molecular Biology. New York, NY: Springer New York; 2014:145-160. doi:10.1007/7651_2014_88.

134. Matsushima GK, Morell P. The neurotoxicant, cuprizone, as a model to study demyelination and remyelination in the central nervous system. *Brain Pathol*. 2001;11(1):107-116.

135. Taraboletti A, Walker T, Avila R, et al. Cuprizone Intoxication Induces Cell Intrinsic Alterations in Oligodendrocyte Metabolism Independent of Copper Chelation. *Biochemistry*. 2017;56(10):1518-1528. doi:10.1021/acs.biochem.6b01072.

136. Cantó C, Menzies KJ, Auwerx J. NAD+ Metabolism and the Control of Energy Homeostasis: A Balancing Act between Mitochondria and the Nucleus. *Cell Metabolism*. 2015;22(1):31-53. doi:10.1016/j.cmet.2015.05.023.

137. Fünfschilling U, Supplie LM, Mahad D, et al. Glycolytic oligodendrocytes maintain myelin and long-term axonal integrity. *Nature*. 2012;485(7399):517-521. doi:10.1038/nature11007.

138. Newcombe J, Uddin A, Dove R, et al. Glutamate Receptor Expression in Multiple Sclerosis Lesions. *Brain Pathol*. 2008;18(1):52-61. doi:10.1111/j.1750-3639.2007.00101.x.

139. Moody LR, Herbst AJ, Yoo HS, Vanderloo JP, Aiken JM. Comparative prion disease gene expression profiling using the prion disease mimetic, cuprizone. *Prion*. 2009;3(2):99-109. doi:10.4161/pri.3.2.9059.

140. Pott F, Gingele S, Clarner T, et al. Cuprizone effect on myelination, astrogliosis and microglia attraction in the mouse basal ganglia. *Brain Research*. 2009;1305:137-149. doi:10.1016/j.brainres.2009.09.084.

141. Benetti F, Ventura M, Salmini B, et al. NeuroToxicology Cuprizone neurotoxicity, copper deficiency and neurodegeneration. *Neurotoxicology*. 2010;31(5):509-517. doi:10.1016/j.neuro.2010.05.008.

142. Tanno O, Ota Y, Kitamura N, Katsube T, Inoue S. Nicotinamide increases biosynthesis of ceramides as well as other stratum corneum lipids to improve the epidermal permeability barrier. *Br J Dermatol*. 2000;143(3):524-531. doi:10.1046/j.1365-2133.2000.03705.x.

143. Nakashima Y, Suzue R. Effect of nicotinic acid on cerebroside synthesis in rat brain. *J Nutr Sci Vitaminol*. 1981;27(1):23-31.

144. Hiremath MM, Saito Y, Knapp GW, Ting JPY, Suzuki K, Matsushima GK. Microglial/macrophage accumulation during cuprizone-induced demyelination in C57BL/6 mice. *Journal of Neuroimmunology*. 1998;92(1-2):38-49. doi:10.1016/S0165-5728(98)00168-4.

145. Hibbits N, Yoshino J, Le TQ, Armstrong RC. Astrogliosis During Acute and Chronic Cuprizone Demyelination and Implications for Remyelination. *ASN Neuro*. 2012;4(6):AN20120062–16. doi:10.1042/AN20120062.

146. Praet J, Guglielmetti C, Berneman Z, Van der Linden A, Ponsaerts P. Cellular and molecular neuropathology of the cuprizone mouse model: Clinical relevance for multiple sclerosis. *Neuroscience and Biobehavioral Reviews*. 2014;47:485-505. doi:10.1016/j.neubiorev.2014.10.004.

147. Song S-K, Yoshino J, Le TQ, et al. Demyelination increases radial diffusivity in corpus callosum of mouse brain. *NeuroImage*. 2005;26(1):132-140. doi:10.1016/j.neuroimage.2005.01.028.

148. Sun S-W, Liang H-F, Trinkaus K, Cross AH, Armstrong RC, Song S-K. Noninvasive detection of cuprizone induced axonal damage and demyelination in the mouse corpus callosum. *Magn Reson Med*. 2006;55(2):302-308. doi:10.1002/mrm.20774.

149. Oakden W, Bock NA, Al-Ebraheem A, Farquharson MJ, Stanisz GJ. Early regional cuprizone-induced demyelination in a rat model revealed with MRI. *NMR Biomed*. 2017;30(9). doi:10.1002/nbm.3743.

150. Herder V, Hansmann F, Stangel M, Skripuletz T, Baumgärtner W, Beineke A. Lack of cuprizone-induced demyelination in the murine spinal cord despite oligodendroglial alterations substantiates the concept of site-specific susceptibilities of the central nervous system. *Neuropathology and Applied Neurobiology*. 2011;37(6):676-684. doi:10.1111/j.1365-2990.2011.01168.x.

151. Doan V, Kleindienst AM, McMahon EJ, Long BR, Matsushima GK, Taylor LC. Abbreviated exposure to cuprizone is sufficient to induce demyelination and oligodendrocyte loss. *J Neurosci Res*. 2013;91(3):363-373. doi:10.1002/jnr.23174.

152. Steelman AJ, Thompson JP, Li J. Demyelination and remyelination in anatomically distinct regions of the corpus callosum following cuprizone intoxication. *Neuroscience Research*. 2012;72(1):32-42. doi:10.1016/j.neures.2011.10.002.

153. Willard SS, Koochekpour S. Glutamate, Glutamate Receptors, and Downstream Signaling Pathways. *Int J Biol Sci*. 2013;9(9):948-959. doi:10.7150/ijbs.6426.

154. Meldrum BS. Glutamate as a neurotransmitter in the brain: review of physiology and pathology. *J Nutr*. 2000;130(4S Suppl):1007S–15S.

155. Wisden W, Seeburg PH. Mammalian ionotropic glutamate receptors. *Curr Opin Neurobiol*. 1993;3(3):291-298. doi:10.1016/0959-4388(93)90120-N.

156. Micu I, Jiang Q, Coderre E, et al. NMDA receptors mediate calcium accumulation in myelin during chemical ischaemia. *Nature*. 2005;51:7–5. doi:10.1038/nature04474.

157. Christensen PC, Welch NC, Brideau C, Stys PK. Functional ionotropic glutamate receptors on peripheral axons and myelin. *Muscle Nerve*. 2016;54(3):451-459. doi:10.1002/mus.25078.

158. Ouardouz M, Coderre E, Basak A, et al. Glutamate receptors on myelinated spinal cord axons: I. GluR6 kainate receptors. *Ann Neurol*. 2009;65(2):151-159. doi:10.1002/ana.21533.

159. Ouardouz M, Coderre E, Zamponi GW, et al. Glutamate receptors on myelinated spinal cord axons: II. AMPA and GluR5 receptors. *Ann Neurol*. 2009;65(2):160-166. doi:10.1002/ana.21539.

160. PhD RM, MD PKS, PhD PDV, MD SAL, PhD DFD. Personal View Mechanisms of glutamate toxicity in multiple sclerosis: biomarker and therapeutic opportunities. *The Lancet Neurology*. 2016;15(10):1089-1102. doi:10.1016/S1474-4422(16)30165-X.

161. Yawata I, Takeuchi H, Doi Y, Liang J, Mizuno T, Suzumura A. Macrophage-induced neurotoxicity is mediated by glutamate and attenuated by glutaminase inhibitors and gap junction inhibitors. *Life Sci*. 2008;82(21-22):1111-1116. doi:10.1016/j.lfs.2008.03.010.

162. Pitt D, Werner P, Raine CS. Glutamate excitotoxicity in a model of multiple sclerosis.

Nature Medicine. 2000;6(1):67-70. doi:10.1038/71555.

163. Matute C, Alberdi E, Domercq M, Pérez-Cerdá F, Pérez-Samartín A, Sánchez-Gómez MV. The link between excitotoxic oligodendroglial death and demyelinating diseases. *Trends in Neurosciences*. 2001;24(4):224-230. doi:10.1016/S0166-2236(00)01746-X.

164. Ma M, Ferguson TA, Schoch KM, et al. Calpains mediate axonal cytoskeleton disintegration during Wallerian degeneration. *Neurobiology of Disease*. 2013;56:34-46. doi:10.1016/j.nbd.2013.03.009.

165. Mata M, Kupina N, Fink DJ. Calpain II in rat peripheral nerve. *Brain Research*. 1991;564(2):328-331. doi:10.1016/0006-8993(91)91471-C.

166. Neumar RW, Meng FH, Mills AM, et al. Calpain Activity in the Rat Brain after Transient Forebrain Ischemia. *Experimental Neurology*. 2001;170(1):27-35. doi:10.1006/exnr.2001.7708.

167. Worku Hassen G, Feliberti J, Kesner L, Stracher A, Mokhtarian F. Prevention of axonal injury using calpain inhibitor in chronic progressive experimental autoimmune encephalomyelitis. *Brain Research*. 2008;1236:206-215. doi:10.1016/j.brainres.2008.07.124.

168. Trapp BD, Stys PK. Virtual hypoxia and chronic necrosis of demyelinated axons in multiple sclerosis. *The Lancet Neurology*. 2009;8(3):280-291. doi:10.1016/S1474-4422(09)70043-2.

169. Witte ME, Mahad DJ, Lassmann H, van Horssen J. Mitochondrial dysfunction contributes to neurodegeneration in multiple sclerosis. *Trends in Molecular Medicine*. 2014;20(3):179-187. doi:10.1016/j.molmed.2013.11.007.

170. Fischer MT, Wimmer I, Höftberger R, et al. Disease-specific molecular events in cortical multiple sclerosis lesions. *Brain*. 2013;136(6):1799-1815. doi:10.1093/brain/awt110.

171. Cummings KA, Popescu GK. Glycine-dependent activation of NMDA receptors. *J Gen Physiol*. 2015;145(6):513-527. doi:10.1085/jgp.201411302.

172. Lee SM, Sha D, Mohammed AA, et al. Motor and sensory neuropathy due to myelin infolding and paranodal damage in a transgenic mouse model of Charcot–Marie–Tooth disease type 1C. *Human Molecular Genetics*. 2013;22(9):1755-1770. doi:10.1093/hmg/ddt022.

173. Grochmal J, Teo W, Gambhir H, et al. A novel approach to 32-channel peripheral nervous system myelin imaging in vivo, with single axon resolution. *Journal of Neurosurgery*. 2018;2:1-9. doi:10.3171/2017.6.JNS17239.

174. Zhu H, Li Y, Vdović S, Long S, He G, Guo Q. Femtosecond coherent anti-Stokes

Raman scattering spectroscopy of hydrogen bonded structure in water and aqueous solutions. *Spectrochimica Acta Part A: Molecular and Biomolecular Spectroscopy*. 2015;151(C):262-273. doi:10.1016/j.saa.2015.06.115.

175. Schmierer K, Wheeler-Kingshott CAM, Boulby PA, et al. Diffusion tensor imaging of post mortem multiple sclerosis brain. *Human Brain Mapping Journal*. 2007;35(2):467-477. doi:10.1016/j.neuroimage.2006.12.010.

176. Smith B, Naji M, Murugkar S, Brideau C, Stys P, Anis H. A novel multimodal CARS miniaturized microscope. In: Periasamy A, König K, So PTC, eds. Vol 8226. SPIE; 2012:822629. doi:10.1117/12.909494.

177. Murugkar S, Smith B, Brideau C, Stys P, Anis H. Development of a fiber optic-based CARS exoscope for the in vivo study of spinal cord disorders. In: IEEE; 2011:96-99. doi:10.1109/LISSA.2011.5754165.

178. Lukić A, Dochow S, Chernavskaia O, et al. Fiber probe for nonlinear imaging applications. *J Biophoton*. 2015;9(1-2):138-143. doi:10.1002/jbio.201500010.

179. Bradler M, Baum P, Riedle E. Femtosecond continuum generation in bulk laser host materials with sub-μJ pump pulses. *Applied Physics B: Lasers and Optics*. 2009;97(3):561-574. doi:10.1007/s00340-009-3699-1.

180. Brideau C, Poon K, Stys PK. Broadly tunable high-energy spectrally focused CARS microscopy with chemical specificity and high resolution for biological samples. In: Periasamy A, König K, So PTC, eds. Vol 8588. SPIE; 2013:85880E–15. doi:10.1117/12.2005512.

181. Schön P, Munhoz F, Gasecka A, Brustlein S, Brasselet S. Polarization distortion effects in polarimetric two-photon microscopy. *Opt Express, OE*. 2008;16(25):20891-20901.

182. Wang X, Yang F, Yin J, Ferrand P, Brasselet S. Quantifying the polarization properties of non-depolarizing optical elements with virtual distorting elements. *Appl Opt*. 2017;56(10):2589–8. doi:10.1364/AO.56.002589.

183. Brideau C, Stys PK. Automated control of optical polarization for nonlinear microscopy. In: Periasamy A, König K, So PTC, eds. Vol 8226. SPIE; 2012:82263A. doi:10.1117/12.908995.

184. Brideau C, Zareinia K, Stys P. Applied 3D printing for microscopy in health science research. In: Periasamy A, So PTC, König K, eds. Vol 9329. SPIE; 2015:93292X–9. doi:10.1117/12.2079659.

185. Ridsdale A, Micu I, Stys PK. Conversion of the Nikon C1 confocal laser-scanning head for multiphoton excitation on an upright microscope. *Appl Opt*. 2004;43(8):1669-1675.

186. Piazza V, de Vito G, Farrokhtakin E, Ciofani G, Mattoli V. Femtosecond-Laser-Pulse

Characterization and Optimization for CARS Microscopy. Shi H, ed. *PLoS ONE*. 2016;11(5):e0156371–13. doi:10.1371/journal.pone.0156371.

187. Goodberlet J, Hagelstein PL. Chirp-compensated autocorrelation of optical pulses. *Opt Lett, OL*. 1993;18(19):1648-1650. doi:10.1364/OL.18.001648.

188. Kuptsov AH, Zhizhin GN. *Handbook of Fourier Transform Raman and Infrared Spectra of Polymers*. Elsevier; 1998.

189. Koenig JL. *Infrared and Raman Spectroscopy of Polymers*. iSmithers Rapra Publishing; 2001.

190. Guild JB, XU C, WEBB WW. Measurement of group delay dispersion of high numerical aperture objective lenses using two-photon excited fluorescence. *Appl Opt*. 1997;36(1):397-401. doi:10.1364/AO.36.000397.

191. Baeten V, Hourant P, Morales MT, Aparicio R. Oil and Fat Classification by FT-Raman Spectroscopy. *J Agric Food Chem*. 1998;46(7):2638-2646. doi:10.1021/jf9707851.

192. Levine D, Monser GJ. Polarization, Ghost, and Shading Effects in Dichroic Beam Splitters. *J Opt Soc Am*. 1961;51(7):783-789.

193. Clancy EP. Polarization Effects in Photomultipler Tubes. *J Opt Soc Am A*. 1952;45:357.

194. Kang H, Jia B, Gu M. Polarization characterization in the focal volume of high numerical aperture objectives. *Opt Express*. 2010;18(10):10813-10819. doi:10.1364/OE.18.010813.

195. Acs P, Selak MA, Komoly S, Kalman B. Distribution of oligodendrocyte loss and mitochondrial toxicity in the cuprizone-induced experimental demyelination model. *Journal of Neuroimmunology*. 2013;262(1-2):128-131. doi:10.1016/j.jneuroim.2013.06.012.

196. Martín MG, Pfrieger F, Dotti CG. Cholesterol in brain disease: sometimes determinant and frequently implicated. *EMBO Rep*. 2014;15(10):1036-1052. doi:10.15252/embr.201439225.

197. Torkildsen O, Brunborg LA, Milde AM, Moslashrk SJ, Myhr K-M, Boslash L. A salmon based diet protects mice from behavioural changes in the cuprizone model for demyelination. *Clinical Nutrition*. 2009;28(1):83-87. doi:10.1016/j.clnu.2008.10.015.

198. Lycette RM, Danforth WF, Koppel JL, Olwin JH. The binding of luxol fast blue arn by various biological lipids. *Biotechnic & Histochemistry*. 1970;45(4):155-160. doi:10.3109/10520297009067471.

199. Berghoff SA, Gerndt N, Winchenbach J, et al. Dietary cholesterol promotes repair of demyelinated lesions in the adult brain. *Nature Communications*. 2017;8:1-15.

doi:10.1038/ncomms14241.

200. Ozsvár A, Szipőcs R, Ozsvár Z, et al. Quantitative analysis of lipid debris accumulation caused by cuprizone induced myelin degradation in different CNS areas. *Brain Research Bulletin*. 2018;137:277-284. doi:10.1016/j.brainresbull.2018.01.003.

201. Torkildsen, Brunborg LA, Myhr KM, Bø L. The cuprizone model for demyelination. *Acta Neurologica Scandinavica*. 2008;117(SUPPL. 188):72-76. doi:10.1111/j.1600-0404.2008.01036.x.

202. Sezgin E, Sadowski T, Simons K. Measuring Lipid Packing of Model and Cellular Membranes with Environment Sensitive Probes. *Langmuir*. 2014;30(27):8160-8166. doi:10.1021/la501226v.

203. Sankaram MB, Thompson TE. Interaction of Cholesterol with Various Glycerophospholipids and Sphingomyelin. *Biochemistry*. 1990;29(47):10670-10675. doi:10.1021/bi00499a014.